DEVELOPMENT OF LOW ELECTROMAGNETIC IMPACT SATELLITE PLATFORMS THROUGH THE USE AND OPTIMIZATION OF GRAPHENE AND CARBONYL IRON-BASED MATERIALS AND PAINTS

Faculty of Civil and Industrial Engineering

Department of Electrical and Energy Engineering (DIEE)
PhD Course in Electrical, Material and Nanotechnology Engineering

Alice Nicole Casling

Matricola 1656344

Supervisor

Prof. Alessio Tamburrano

Co-supervisor

Ing. Emiliano Scione

Ing. Alessandro Giordani

Ciclo di dottorato XXXVII

Acknowledgments

I wish to acknowledge the research group at the Department of Electrical and Energy Engineering (DIEE) of Sapienza University of Rome, with particular mention of Professor Alessio Tamburrano. The members of the Nanotechnology Laboratory and the Electromagnetic Compatibility (EMC) Laboratory provided the necessary guidance and collaborative environment to conduct this work.

Acknowledgment is also due to the EMC Group at Thales Alenia Space Italia S.p.A., specifically Ing. Emiliano Scione and Giovanni Maria Mongini, for their professional collaboration. Their support in providing specialized aerospace-grade materials and facilitating simulations via their high-performance computing facilities was essential in bridging the gap between fundamental research and satellite applications.

Abstract

The rapid evolution of the aerospace industry, characterized by the proliferation of Low Earth Orbit (LEO) constellations and the aggressive miniaturization of platforms like CubeSats and SmallSats, has imposed unprecedented electromagnetic constraints on payload and platform design. Modern satellite architectures require high-density electronic integration where the proximity of sensitive components—such as digital units and RF front-ends—intensifies the risk of Electromagnetic Interference (EMI). Traditional metallic shielding often fails in the S and C-bands (2–8 GHz) in case of cavity resonance effects, where internal reflections degrade the signal-to-noise ratio. Furthermore, the volumetric and mass penalties of traditional bulk absorbers are incompatible with modern launch constraints.

This PhD thesis investigates the development of multifunctional, thin, and tunable electromagnetic absorbers designed to mitigate internal EMI without occupying critical satellite volume. The research focuses on two primary architectures: modular multilayer thin films and bi-layered coatings for honeycomb structures. The practical realization of these designs necessitated an initial phase focused on formulating high-performance electromagnetic paints, specifically by optimizing the dispersion of dielectric and magnetic fillers within aeronautical and aerospace-grade matrices.

The material phase of this study characterizes the production of lossy dielectric and magnetic composites using Graphene Nanoplatelets (GNP) and Carbonyl Iron Particles (CIP). Specifically, the research investigates how both the host matrix and the filler morphology contribute to the enhancement of the composites' complex electromagnetic parameters. The study explores the mechanical transformation of spherical CIP into a flaky morphology (CIF) as a mechanism for shifting resonance frequencies and increasing permeability. While the resulting increase in specific surface area triggers rapid oxidation—presenting a compelling challenge for future anti-corrosive stabilization—the altered magnetic performance observed in the oxidized state underscores the significant influence of particle shape. Furthermore, the investigation evaluates the optimization of the host polymer, revealing that an organic solvent-based system (AZ) facilitates superior processability and achieves a substantial increase in complex relative permeability compared to water-based alternatives.

Building upon the data obtained from the material characterization phase, the study progressed to the development of an industrially-oriented engineered multilayer structure. By integrating the measured complex relative permittivity and permeability of each single layer into an optimization framework based on Transmission Line Theory, the thicknesses and stacking sequences were precisely tuned to develop a cohesive adhesive stack suitable for rapid industrial application. This optimized architecture, with a total thickness of 6.21

mm, achieved a Reflection Loss (RL) of -20.11 dB at 2 GHz through the strategic alternation of GNP-loaded and CIP-loaded layers.

While the multilayer approach demonstrated effective dual-band absorption as a compact additive solution, this work also explores a complementary paradigm: embedding C-band attenuation directly within structural honeycomb panels. By applying a conformal bi-layer coating — a CIP foundation layer beneath a GNP topcoat — to the honeycomb lattice via sequential dip-coating, the inherent open-cell geometry is exploited to force incident waves into multiple interactions with the lossy walls. This approach co-locates electromagnetic shielding within a load-bearing component already present in small satellite architectures, enabling a 5 mm panel to maintain RL > 10 dB across the 4–6 GHz band while minimizing net mass addition to the platform.

Publications List

[A] A. Giordani et al. "Feasibility Study of a Graphene-Loaded Composite for Improved EMI Performance of Satellite Cavities." 2023 International Symposium on Electromagnetic Compatibility–EMC Europe. IEEE, 2023.

[B] A. N. Casling et al. "Performance Assessment of Magnetic Polymeric Composites for EMI Reduction in Small Satellites." 2025 ESA Workshop on Aerospace EMC (Aerospace EMC). IEEE, 2025.

[C] A. N. Casling et al. “Honeycomb Structures Coated with Graphene Nanoplatelets and Carbonyl Iron-Based Paints for C-Band EM Absorption.” 2026 International Symposium on Electromagnetic Compatibility–EMC Europe, IEEE, 2026. (accepted)

[D] A. N. Casling et al. “Multilayer Panels Incorporating GNP/CIP-Loaded Paints for S-Band EMI Absorption in Space Environments“, IEEE Transactions on Electromagnetic Compatibility. (under submission)

INDEX

Abbreviations List

AFM: Atomic Force Microscopy

AW: Aeronautical-grade Water-based paint

AZ: Aerospace-grade solvent-based paint

CB: Carbon Black

CGS: CIP–GNP–Substrate (layer stacking sequence)

CIF: Carbonyl Iron Flakes

CIP: Carbonyl Iron Particles

CNT: Carbon Nanotubes

CST: Computer Simulation Technology (Studio Suite)

DC: Direct Current

ECSS: European Cooperation for Space Standardization

EDS: Energy Dispersive Spectroscopy

EM: Electromagnetic

EMC: Electromagnetic Compatibility

EMI: Electromagnetic Interference

ESA: European Space Agency

FDM: Fused Deposition Modelling

GCS: GNP–CIP–Substrate (inverted layer stacking sequence)

GGS: GNP–GNP–Substrate (purely dielectric stacking configuration)

GNP: Graphene Nanoplatelets

HC: Honeycomb

LEO: Low Earth Orbit

MATLAB: MATrix LABoratory (numerical computing software)

NRW: Nicolson–Ross–Weir (parameter extraction method)

PEC: Perfect Electric Conductor

PNA-X: Performance Network Analyser – eXtended (Agilent/Keysight)

RAM: Radar Absorbing Material

RF: Radio Frequency

RL: Reflection Loss

SAR: Synthetic Aperture Radar

SEM: Scanning Electron Microscope

TEM: Transverse Electromagnetic (propagation mode)

TLT: Transmission Line Theory

TT&C: Telemetry, Tracking, and Command

VNA: Vector Network Analyzer

1.

INTRODUCTION

1.1 Mitigation of Low-GHz EMI in Next-Generation Satellite Architectures

The rapid evolution of the aerospace industry, characterized by the proliferation of Low Earth Orbit (LEO) constellations and the radical miniaturization of platforms such as CubeSats and SmallSats, has imposed unprecedented constraints on payload and platform design. Modern satellite platforms require high-density electronic integration, where the extreme proximity of sensitive components significantly escalates the risk of Electromagnetic Interference (EMI) and internal crosstalk. As underscored by the aerospace EMI shielding literature, overlooking the electromagnetic radiation environment in spacecraft and satellite design carries significant risks to both the performance and operational lifetime of onboard systems, underscoring the fundamental need for advanced EMI shielding solutions in modern space platforms [1]. In these confined, densely packed environments, electric fields generated by onboard equipment—such as digital units and radio-frequency (RF) components—can resonate and amplify, leading to conducted and radiated interference within the satellite cavity. While traditional metallic enclosures have historically provided robust shielding via reflection, they present critical drawbacks for modern miniaturized platforms. The inefficiency of this approach is two-fold: not only do these covers impose a mass penalty reaching one-fifth of a power system's total weight [2], but their reflective nature exacerbates the internal noise environment through cavity resonance. This phenomenon degrades signal integrity and creates resonant noise floors that can render sensitive payloads ineffective. Consequently, the "NewSpace" era demands a shift from bulky, reflective shielding toward lightweight, absorptive materials that can be integrated directly into the spacecraft's architecture.

Consequently, the design of multifunctional materials has become increasingly attractive for the production of smart systems that provide high-performance electromagnetic absorption without occupying critical volume within the satellite [3]. Instead of relying on bulky, invasive shielding, the goal shifts toward integrating these functions into the existing internal surfaces or thin-film architectures to maintain the mission's strict spatial constraints. Particular attention is currently focused on the S and lower C-bands (2–6 GHz), a frequency range critical for satellite Telemetry, Tracking, and Control (TT&C), weather radar applications, and Synthetic Aperture Radar (SAR) antennas. However, achieving effective absorption across this diverse spectrum poses a significant physical challenge.

According to electromagnetic theory, lower frequencies—characterized by longer wavelengths—typically require a proportional increase in absorber thickness to achieve the phase cancellation necessary for impedance matching. This relationship, often referred to as the quarter-wavelength principle or Salisbury Screen limit, dictates that the thickness of a resonant absorber is fundamentally linked to the wavelength of the incident radiation and the electromagnetic properties of the medium [4, 5, 6].

At a frequency of 2 GHz, a standard air-spaced resonant screen would require a thickness of several centimeters—a dimension entirely incompatible with the high-stowage-efficiency requirements of modern space platforms where every millimeter of cavity space is at a premium. To circumvent these volumetric limitations, research has shifted toward the development of polymeric nanocomposites enriched with functional fillers. Dielectric loss materials, such as carbon nanotubes (CNTs) and graphene nanoplatelets (GNP), have gained considerable attention due to their ability to exploit interfacial polarization and ohmic losses to dissipate energy within a very thin profile [7, 8]. At higher frequencies, such as the X-band (8–12 GHz), the physics of wave-matter interaction are inherently more favorable for thin-film solutions: shorter wavelengths reduce the required absorber thickness to the millimeter scale, while a reduced skin depth confines electromagnetic energy closer to the material surface, allowing even lightweight conductive coatings to achieve significant attenuation. As a result, the X-band has become one of the most extensively studied regimes in the open literature, with a wide body of work demonstrating that dielectric nanocomposites based on carbon fillers can reliably achieve reflection losses exceeding −10 dB within profiles of just 1–3 mm [9]. The relative maturity of X-band absorber design means that solutions in this range are comparatively well-established, and the incremental performance gains available through further material optimization are limited.

The frontier challenge lies instead at lower frequencies. In the S and lower C-bands (2–6 GHz), the same thin conductive composites that perform well at X-band become largely ineffective: the skin depth increases substantially, causing the material to remain electrically thin and allowing electromagnetic energy to pass through with minimal interaction or, conversely, causing high surface reflectivity that leads to narrow absorption bandwidths. Achieving meaningful absorption in this range while simultaneously satisfying the mass and thickness budgets imposed by space applications — where structural weight penalties are measured in launch cost per kilogram — defines the core design challenge that motivates this work.

To address these limitations in the S and lower C-bands, magnetic loss materials—utilizing carbonyl iron particles (CIP), ferrites, or soft magnetic alloys—are employed to exploit natural ferromagnetic resonance, hysteresis loops, and eddy current effects [10–12].

Unlike purely conductive fillers that rely on ohmic losses, these magnetic media utilize the dynamic lag of the magnetization vector behind the alternating external magnetic field to dissipate energy even when the material is physically thin relative to the incident wavelength [13].

The efficacy of these magnetic absorbers is fundamentally bounded by Snoek's limit, a physical law that establishes an intrinsic inverse relationship between a material's initial static permeability and its resonance frequency [14]. This principle dictates that materials with high permeability inevitably suffer from a lower resonance frequency, thereby restricting the effective bandwidth in the GHz range. To mitigate this frequency ceiling and suppress the skin effect within the particles themselves, the morphology of the inclusions becomes a critical design parameter. Tailored size distributions and high-aspect-ratio shapes, such as flakes or needles, introduce shape anisotropy that allows the material to exceed the conventional Snoek limit, shifting the resonance to higher frequencies while maintaining high permeability [15–17]. These magnetic inclusions provide the electromagnetic density necessary to effectively compress the wavelength within the material, facilitating radical miniaturization of the absorber's physical profile without compromising its attenuation capabilities.

Beyond individual material fabrication, the integration of these absorbers into functional aerospace environments can be achieved through multilayered architectures—a specific technical response to the inherent conflict between broadband performance and ultra-thin profiles. By precisely stacking layers with staggered dielectric and magnetic properties, it is possible to engineer structures in which the transition from the free-space air interface to the lossy material gradually increases in electromagnetic density, guiding the incident wave into the material for internal dissipation rather than reflecting it back into the sensitive satellite cavity [18-21]. The practical implementation of these designs can utilize thin, flexible film absorbers applied directly onto internal housings or the interior walls of a satellite without requiring structural modifications—an approach that has been investigated specifically in the context of reducing electromagnetic scattering from satellite surfaces [22]. These multilayered thin-film structures provide distinct advantages by utilizing the multiple boundaries between distinct layers to create additional sites for interfacial polarization, enhancing energy dissipation at each layer interface [23, 24].

A further and highly effective approach is based on the realization of lossy honeycomb (HC) panels, which provide an alternative to monolithic absorbers by utilizing geometric mechanisms. HC panels impregnated or coated with lossy materials facilitate volumetric attenuation of incident EM waves through multiple internal reflections, progressively dissipating EM energy within the cellular structure [25–30]. These panels are of particular interest for lightweight applications where a high degree of attenuation is required without adding excessive volume to the satellite's internal footprint [31]. The EM performance of HC RAM can be tailored through control of the panel thickness, cell dimension, and the electromagnetic properties of the coating [32]. Recent studies have investigated the effect of combining dielectric top layers with magnetic bottom layers within honeycomb cores to enhance this internal multiple reflection mechanism [33]. This structural approach allows for the dissipation of energy through waveguide modes generated inside the hexagonal cells, offering a solution that is both electromagnetically distinct from traditional monolithic absorbers and compatible with the high-density requirements of modern space systems.

1.2 Thesis Objectives

The central aim of this thesis is to reconcile the constraints of electromagnetic absorber design with the demanding volumetric requirements of miniaturized satellite platforms, producing thin solutions whose performance is explicitly engineered for the S and lower C-band frequency ranges. Industrial deployability is treated as a non-negotiable design criterion throughout: all proposed solutions take the form of structural coatings or thin films, conceived to be applied within densely populated electronic cavities without interfering with established aerospace manufacturing workflows. Toward this end, the research undertakes a systematic investigation of two distinct composite formulation strategies: the enhancement of complex relative permeability in magnetically loaded systems, and the enhancement of complex relative permittivity in lossy dielectric materials — both pursued at reduced frequencies and jointly contributing to the overarching absorption objectives. The influence of the polymeric matrix in combination with functional fillers is examined in depth, alongside the role of filler morphology — notably the use of anisotropic flaky particles — as a means of increasing the electromagnetic density of the composite and compressing the effective wavelength to circumvent the thickness penalties conventionally associated with low-frequency absorption.

A central methodological contribution is the thickness-modulated design framework, wherein multilayered architectures are engineered by varying layer thickness and filler loading to tune reflection loss peaks without altering the base material chemistry. This logic is subsequently extended to a structural dimension: the internal walls of periodic honeycomb geometries are functionalized with these same paint systems, arranged in strategic bilayer configurations. By leveraging the honeycomb lattice, these structures exploit a multi-reflection effect that forces incident waves into repeated interactions with the lossy cell walls, thereby amplifying the coatings' intrinsic dissipative mechanisms.

The convergence of compositionally tailored absorbing layers and periodic structural geometries provides a viable route to circumventing the classical thickness-frequency trade-off, yielding compact, high-performance attenuation systems compatible with the architectural constraints of next-generation space platforms.

1.3 Thesis Organization

The research progresses logically from the fundamental characterization of raw materials to the realization of complex multilayered and geometrically integrated absorbers, organized as follows:

- Chapter 2 focuses on the development of the fundamental building blocks, including GNP-based dielectric paints and CIP-based magnetic materials. It investigates the effects of high-energy ball milling on particle morphology and explores the trade-offs between performance and long-term stability in space environments. Intrinsic electromagnetic complex parameters are extracted via Vector Network Analyzer (VNA) and waveguides using a modified Nicolson-Ross-Weir (NRW) algorithm.

- Chapter 3, building on the materials characterized previously, details the fabrication and optimization of composite stacks. Using custom MATLAB algorithms for 1D simulation and CST Studio Suite for 3D full-wave verification, it investigates how stacking dielectric and magnetic layers can resolve impedance mismatch issues and provide frequency-specific optimization (e.g., for 2 GHz and 5.4 GHz).

- Chapter 4 explores the integration of tailored electromagnetic properties into periodic honeycomb geometries for lower C-band mitigation. It details the fabrication of a conformal bilayered system — a magnetic CIP foundation and a dielectric GNP topcoat — to leverage internal internal multiple reflection mechanism. Furthermore, it validates a homogenized equivalent single-layer model against high-fidelity 3D CST simulations using waveguide measurements, ensuring highly volume-efficient aerospace integration.

- Chapter 5 synthesizes the experimental and simulated results, providing a summary of the achievements in EMI mitigation for aerospace applications and outlining future research directions.

References

[1] M. Jaroszewski et al., Eds., *Advanced Materials for Electromagnetic Shielding: Fundamentals, Properties, and Applications*. Hoboken, NJ: John Wiley & Sons, 2019.

[2] J. Gaier, "Radiation protection of new lightweight electromagnetic interference shielding materials determined," NASA Lewis Research Center, Cleveland, OH, 1996.

[3] Q. D. Nguyen et al., "Recent advances in multifunctional electromagnetic interference shielding materials," *Heliyon*, vol. 10, no. 10, 2024.

[4] E. Knott et al., *Radar Cross Section*, 2nd ed. Raleigh, NC: SciTech Publishing, 2004.

[5] W. Salisbury, "Absorbent body for electromagnetic waves," U.S. Patent 2,599,944, Jun. 10, 1952.

[6] K. Vinoy et al., *Radar Absorbing Materials: From Theory to Design and Characterization*. Norwell, MA: Kluwer Academic Publishers, 1996.

[7] Z. Wang et al., "Dielectric and microwave attenuation properties of graphene nanoplatelet–epoxy composites," *AIP Adv.*, vol. 4, no. 1, p. 017139, 2014.

[8] Y. Xia et al., "A review on graphene-based electromagnetic functional materials: Electromagnetic wave shielding and absorption," *Adv. Funct. Mater.*, vol. 32, no. 42, p. 2204591, 2022.

[9] A.R. Ayagara et al. "Polymer Matrix Composite as Radar Absorbent Material in X Band: A Comprehensive Review." *Journal of Science: Advanced Materials and Devices*, 101083, 2025.

[10] A. Gama et al., "Complex permeability and permittivity variation of carbonyl iron rubber composites in the frequency range of 2 to 18 GHz," *J. Aerosp. Technol. Manag.*, vol. 2, no. 1, pp. 59–62, 2010.

[11] Y. Pan et al., "Electromagnetic and microwave absorption properties of coatings based on spherical and flaky carbonyl iron," *J. Mater. Sci.: Mater. Electron.*, vol. 30, no. 19, pp. 18123–18134, 2019.

[12] K. Sun et al., "Core-shell structural design and microwave absorption enhancement of multi-dimensional graphene oxide@polypyrrole/carbonyl iron fiber nanocomposites," *J. Alloys Compd.*, vol. 930, p. 167446, 2023.

[13] W. Zheng et al., "Recent progress in iron-based microwave absorbing composites: A review and prospective," *Molecules*, vol. 27, no. 13, p. 4117, 2022.

[14] J. L. Snoek, "Dispersion and absorption in magnetic ferrites at frequencies above 1 Mc/s," *Physica*, vol. 14, no. 4, pp. 207–217, 1948.

[15] O. Acher et al., "Generalization of Snoek's law to ferromagnetic films and composites," *Phys. Rev. B*, vol. 77, no. 10, p. 104440, 2008.

[16] W. Fu-Sheng et al., "Influence of shape anisotropy on microwave complex permeability in carbonyl iron flakes/epoxy resin composites," *Chinese Phys. B*, vol. 17, no. 6, pp. 2263–2267, 2008.

[17] Z. Cui et al., "Enhanced microwave absorption for high filler content composite molded from polymer coated flaky carbonyl irons modified by silane coupling agents," *J. Wuhan Univ. Technol. – Mater. Sci. Ed.*, vol. 38, pp. 42–51, 2023.

[18] Y. Wu et al., "Electrically aligned $Ti_3C_2T_x$ MXene composite with multilayered gradient structure for broadband microwave absorption," *Nano-Micro Lett.*, vol. 15, p. 110, 2023.

[19] Y. Wang et al., "Simulation-guided design of gradient multilayer microwave absorber with tailored absorption performance," *Macromol. Mater. Eng.*, vol. 309, p. 2400015, 2024.

[20] B. Ji et al., "Microwave absorption properties of multilayer impedance gradient absorber consisting of $Ti_3C_2T_x$ MXene/polymer films," *Carbon*, vol. 181, pp. 130–142, 2021.

[21] Z. Zhang et al., "Gradient carbonyl-iron/carbon-fiber reinforced composite metamaterial for ultra-broadband electromagnetic wave absorption by multi-scale integrated design," *Int. J. Miner. Metall. Mater.*, vol. 30, no. 3, pp. 549–560, 2023.

[22] D. Micheli et al., "Reduction of satellite electromagnetic scattering by carbon nanostructured multilayers," *Acta Astronaut.*, vol. 88, pp. 61–73, 2013.

[23] S. Zheng et al., "Research progress on high-performance electromagnetic interference shielding materials with well-organized multilayered structures," *Mater. Today Phys.*, vol. 40, p. 101330, 2024.

[24] Q. Zhang et al., "Structural design and preparation of $Ti_3C_2T_x$ MXene/polymer composites for absorption-dominated electromagnetic interference shielding," *Nanoscale Adv.*, vol. 5, no. 14, pp. 3549–3574, 2023.

[25] W. Choi et al., "Broadband microwave-absorbing honeycomb structure with novel design concept," *Compos. Part B: Eng.*, vol. 83, pp. 14–20, 2015.

[26] S. Leng et al., "Electromagnetic loss study of honeycomb structured absorbers with a metal substrate," *AIP Adv.*, vol. 13, p. 105226, 2023.

[27] C. Shen et al., "Synergistic integration of CIP and graphene within honeycomb architectures toward high-efficiency electromagnetic wave absorption," *Coatings*, vol. 15, no. 11, p. 1262, 2025.

[28] J. H. Choi et al., "Investigation on microwave absorption characteristics of conductive-coated honeycomb absorber," *Compos. Struct.*, vol. 242, p. 112129, 2020.

[29] Y. He et al., "Preparation and microwave absorption properties of metal magnetic micropowder-coated honeycomb sandwich structures," *Smart Mater. Struct.*, vol. 16, no. 5, pp. 1501–1505, 2007.

[30] J. Liang et al., "Study on microwave absorption performance of the skin-core dual-domain structure constructed with thin-ply laminate and honeycomb," *Polym. Compos.*, vol. 45, no. 9, pp. 8414–8425, 2024.

[31] Y. Xian et al., "A novel frequency-selective surface-enhanced composite honeycomb absorber with excellent microwave absorption," *Polymers*, vol. 16, no. 23, p. 3312, 2024.

[32] J. Feng et al., "Oblique incidence performance of radar absorbing honeycombs," *Compos. Part B: Eng.*, vol. 99, pp. 465–471, 2016.

[33] Y. He et al., "Enhanced microwave-absorbing property of honeycomb sandwich structure with a significant interface effect," *Materials*, vol. 15, no. 16, p. 5741, 2022.

2.

MATERIALS: DEVELOPMENT AND CHARACTERIZATIONS

This chapter details the manufacturing, fabrication, and characterization of composite materials reinforced with Graphene Nanoplatelets (GNP) and Carbonyl Iron Particles (CIP). These fillers are integrated into high-performance polymer matrices specifically selected for aeronautical and astronautical applications, where they serve as critical solutions for Electromagnetic Interference (EMI) mitigation in satellite environments.

The chapter is structured as follows:

- Section 2.1 details the synthesis, fabrication, and characterization of GNP-loaded composites.
- Section 2.2 focuses on the development and characterization of CIP-filled composites.

The resulting physical and electromagnetic data establish the fundamental parameters necessary for the experimental analyses and performance evaluations in subsequent chapters.

2.1 GNP based lossy dielectric paints

In this section, the investigation focuses on the development and characterization of GNP reinforced composites. The electromechanical and electromagnetic properties of GNP dispersed in water-based aeronautical paints (later referred to as AW) have been extensively characterized in previous studies conducted by our research group [1-3]. Building upon that established baseline, this work advances the state-of-the-art by shifting the experimental focus exclusively toward aerospace-grade matrices designated as AZ for the remainder of this study. This dedicated investigation into a diverse matrix is a foundational step, as it provides the necessary data for the subsequent chapter, where a direct comparison between the performance of the two matrix systems will be extensively discussed.

2.1.1 Graphene nanoplatelets (GNP): Intrinsic Properties

Over the past two decades, graphene has emerged as a more intriguing technological solution than other carbon nanomaterials, such as single-walled or multi-walled carbon nanotubes (CNTs) and carbon nanofibers [4, 5]. It offers a superior balance of application versatility, cost-effectiveness, and scalability in production [6].

Structurally, graphene is defined as a monoatomic plane of carbon atoms arranged in a two-dimensional (2D) hexagonal lattice. The atoms are interconnected via strong sp^2 covalent bonds, which bestow the material with exceptional mechanical strength—with a Young's modulus of approximately 1 TPa—high chemical stability, and outstanding electrical conductivity [7]. Within modern materials science, this unique combination of properties yields an unparalleled performance profile that continues to set the benchmark for advanced nanomaterials [8].

The significance of graphene lies primarily in its ability to overcome the traditional thickness limitations of conductive 2D films. In conventional top-down manufacturing, producing ultra-thin continuous layers is often cost-prohibitive due to mechanical lamination constraints. Conversely, bottom-up approaches—such as Chemical Vapor Deposition (CVD)—initially deposit material in isolated islands. In these systems, electrical conductivity is only achieved once the material reaches a critical thickness—the percolation threshold—where these islands merge to form a continuous pathway [9]. For typical metallic films, this threshold is generally around 10 nm; because metallic bonds are non-directional and relatively weak, sufficient bulk material is required to sustain stable electron flow.

Graphene circumvents this bulk requirement entirely. As a zero-bandgap semi-metal, it functions as an exceptional conductor even at the monoatomic scale. However, in practical engineering applications—particularly within macroscopic composite manufacturing—the theoretical ideal of a pristine single 2D sheet gives way to the use of

GNP. These structures consist of short stacks of individual graphene sheets presenting an overall thickness that typically ranges from 3 nm to 100 nm [10].

In practical engineering, the distinction between a single layer and these stacks—specifically the exact ordering of the graphene planes—is often treated as negligible. Differentiating between them requires exhaustive physicochemical analysis, such as Raman spectroscopy or Atomic Force Microscopy (AFM), which is often impractical for large-scale industrial applications. What remains paramount are the intrinsic properties that GNP retain from their single-layer origin, which can be summarized as follows:

- Electronic Excellence: Due to the zero bandgap, electrons behave as massless Dirac fermions [11]. This results in extremely high carrier mobility, allowing for the formation of conductive networks at significantly lower thicknesses and volume fractions than traditional metals.
- High Aspect Ratio: The ratio of the width to the thickness is massive. This platelet geometry is mathematically ideal for percolation, allowing GNP to create a pathway for electricity through a composite matrix even at very low filler loadings [13].
- Mechanical and Chemical Robustness: The sp^2 covalent bonding within each layer makes GNP chemically inert and provides an intrinsic tensile strength of approximately 130 GPa, ensuring the structural integrity and environmental resistance of the resulting material [7].
- Percolation Efficiency: While the layers within a nanoplatelet are held together by weak Van der Waals forces, they can be effectively exfoliated and dispersed during processing. This allows them to form a conductive mesh or network that bypasses the island-formation issues common in CVD-grown metallic layers, ensuring consistent conductivity across the substrate [12].

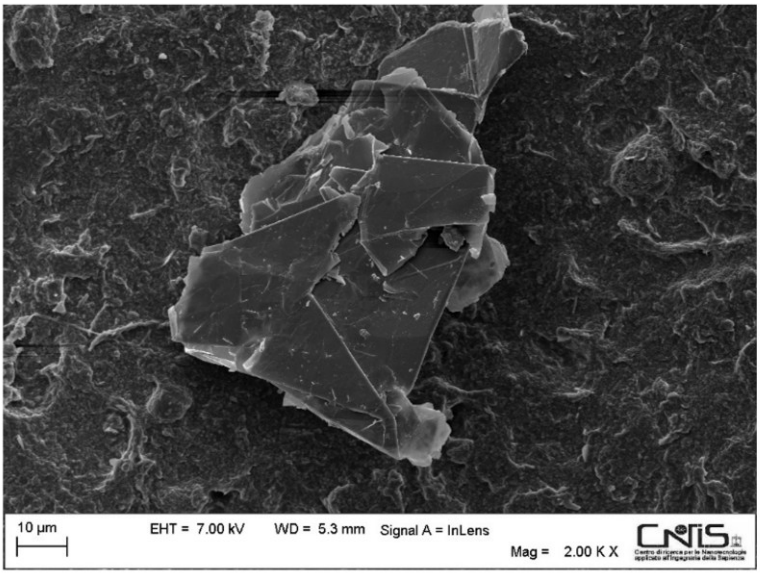

Fig. 2.1 SEM analysis of a graphene nanoplatelet (GNP) structure, illustrating the stacked monolayer architecture and the characteristic high aspect ratio that enables percolation at low filler loadings.

The use of commercial-grade GNPs and liquid-phase processing represents a strategic path toward ensuring industrial scalability and economic feasibility. By favoring accessible techniques like sonication and automated spraying over complex, high-cost methods like CVD, the process becomes highly applicable to both the Italian and global manufacturing sectors. This transition toward more robust and versatile manufacturing protocols allows for a seamless integration into existing industrial lines, reducing the need for specialized cleanroom environments. Such an approach minimizes technical barriers while leveraging graphene’s high percolation efficiency; because target performance is achieved at low filler loadings, the process remains cost-effective and easily integrated into large-scale production without compromising mechanical integrity.

2.1.2 Graphene Nanoplatelets Synthesis and Composite Sample Fabrication

The GNPs utilized in this study were obtained by processing commercial-grade nanoplatelets. To facilitate the exfoliation of the constituent graphene layers, the raw material underwent liquid-phase sonication in acetone. This process was carried out for 20 minutes using a horn sonicator operating on a pulsed cycle (1 s on, 1 s off). To prevent solvent evaporation and avoid localized overheating, the suspension was maintained at approximately 10 °C throughout the procedure. Following this exfoliation step, the samples were thermally treated in an oven at 100 °C for 3 hours to drive off the residual solvent.

Following the exfoliation of the GNP, nanocomposite specimens were prepared using the aerospace-grade polymeric matrix (AZ) at three distinct filler weight fractions: 2 wt%, 3 wt%, and 4 wt%. The GNPs were initially incorporated into the matrix via mechanical mixing, followed by high-shear mixing for 15 minutes. Subsequently, an ultrasonication process was employed to further homogenize the dispersion, during which a solvent thinner was introduced. While the manufacturer’s technical data sheet recommends a thinner concentration between 15% and 20% (initially targeted at the 17.5% median), the addition of GNP—characterized by their high aspect ratio and substantial excluded volume—significantly increased the mixture's viscosity. Consequently, additional thinner was required to achieve the optimal rheological properties. The coating application was executed via airbrushing, an automated plotter system with a parameterized toolpath was employed, ensuring rigorous control over deposition velocity and spray amplitude. This sequential production approach—spanning from the initial GNP exfoliation to the controlled spray deposition—establishes a consistent and scalable framework for developing high-quality, functional nanocomposite coatings.

2.1.3 Morphological characterizations

To validate the effectiveness of the fabrication and homogenization protocols, the morphology and internal structure of the coatings were investigated using Scanning Electron Microscopy (SEM). Surface and cross-sectional analyses allowed for visualizing the internal architecture of the composite, providing a clear comparison between the neat polymer matrix and the GNP-loaded samples. A primary focus of this characterization was verifying the quality of the GNP debundling process by evaluating the homogeneity of the filler distribution. Identifying potential aggregates or clusters is critical, as these formations act as localized defects that adversely affect both mechanical integrity and electrical continuity.

The SEM micrograph obtained at a magnification of 5.00 kX, shown in Fig. 2.2, reveals the fractured surface of the composite, where the exfoliated graphene nanoplatelets are embedded within the polymeric matrix. The image demonstrates a dense, overlapping arrangement of the carbon fillers, confirming the successful creation of a consistent, interconnected network. This structural architecture is essential for reaching the percolation threshold, as the massive aspect ratio of the platelets allows them to create continuous pathways for electron flow even at relatively low filler loadings. Furthermore, the absence of large-scale isolated clusters indicates that the homogenization process effectively prevented the formation of defects that could compromise the material's mechanical and electromagnetic performance. Ultimately, confirming this uniform and isotropic dispersion is paramount, as the nanocomposite’s ability to provide reliable EMI mitigation relies entirely on establishing a consistent filler network throughout the matrix.

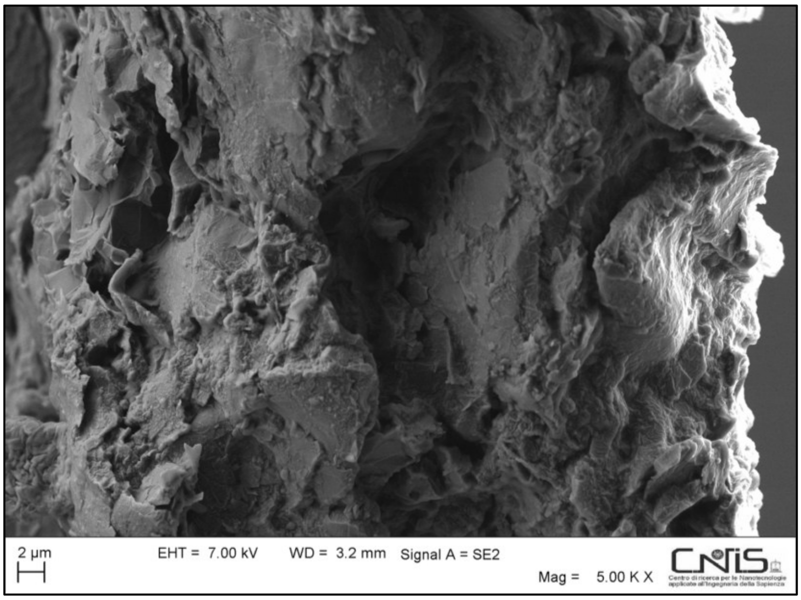

Fig. 2.2 SEM micrograph (5.00 kX magnification) of the fractured cross-section of GNP-loaded AZ paint, showing exfoliated platelets embedded within the polymer matrix and the formation of a dense, interconnected conductive network.

2.1.4 DC electrical conductivity

Complementing the morphological study, the samples underwent electrical characterization to correlate the observed structure with functional performance.

The electrical behavior of nanocomposites is characterized by the percolation curve, which describes the transition of an insulating polymeric matrix into a conductive material as filler concentration increases. This process is governed by the percolation mechanism [9], where a continuous network of conductive filler is established through the matrix in four distinct stages. Initially, a low concentration of nanostructures leaves the composite electrically insulating. As the filler volume content (ϕ) rises, local clusters form and begin to interact through the tunneling effect, leading to a gradual increase in conductivity (γ_C) even before a physical network is fully connected.Once the filler concentration reaches a critical value known as the percolation threshold (ϕ_c), several continuous conductive paths are formed, causing the conductivity to increase by several orders of magnitude. This threshold is influenced by filler geometry, such as particle size and orientation, as well as matrix characteristics like viscosity and crystallinity. In the final stage, additional filler creates further conductive paths until the conductivity levels off at a constant value slightly lower than that of the pure filler. Mathematically, the composite's conductivity follows specific power laws based on its relation to the threshold. When $\phi > \phi_c$ and a network is established, the behavior is described by $\gamma_C = \gamma_p(\phi - \phi_c)^t$, where t is the critical exponent and γ_p is the matrix conductivity. If $\phi < \phi_c$, the tunneling effect governs the material according to $\gamma_C = \gamma_f(\phi_c - \phi)^s$. Directly at the transition point where $\phi \approx \phi_c$, the conductivity is determined by $\gamma_C = \gamma_f^{1-u}\gamma_p^u$, where $u = t/(t+s)$.

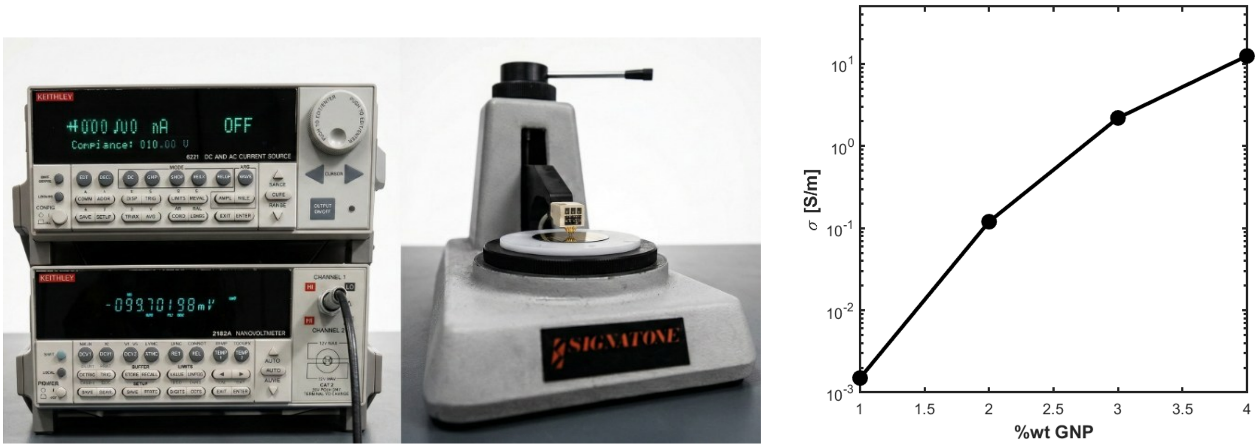

Fig. 2.3 Four-point probe DC resistivity measurement setup (left) and resulting electrical percolation curve (right) as a function of GNP content in the AZ paint.

The resistance of the GNP paint is measured using the four-point probe resistivity measurement system shown in Fig. 2.3, which consists of a Signatone stand connected to a

Keithley 6221 current source and a Keithley 2182A nanovoltmeter. To account for probe and specimen geometry, the measured resistance is multiplied by a correction factor of 4.44 to determine the sheet resistance (R_s). The final electrical conductivity (σ) is then calculated using the formula $\sigma = 1/(R_s \cdot t)$, where t represents the film thickness, typically between 25 μm and 40 μm. The resulting data is plotted to produce the percolation curve reported in Fig. 2.3, which visualizes the relationship between filler concentration and the material's conductive performance.

All measurements were conducted at room temperature (~25°C), which represents standard practice in early-stage materials characterization and provides the reference baseline required for comparison with existing literature. While the intended application of the material in satellite structures implies exposure to a wide operational temperature range (typically −150°C to +150°C), room temperature characterization is an established first step at this stage of development, consistent with a Technology Readiness Level (TRL) 2–3 assessment. The influence of thermal cycling on the electrical properties of the composite — including potential conductivity drift and network stability — is identified as a key direction for future investigation.

While DC conductivity σ provides a fundamental baseline for evaluating material performance, its applicability to AC modeling is contingent upon the dominant conduction mechanism. In the low-frequency regime, especially when the filler concentration is well above the percolation threshold, the established ohmic network allows σ to serve as a reasonable approximation for conductive losses. However, the electrical response is not strictly frequency-independent; as the frequency scales into the microwave and radar bands, displacement currents and dielectric relaxation effects become increasingly prominent. Consequently, while σ accurately describes charge transport through continuous physical pathways, it must be integrated with frequency-dependent parameters to fully characterize the complex relative permittivity at higher frequencies. This frequency-dependent behavior forms the technical basis for the transition into the microwave regime, which is characterized through the following high-frequency analysis.

2.1.5 AC complex relative permittivity measurements

Following the morphological and electrical assessments, the composite samples underwent electromagnetic characterization to extract their complex relative permittivity and permeability. A critical challenge in characterizing thin films via standard coaxial waveguides is their extreme susceptibility to two distinct sources of experimental error: longitudinal positioning uncertainties and radial air gaps. Longitudinal placement errors relative to the calibrated reference planes can introduce severe phase inaccuracies in the measured S-parameters, which mathematically corrupt the parameter extraction. Simultaneously, parasitic radial air gaps between the sample and the inner or outer conductors are known to cause a significant underestimation of the complex relative permittivity at higher frequencies.

To substantially mitigate both issues, a custom measurement framework was commissioned from Genex RF. To limit the longitudinal positioning errors inherent to thin films, a custom coaxial airline was specifically designed with a reduced total length of 10 mm. This shortened physical span grants the operator significantly greater control over the sample's placement within the fixture.

To concurrently address the radial air gap problem, the fabrication of the supporting substrates was entrusted to the same manufacturer. Genex utilized high-precision CNC machining to produce Rexolite substrates tailored to closely match the internal dimensions of the custom airline. By using these precisely toleranced Rexolite rings as the physical guide and foundation for the thin-film sample fabrication, a tight mechanical interface against the conductors was promoted. This integrated manufacturing approach effectively minimized detrimental air gaps at the sample interfaces and helped maintain the required 50 Ω characteristic impedance throughout the structure, leading to highly reliable material parameter extraction.

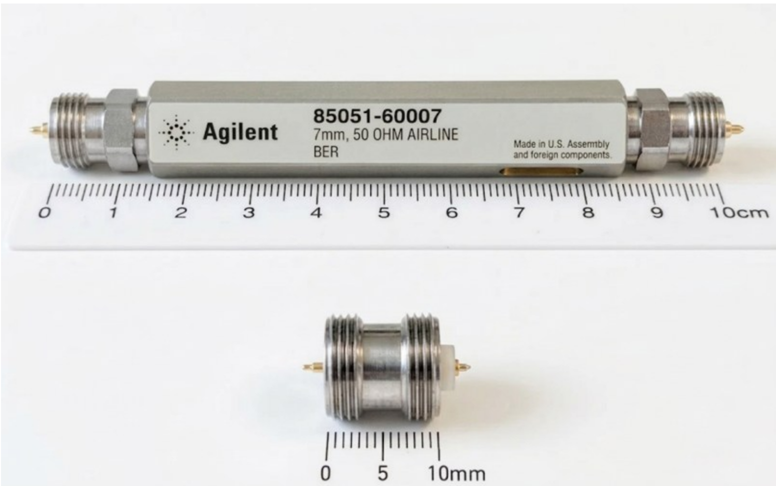

Fig. 2.4 Custom short coaxial airline fixture (active length 10 mm, outer diameter 7 mm, inner diameter 3.04 mm) designed for EM characterization of air-sprayed thin-film composite samples.

The custom airline was interfaced with an Agilent N5245A PNA-X Microwave Network Analyzer and calibrated using an 85050D Short-Open-Load-Thru (SOLT) kit. To characterize the thin films, samples were mounted onto a rigid substrate using double-sided adhesive tape. The measurement protocol followed a sequential approach to isolate the electromagnetic response of the composite, beginning with the bare substrate to verify calibration accuracy. This was followed by measuring the substrate combined with the blank adhesive tape, and finally characterizing the full stack consisting of the substrate, tape, and the sprayed GNP-loaded paint. These preliminary sequential measurements were critical for the mathematical de-embedding of the thin film's intrinsic properties from the overall coaxial fixture, allowing for the precise evaluation of coatings with varying GNP concentrations.

2.1.5.1 Deembedding algorithm and Permittivity Extraction Algorithm

Standard extraction techniques, such as the direct Nicolson-Ross-Weir (NRW) algorithm [13, 14], are highly sensitive to phase errors arising from sample displacement and parasitic air gaps between the sample and the coaxial conductors. Furthermore, for magnetic materials where $\mu_r \neq 1$, the NRW method is prone to numerical instabilities at singularity points, typically occurring when the sample thickness equals an integer multiple of a half-wavelength. At these specific electrical lengths, the measured transmission phase exceeds 2π, triggering the well-known branch ambiguity problem. Because the NRW extraction relies on evaluating the complex logarithm of the transmission coefficient to calculate the wave propagation constant, it is subject to an inherent 2πn phase periodicity. This mathematical ambiguity yields an infinite number of possible roots for the material parameters. If the algorithm cannot correctly identify the appropriate branch index (n), it results in severe, non-physical discontinuities and resonant spikes in the extracted spectra.

To rigorously overcome these phase uncertainties and isolation issues, the measurement setup is analytically modeled as a cascade of transmission line sections. The total internal length of the airline is partitioned into an initial air gap (t_1), the supporting substrate (t_{sub}), the thin film under test (t_{TF}), and a final air gap (t_2). For any individual uniform section i, the electromagnetic wave propagation is described by an ABCD transmission matrix M_i, defined by the following components:

$$A_i = \cosh(\gamma_i l_i) \tag{1}$$

$$B_i = Z_i \sinh(\gamma_i l_i) \tag{2}$$

$$C_i = (1/Z_i) \sinh(\gamma_i l_i) \tag{3}$$

$$D_i = \cosh(\gamma_i l_i) \tag{4}$$

where γ_i and Z_i denote the complex propagation constant and the wave impedance of the specific medium, respectively. To isolate the electromagnetic response of the thin film, a matrix de-embedding procedure is applied. The total measured system matrix, M_{tot}, is defined as the product of these individual cascaded sections:

$$M_{tot} = M_{air}(t_1) \cdot M_{sub}(t_{sub}) \cdot M_{TF}(t_{TF}) \cdot M_{air}(t_2) \quad (5)$$

While the intrinsic electromagnetic properties of the substrate and the air regions are known, the exact longitudinal coordinates t_1 and t_{sub} are subject to micron-scale experimental positioning uncertainties. Furthermore, the thickness of the thin-film sample (t_{TF}), initially determined via standard micrometer measurement, is subject to inherent measurement tolerances. Collectively, these experimental uncertainties necessitate a robust computational solution.

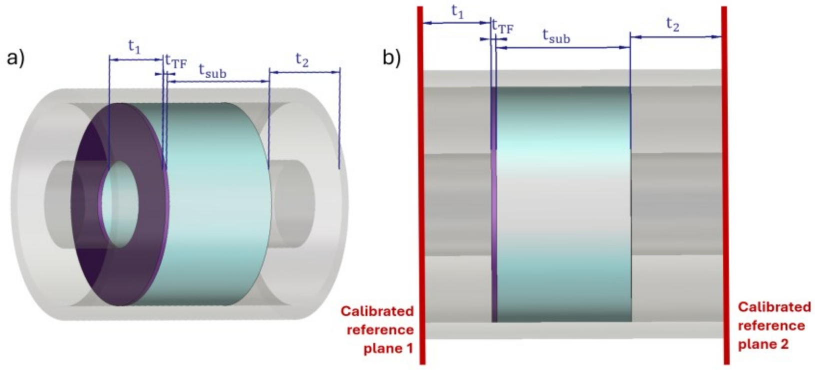

Fig. 2.5 3D CAD of a coaxial airline (a) perspective view (b) section partially filled with thin film and substrate.

To resolve these uncertainties, the developed algorithm performs a parametric sweep over the variables t_1, t_2 and t_{sub} within an iterative optimization loop. For every iteration representing a specific geometric configuration, the analytical air matrices and the previously characterized supporting substrate matrix are mathematically inverted and removed from M_{tot} to extract the isolated ABCD matrix of the thin film, M_{TF}. This isolated matrix is then converted back into the thin film's scattering parameters (S_{11}^{TF} and S_{21}^{TF}).

From these de-embedded parameters, the fundamental NRW variables—the reflection coefficient (Γ) and transmission coefficient (T)—are calculated:

$$X = \frac{(S_{11}^{TF})^2 - (S_{21}^{TF})^2 + 1}{2S_{11}^{TF}} \quad (6)$$

$$\Gamma = X \pm \sqrt{X^2 - 1} \quad (7)$$

$$T = \frac{S_{11}^{TF} + S_{21}^{TF} - \Gamma}{1 - (S_{11}^{TF} + S_{21}^{TF})\Gamma} \quad (8)$$

The effective wavelength inside the material (Λ) is then derived using the unwrapped phase of the transmission coefficient:

$$\Lambda = \frac{-j2\pi l_{TF}}{\ln(T)} \quad (9)$$

The complex relative permeability (μ^*_r) and permittivity (ε^*_r) are extracted using the classical relationships (where λ_0 is the free-space wavelength and $\lambda_c \to \infty$ for the fundamental TEM mode of the coaxial airline):

$$\mu^*_r = \frac{1+\Gamma}{1-\Gamma}\left(\frac{\lambda_0}{\Lambda}\right) \quad \text{and} \quad \varepsilon^*_r = \frac{\lambda_0^2}{\mu_r \Lambda^2} \quad (10)$$

In this specific implementation, since the samples are loaded with a non-magnetic GNP filler, the extraction is stabilized by enforcing the physical constraint $\mu_r = 1$, effectively bypassing magnetic numerical instabilities and the aforementioned branch ambiguity.

To evaluate the validity of each spatial configuration, the extracted parameters are fed back into a forward analytical model. Using the ABCD parameters of the isolated sections, the algorithm reconstructs the theoretical S-parameters for the entire multi-layered stack (S_{ij}^{calc}). The algorithm identifies the optimal physical coordinates by calculating an objective error function, $E(t_1, t_{res})$, which quantifies the deviation between the raw measurements and this reconstructed forward model across the entire frequency range (N_f):

$$E(t_1, t_{res}) = \frac{1}{4N_f}\sum_{k=1}^{N_f}\left(\left|S_{11}^{calc} - S_{11}^{meas}\right| + \left|S_{21}^{calc} - S_{21}^{meas}\right| + \left|S_{12}^{calc} - S_{12}^{meas}\right| + \left|S_{22}^{calc} - S_{22}^{meas}\right|\right) \quad (11)$$

By evaluating this cost function across the defined physical boundaries, the geometric configuration yielding the global minimum error is selected as the true physical state of the measurement setup, ensuring highly accurate and mathematically robust material characterization.

2.1.5.2 GNP-loaded paint complex relative permittivity

As illustrated in Fig. 2.6, the composite samples exhibit a significant increase in both the real part of permittivity, representing energy storage, and the imaginary part, representing dielectric loss, at remarkably low GNP weight fractions. This dual enhancement in the complex relative permittivity components demonstrates superior performance compared to alternative matrices, such as water-based paints, prepared under identical loading protocols [1-3]. This superior electromagnetic response is directly attributable to the chemical formulation; specifically, the use of organic solvents like toluene facilitates the homogenous dispersion and stabilization of the GNPs. This solvent-assisted process prevents particle agglomeration and promotes the formation of a highly efficient, interconnected electrical network throughout the polymer matrix at reduced filler concentrations.

The dielectric characterization of these thin films reveals a strong dependence on filler loading across the 1 GHz to 6 GHz bandwidth. For the 2 wt% and 3 wt% concentrations, the real part of the relative permittivity (ε') remains relatively low and stable, suggesting a regime where the inclusions are well-dispersed without forming a continuous conductive path. In stark contrast, the 4 wt% sample exhibits a dramatic surge in ε', with values starting near 200 at 1 GHz before gradually decreasing toward 170 at 6 GHz.

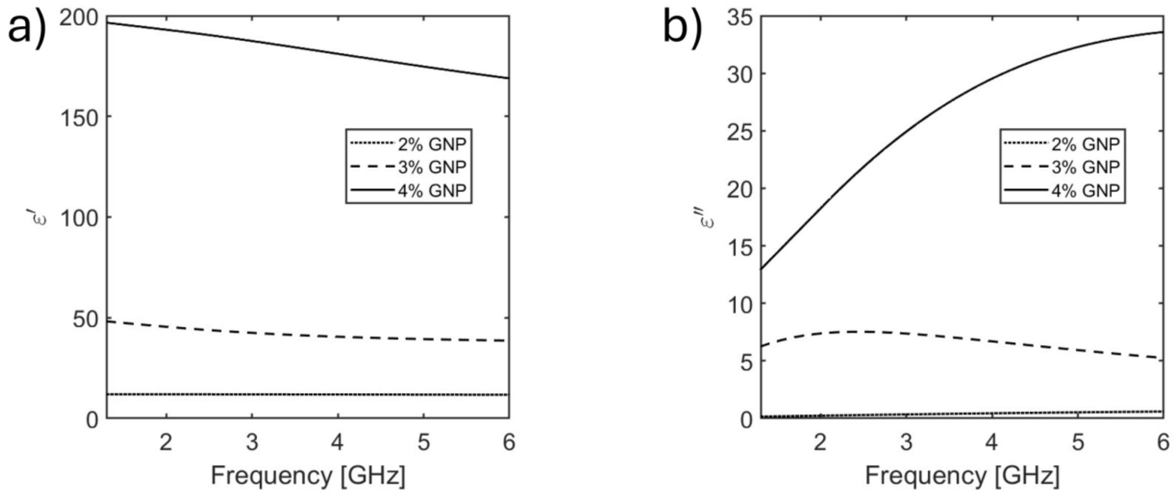

Fig. 2.6 Complex relative permittivity ε′ (a) and ε″ (b) of GNP-loaded AZ aerospace-grade paint at 2, 3, and 4 wt% filler concentrations across the 1–6 GHz range, demonstrating the strong dependence on loading fraction.

The imaginary part of the permittivity (ε'') follows a consistent trend, with the 4 wt% sample displaying significantly higher dielectric losses than the lower concentrations. While the 2 wt% and 3 wt% samples exhibit nearly negligible losses, the 4 wt% sample shows clear dispersive behavior, with ε'' rising from approximately 13 at 1 GHz to a peak of nearly 34 at 6 GHz. The rising slope of the loss factor in this range suggests the onset of significant conductivities and relaxation mechanisms within the percolative network.

Furthermore, the high dielectric contrast between the 4 wt% film and the substrate amplifies the phase uncertainties inherent in thin-film measurements. The successful extraction of these high-magnitude parameters—free from the typical ripples associated with resonance errors—confirms that the iterative optimization and de-embedding methodology established in the previous section is essential for maintaining accuracy as the material properties become increasingly complex and dissipative.

2.2 CIP based magnetic materials

This section details the development and characterization of magnetic materials, structured in two primary phases. First, an investigation into bulky polymeric composites (2 to 4 mm thickness) was conducted. Building on these fundamentals, the research transitions to the characterization of the two distinct grade paints: the water-based "AW" matrix and a "AZ" aerospace-grade paint. This dual-matrix approach identifies the optimal host medium for high-density magnetic fillers by evaluating how different chemical formulations and curing mechanisms influence final magnetic permeability.

2.2.1 Carbonyl Iron Particles (CIP): Intrinsic Properties

To functionalize these matrices, CIP were selected as the primary magnetic reinforcement. Composed of highly pure iron (typically >99% Fe), CIP are widely regarded as the gold standard for radar absorbing applications, particularly when compared to ceramic ferrite-based alternatives. Their primary advantage lies in its exceptionally high saturation magnetization ($M_s \approx 21.5$ kG or 2.15 T), which is nearly an order of magnitude higher than that of soft ferrites ($M_s \approx 3 - 5$ kG). This parameter is physically decisive because, according to Snoek's limit [15], the product of the initial static permeability (μ_i) and the resonance frequency (f_r) is directly proportional to the saturation magnetization:

$$(\mu_i - 1) f_r \propto M_s \tag{12}$$

Consequently, the high M_s of CIP allows the material to maintain a substantial initial permeability over a much broader frequency bandwidth before the inevitable ferromagnetic resonance drop-off occurs. Furthermore, in a satellite scenario, thermal stability is a critical requirement for aerospace payloads. CIP exhibits a Curie temperature (T_c) exceeding $770°C$, ensuring that its magnetic properties remain stable even under the severe thermal cycling of the space environment (typically $-120°C$ to $+120°C$ in LEO). Unlike ferrites, whose magnetic permeability can drift significantly with temperature fluctuations, CIP provides a reliable and consistent magnetic loss mechanism essential for mission-critical absorbing performance [16].

While spherical CIP exhibits excellent saturation magnetization, its performance is physically constrained by the Snoek's limit for isotropic spheres. To overcome this, the material is often processed into a flaky morphology—Carbonyl Iron Flakes (CIF)—to exploit shape anisotropy. The reason of the latter statement is that in magnetic materials, the effective permeability is heavily dependent on the demagnetization factor (N), a geometric parameter determined by the particle's shape. For a spherical particle, the demagnetization factor is isotropic ($N = 1/3$ in all directions), which imposes a stiff penalty on the susceptibility. However, for a thin flake or disk, the demagnetization factor along the planar axis approaches zero ($N \approx 0$). The influence of particle geometry on the static magnetic permeability (μ_s) is described by the following expression, derived from the low-frequency limit of the Landau-Lifshitz equation [17]:

$$\mu_s - 1 \approx \frac{M_s}{H_{an} + NM_s} \tag{13}$$

where M_s is the saturation magnetization and H_{an} is the anisotropy field. By minimizing N through the use of high-aspect-ratio flakes, the term NM_s in the denominator vanishes, leading to a significant enhancement in permeability [18]. Furthermore, this geometric anisotropy allows the material to surpass the conventional Snoek limit, shifting the ferromagnetic resonance to higher frequencies and broadening the effective absorption bandwidth in the GHz range [20].

2.2.2 Bulky polymeric magnetic composites

This section details the development of a magnetically-loaded polymeric matrix, encompassing its fabrication and experimental characterization. This work serves as a preliminary investigation into the behavior of embedded magnetic particles, specifically aiming to establish accurate constitutive parameters for the composite within the S-band. While the actual Telemetry, Tracking, and Command (TT&C) operational frequency band spans 2025–2110 MHz, 2 GHz was selected as a representative sample frequency for this study. These findings at 2 GHz are then integrated into a 3D full-wave simulation of a real satellite cavity, providing a high-fidelity assessment of the material's performance in a practical mission environment.

2.2.2.1 Realization

The fabrication of the magnetically-loaded composites followed a sequential process: first, the morphological transformation of the filler; second, the integration into the polymer; and finally, the precision molding for electromagnetic testing.

To induce the critical morphological transformation described in Section 2.2.1, spherical CIP was subjected to high-energy ball milling, a mechanical attrition technique that utilizes a Retsch Planetary Mill PM 100 to apply intense kinetic impact and shear forces. The planetary motion—characterized by the counter-rotation of the sun wheel and the grinding jar—generates high-magnitude centrifugal forces that drive the transition from native spherical micro-particles into high-aspect-ratio flaky geometries [19]. This shape anisotropy is a technique that allows to overcome the Snoek limit and enhance high-frequency magnetic permeability [20].

A primary technical challenge in processing iron-based powders is their high susceptibility to thermal oxidation. CIP is particularly prone to reacting with atmospheric oxygen during the localized temperature spikes inherent to high-energy milling. Because the formation of iron oxide layers significantly degrades magnetic permeability—a vital parameter for effective satellite-grade EMI absorbance—maintaining chemical integrity is paramount. To mitigate these risks, the milling was executed using a controlled intermittent protocol consisting of 20 minutes of active grinding followed by 10 minutes of cooling and under Argon controlled atmosphere.

The experimental setup was further optimized through the calibration of several interdependent variables. Regarding grinding media dynamics, the diameter and quantity of the grinding balls were selected to maximize the effective contact area, ensuring uniform plastic deformation across the powder batch. Furthermore, the ball-to-powder ratio (BPR) was strategically balanced to optimize energy transfer while maintaining the mechanical stability of the planetary system at high rotational speeds [21]. Temporal control served as the primary independent variable to identify the threshold where particle flattening is maximized before the onset of excessive fragmentation. Following established scientific literature, samples were processed for durations of 3, 6, and 9 hours to evaluate the evolution of the flaky morphology and the refinement of the grain structure [19].

Following the conclusion of the carbonyl iron flakes (CIF) preparation, the fabrication of the composite specimens commenced with the integration of either the as-received spherical CIP or the processed flaky CIF into a high-performance two-part epoxy resin system consisting of Part A (Resin) and Part B (Hardener). A high-shear mechanical mixing approach was employed to ensure each filler particle was fully wetted and to break up any agglomerates, as achieving a homogeneous dispersion is critical for avoiding local clusters that disrupt the electromagnetic response [22]. To meet the rigorous requirements of coaxial airline measurements, the resulting mixture was cast into custom-engineered silicone molds featuring a fixed central pin to ensure accurate annular sample geometry. The inherent flexibility of the silicone allowed for de-molding without distorting the specimens, preserving the strict dimensional tolerances necessary to eliminate air-gap errors during characterization.

Furthermore, to address the density mismatch between the iron fillers and the resin, a dynamic curing protocol was implemented at 60°C for 2 hours. To mitigate particle sedimentation, a systematic inversion strategy was implemented during the initial gelation phase. The process was initially evaluated using 30, 15 and 10-minute flipping intervals; however, these durations proved insufficient to counteract the gravitational settling of the dense metallic fillers. Through iterative testing, a 5-minute inversion cycle was established as the optimal protocol for maintaining a uniform distribution. The efficacy of this 5-minute interval was validated via VNA measurements in the X-band, for the ease of handling of the dimensions of the samples, which demonstrated a high degree of symmetry between the S_{11} and S_{22} parameters. This precise match indicates that the filler-concentration gradient was successfully eliminated, ensuring the structural homogeneity and isotropic electromagnetic properties required for the subsequent case study.

Following the optimization of the flipping timing, annular samples measuring 2 mm and 4 mm in thickness were produced, containing 30, 50, and 70 wt% of either CIP or CIF.

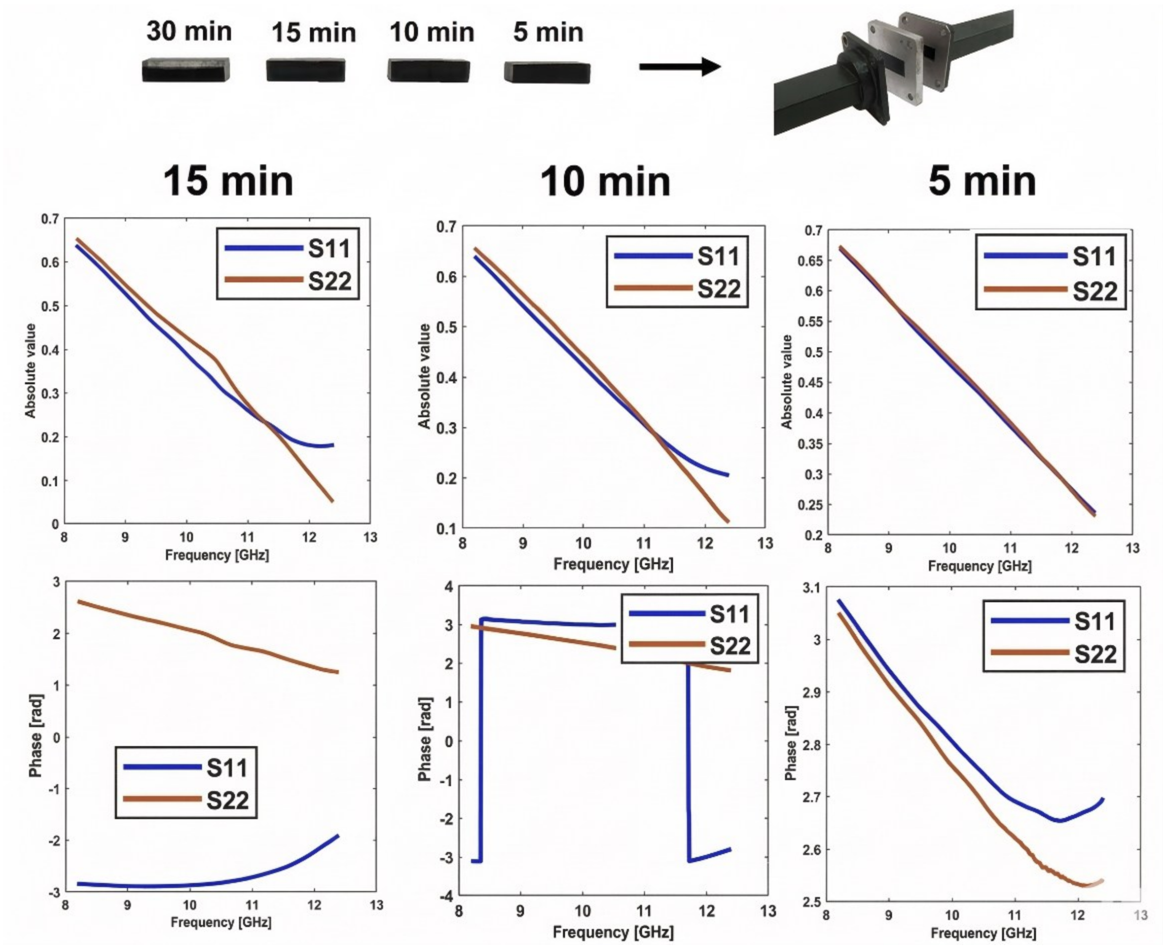

Fig. 2.7 Optimization of the sample flipping procedure for CIP-loaded composites; fabricated samples prepared at varying flipping intervals; sample positioning inside the rectangular waveguide fixture; extracted complex electromagnetic parameters as a function of flipping time, illustrating the convergence toward a homogeneous filler distribution.

2.2.2.2 Morphological characterizations

To evaluate the effectiveness of the mechanical attrition process, a comparative morphological study was conducted between the pristine CIP and the samples processed via planetary ball milling. The evolution of the particle shape and size was monitored using SEM, providing a visual verification of the transition from a three-dimensional spherical geometry to a quasi-two-dimensional flake-like structure. The pristine CIP at zero hours exhibits a characteristic spherical morphology with a smooth surface and a relatively narrow particle size distribution. While spherical particles are isotropic and easy to disperse, they are suboptimal for EMI absorbance due to their low aspect ratio, which requires high filler loadings to reach the electrical percolation threshold.

As shown in the micrographs corresponding to zero, three and nine hours of milling, the mechanical energy from the Retsch PM 100 induces progressive plastic deformation. During the initial flattening phase at three hours, the impact of the grinding media begins to compress the spheres into thick, disc-like structures. At this stage, the overall diameter increases slightly, but the thickness remains significant. The particles begin to exhibit a flake-like morphology, significantly increasing the aspect ratio. By the nine-hour mark, optimized thinning occurs, and the thickness of the flakes is further reduced. This reduction is critical for satellite applications, as thinner flakes increase the specific surface area and enhance the skin effect response.

The characterization highlights a critical trade-off in the milling duration. While the nine-hour samples show the most desirable thinning, the SEM analysis also reveals the onset of

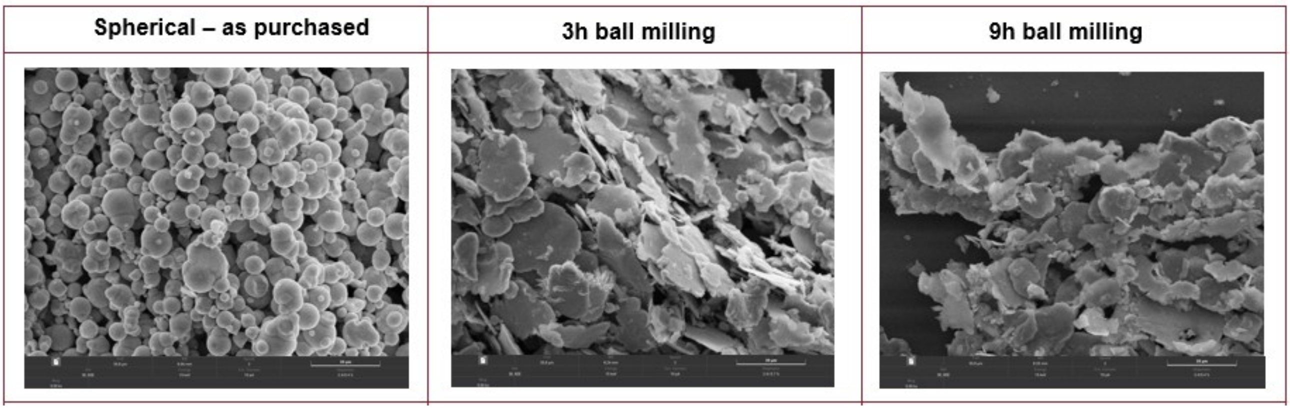

Fig. 2.8 SEM micrographs of carbonyl iron particles following planetary ball milling at (a) 0 h, (b) 3 h, and (c) 9 h, illustrating the progressive transformation from spherical morphology to high-aspect-ratio flake geometry.

excessive miniaturization. Beyond the optimal milling time, the flakes become increasingly fragile; the high-energy kinetic impacts that initially caused flattening begin to induce particle fracture. This fragmentation leads to a reduction in the lateral dimensions of the flakes, effectively lowering the aspect ratio and returning the powder toward a more isotropic (though smaller) state. Therefore, the nine-hour interval was identified as the upper limit for this study, as it represents the point where the thickness is minimized just before significant fragmentation compromises the structural advantages of the flake geometry.

2.2.2.3 Complex relative permeability measurements

To determine the electromagnetic performance of the synthesized composites, a coaxial airline measurement setup was utilized to extract S-parameters across a wide frequency spectrum (10 MHz to 18 GHz) via a vector network analyzer (Agilent N5245A PNA-X), in accordance with the ASTM D5568-08 standard. The fundamental objective was to derive the complex relative permittivity ($\varepsilon^* = \varepsilon' - j\varepsilon''$) and permeability ($\mu^* = \mu' - j\mu''$), which are the critical constitutive parameters governing electromagnetic wave interaction. In this case, these values were extracted using a modified iterative NRW algorithm to provide high-fidelity data for 3D full-wave simulations, modeling EMI suppression within small satellite cavities.

The frequency-dependent behavior of the produced samples, specifically within the 1–8 GHz range (incorporating the S-band), reveals a clear correlation between filler concentration, particle morphology, and electromagnetic response. As illustrated in the following data, a significant enhancement in both ε^* and μ^* occurs as filler loading increases and the particle shape transitions from spherical (CIP) to flake-like (CIF) morphology.

As shown in Fig. 2.9 the superiority of the flake-like morphology (CIF) over the spherical morphology (CIP) is quantitatively evident in the measured electromagnetic parameters. As summarized in the tabulated data at the 2 GHz TT&C representative operational frequency, the CIF composites consistently outperform their CIP counterparts across all weight fractions.

For instance, at a 70% weight concentration, the CIF70 sample achieves a real permittivity (ε') of 7.17 and a real permeability (μ') of 1.53. This significantly outperforms its spherical counterpart, CIP70, which reaches values of only 3.45 and 1.35, respectively. Furthermore, the broadband spectroscopic data from 1 to 8 GHz illustrates that the CIF samples exhibit a pronounced increase in both the real and imaginary parts of complex relative permittivity and relative permeability compared to the CIP samples.

This substantial enhancement is physically justified by the high aspect ratio of the flakes, which allows the composite to surpass the traditional Snoek's limit. This quasi-two-dimensional geometry provides a greater interfacial area and a more favorable alignment for electromagnetic interactions when compared to isotropic spherical particles.

Consequently, integrating a high filler content with a flake-like morphology results in maximized electromagnetic losses and superior absorbance effectiveness. These optimized material properties are particularly critical for ensuring high-fidelity performance at the 2 GHz frequency.

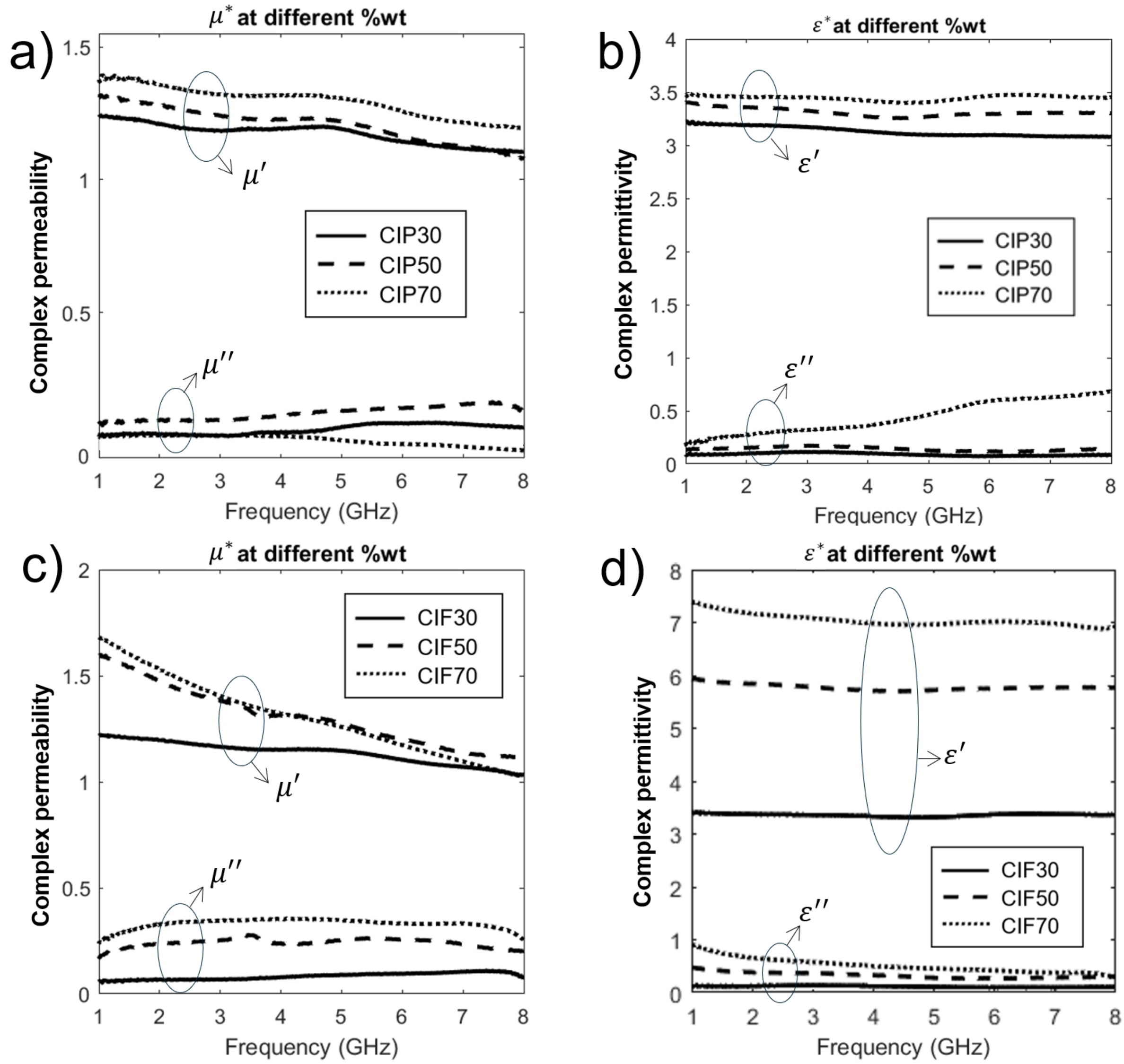

Fig. 2.9 Complex relative permeability μ′ (a) and μ″ (b) of CIP-loaded AZ paint at three filer concentrations, across the 1–8 GHz range, showing the enhancement of magnetic response with increasing degree of flake-like particle morphology.

2.2.2.4 3D full wave simulations: setup and configuration of satellite case study

To bridge the gap between fundamental material characterization and application-level electromagnetic validation, a 3D full-wave frequency-domain simulation was performed using CST Microwave Studio Suite (CST MWS). The simulation geometry replicates a small satellite platform with an overall height of 1 m and a square base of 550 mm × 550 mm. At the heart of this modular satellite design is the tray, the primary structural unit: each tray is populated with components from different subsystems and the individual trays are layered to form the satellite stack, with the entire assembly finalized by the addition of top and bottom closure panels. As illustrated in Fig. 2.10, the platform comprises four such tray modules; this stack-of-trays architecture is commonly employed in the space industry to simplify mechanical assembly, harness routing, and system integration, as further shown in Fig. 2.10b.

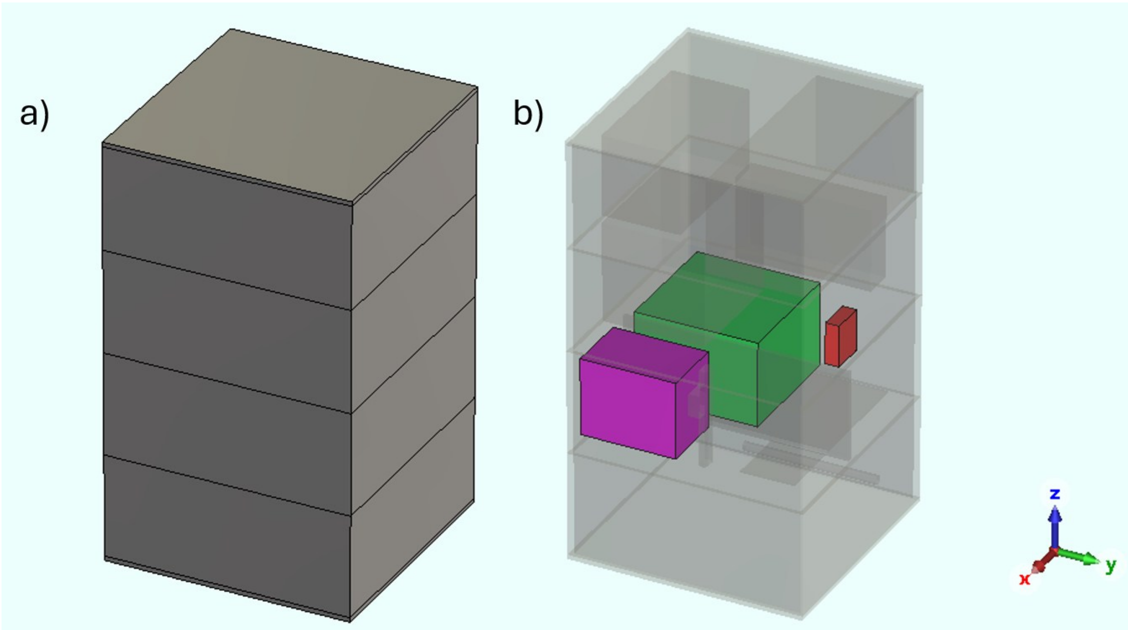

Fig. 2.10 3D full-wave CST simulation model of the modular satellite cavity, replicating a multi-tier stack-of-trays architecture, external (a) and internal view (b).

At the early stages of satellite design the precise radiation mechanism of individual electronic units is generally unknown; a conservative approach is therefore adopted, in which all onboard equipment is assumed to radiate at the maximum level permitted by the applicable standard. Accordingly, the spurious emissions of the killer unit were modelled by means of an equivalent Near Field Source (NFS), implemented in CST MWS as a semi-isotropic radiator. This configuration ensures a spatially uniform electric field magnitude at a reference distance of 1 m from the source across the upper hemisphere, consistently replicating the worst-case far-field emission profile regardless of the actual directivity of the physical unit. The excitation level was calibrated to 77 dBμV/m at 2 GHz in compliance with the ECSS-E-ST-50-05C Rev.2 radiated emission limit for space equipment (Fig. 2.11) [23]. A critical numerical requirement of the Frequency Domain Solver is that the NFS must be supported by a material surface with a well-defined surface impedance; accordingly, the source was placed on a planar boundary assigned the free-space wave impedance of 377 Ω (Fig. 2.12), enabling the solver to correctly compute the surface currents induced by the near-field excitation and propagate the resulting field distribution into the cavity volume.

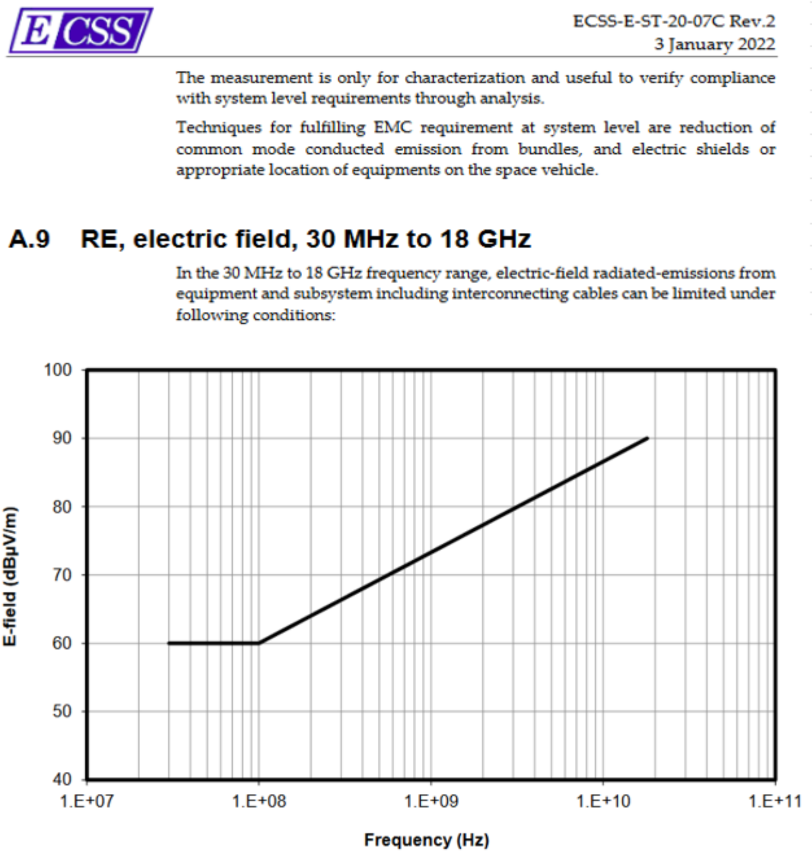
ECSS

ECSS-E-ST-20-07C Rev.2
3 January 2022

The measurement is only for characterization and useful to verify compliance with system level requirements through analysis.

Techniques for fulfilling EMC requirement at system level are reduction of common mode conducted emission from bundles, and electric shields or appropriate location of equipments on the space vehicle.

A.9 RE, electric field, 30 MHz to 18 GHz

In the 30 MHz to 18 GHz frequency range, electric-field radiated-emissions from equipment and subsystem including interconnecting cables can be limited under following conditions:

Fig. 2.11 Emission profile of a unit at 1 m distance: radiated electric field limit per ECSS-E-ST-20-07C Rev.2, Section A.9, in the 30 MHz – 18 GHz frequency range.

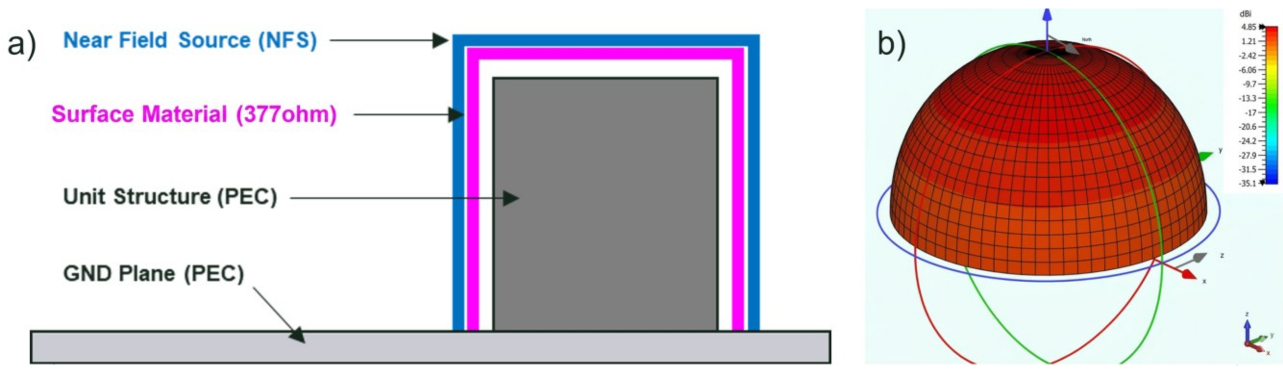

Fig. 2.12 Semi-isotropic Near Field Source (NFS) positioned within the satellite cavity, representing the killer unit excitation at 77 dBµV/m at 2 GHz, with the 377 Ω surface impedance boundary assigned to the source plane (a) and Gain pattern of the semi-isotropic source (b).

Given the strongly resonant nature of the enclosed satellite cavity — characterized by high Q-factor modes and densely packed resonances in the gigahertz range — the Frequency Domain Solver was selected over time-domain alternatives. Unlike time-domain solvers, which integrate Maxwell's equations step-by-step and must propagate the simulation until all resonantly stored energy has fully decayed, the FDS directly computes the steady-state harmonic solution at each target frequency, entirely bypassing the long transients associated with resonant energy build-up and delivering superior numerical efficiency for this class of problem. The spatial discretization was performed using an unstructured tetrahedral mesh, with the maximum cell size constrained to $\lambda/10$ equal to 15 mm, ensuring at least ten cells per wavelength throughout the computational domain (Fig. 2.13a). To establish a conservative upper-bound reference, all cavity walls were assigned PEC boundary conditions, enforcing zero tangential electric field and zero normal magnetic flux density at every surface. This lossless, fully reflective configuration eliminates all wall-absorption losses and maximises the internal field intensity, representing the worst case in terms of resonant field build-up and thereby providing the most demanding test environment against which the attenuation performance of the absorbing coatings can be rigorously benchmarked.

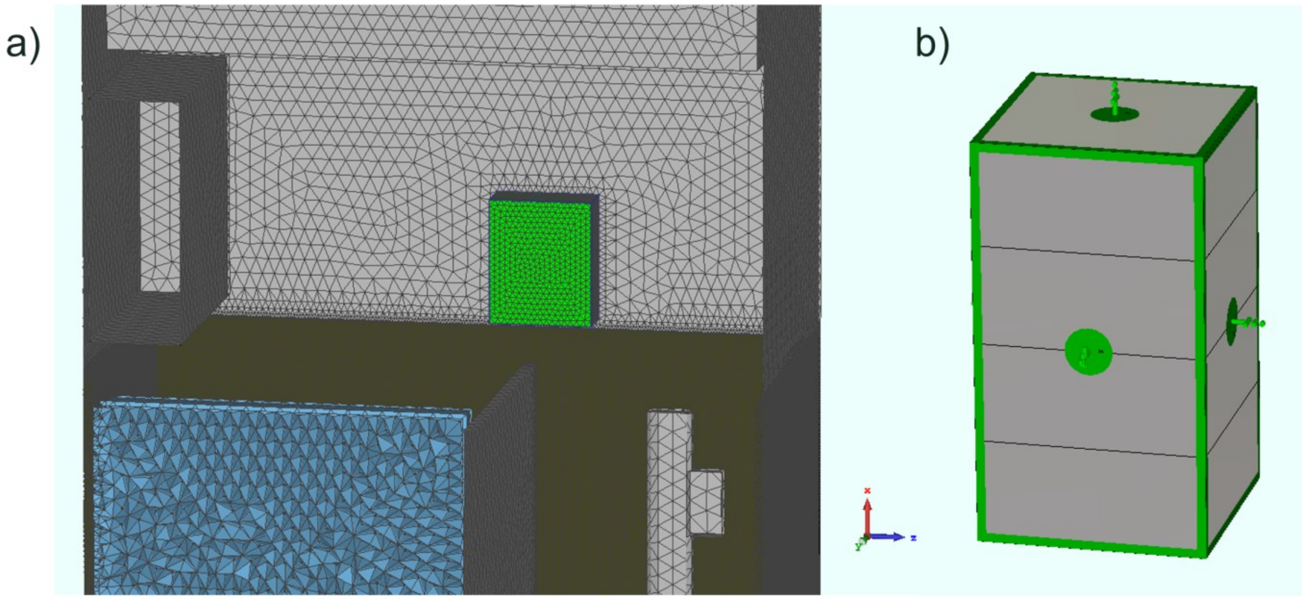

Fig. 2.13 Tetrahedral mesh discretization of the satellite cavity model: (a) full-model mesh overview and (b) detail view of the mesh refinement, with a maximum element size of $\lambda/10$ = 15 mm evaluated at 2 GHz.

2.2.2.5 3D full wave simulations: coated cavity electromagnetic performance

The investigation focused on a specific internal tray module housing both the killer source and a victim unit to quantitatively assess the isolation provided by the applied absorbing layers. To mitigate internal interference, the magnetic coatings were applied directly to the internal walls of this specific tray, as shown in Fig. 2.14b. A comparative analysis was performed by mapping the E-field distribution before and after the application of two distinct magnetic coatings: the optimal composite developed in this study (CIF70) and a benchmark high-permeability material (CIF HP) [24]. The precise values for the complex relative permittivity and permeability of all evaluated samples, including the CIF HP benchmark, are detailed in Table 2.1. These coatings were evaluated at thicknesses of 2 mm and 4 mm to rigorously assess the critical trade-off between maximizing electromagnetic interference (EMI) attenuation and minimizing the strict mass and volume budgets inherent to aerospace engineering. The integration of the magnetically filled polymeric composites into the simulation yielded a quantifiable and significant reduction of the E-field within the satellite cavity.

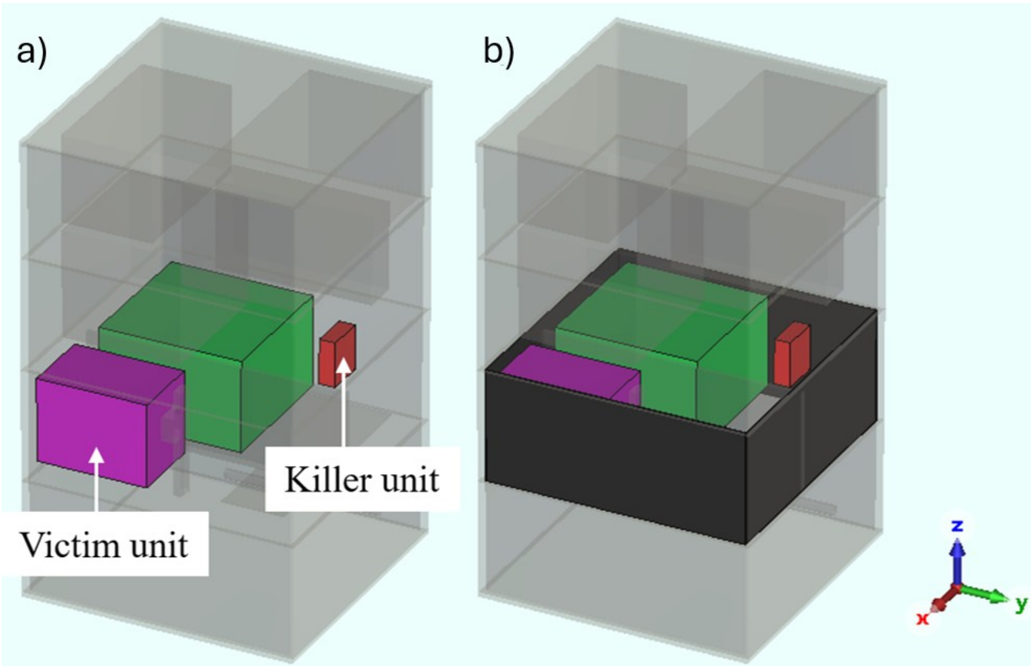

Fig. 2.14 3D full-wave CST simulation CAD view of the killer unit and victim unit (a) and the CIP/CIF loaded polymeric matrix coated tray.

The E-field distribution was extracted from the CST environment as a 3D field map with a discretization step of 3 mm along the $x, y,$ and z axes. For each grid point, the magnitude of the electric field was derived from its complex Cartesian components (E_x, E_y, E_z), accounting for both real and imaginary parts.. The final localized and global metrics were obtained by calculating the arithmetic mean of the field values across the total number of discretized points within the volumes of interest. As illustrated in the field intensity plots (Fig. 2.15), the maximum electric field—measured at the center height of the victim unit—experienced a notable decrease from a baseline of 120 dBμVrms/m down to 113.17 dBμVrms/m following the application of a 4 mm layer of the CIF70 composite. The localized and global attenuation metrics further validate the material's performance. The localized and global attenuation metrics further validate the material's performance, with the 4 mm CIF70 layer achieving a significant localized Module Mean Attenuation of 7.38 dB (Table 2.2) and an overall cavity attenuation of 6.46 dB (Table 2.2). Specifically, Table 2.3 details the mean E-field reduction calculated directly on the surface of the victim unit, demonstrating that the 4 mm layer of CIF70 achieves a significant localized Module Mean Attenuation of 7.38 dB.

Sample	Polymer : Filler	μ* @ 2GHz	ε* @ 2GHz
Polymer	100:0	1 - j0	3 - j0
CIP30	100:30 CIP	1.19 – j0.03	3.19 – j0.12
CIF30	100:30 CIF	1.22 - j0.06	3.45 – j0.09
CIP50	100:50 CIP	1.28 – j0.04	3.35 – j0.15
CIF50	100:50 CIF	1.47 – j0.23	5.84 – j0.38
CIP70	100:70 CIP	1.35 – j0.04	3.45 – j0.3
CIF70	100:70 CIF	1.53 – j0.32	7.17 – j0.65
CIF HP [24]	100:30 CIF HP	3 – j1	10 – j1

Table 2.1. Complex relative permittivity and permeability values of fabricated samples and benchmark material @2GHz.

The E-field distribution maps provide direct, spatially resolved visualization of the mitigation performance and reveal the decisive role of material permeability in enabling thickness reduction. Comparing the uncoated reference (panel a) with the coated configurations (panels b and c) makes the attenuation effect immediately apparent: intense E-field concentrations visible in the uncoated cavity are substantially suppressed in both coated cases. Most significantly, the CIF HP coating (panel b) applied at only 2 mm achieves field attenuation comparable to—and in localized regions exceeding—that produced by the CIF70 coating (panel c) at 4 mm. This performance differential directly results from the markedly different relative permeability values: CIF HP exhibits a real permeability of approximately μ' = 3, roughly double that of CIF70 at μ' = 1.53.

This result is fully consistent with the quarter-wavelength thickness condition, according to which the minimum absorber thickness scales as $d \propto 1/\sqrt{\mu'\varepsilon'}$: the resonant thickness is reduced whenever either the real permeability or the real permittivity — or both — are increased. It is important to note that the CIF HP material presents elevated values of both parameters simultaneously. The combined increase in the product $\mu'\varepsilon'$ from approximately 11 (CIF70) to 30 (CIF HP) translates into a wavelength compression factor of roughly ≈ 1.65, which is broadly consistent with the observed halving of the layer thickness required to achieve comparable attenuation. The E-field maps therefore constitute direct visual evidence of the central design principle of this work: rather than compensating for the volumetric constraints of a satellite platform by accepting thicker absorber layers, the concurrent engineering of both the relative magnetic permeability and the dielectric permittivity of the composite is the operative strategy for achieving equivalent or superior electromagnetic attenuation within a progressively thinner and lighter profile. Increasing the magnetic filler content, optimizing its morphology toward high-aspect-ratio flaky geometries, or adopting benchmark high-permeability materials are therefore the primary levers available to compress the electromagnetic wavelength inside the composite and satisfy the resonance condition at S-band frequencies without violating the strict mass and volume budgets of modern space platforms. The theoretical effectiveness of the coating is intrinsically linked to the wave impedance (Z_w) of the impinging field, which undergoes a significant transition across different field regions. In the far-field, the wave is TEM with a stable impedance of 377 Ω; here, absorption is governed by how closely the coating's intrinsic impedance $\eta = \eta_0\sqrt{\mu/\varepsilon}$ matches that of free space to minimise reflections and maximise power transfer into the absorbing layer. In the reactive and radiating near-field regions, however, the impedance environment departs substantially from this TEM condition. An electric dipole source generates a high-impedance field ($Z_w \gg 377\ \Omega$), dominated by the electric component. To achieve impedance matching in this regime, the material's intrinsic impedance must be correspondingly elevated, which requires a high μ/ε ratio; consequently, permeability is the primary lever governing coupling efficiency, while increasing ε_r alone would in fact lower the intrinsic impedance and worsen the mismatch. Conversely, a magnetic dipole source produces a low-impedance field ($Z_w \ll 377\ \Omega$), dominated by the magnetic component. Here, effective coupling requires a low intrinsic impedance, achieved through a high ε/μ ratio, making permittivity the dominant matching parameter.

Consequently, the localized performance in a satellite cavity — where electronic units may be in close proximity to the walls — is not a static property but a variable of source type and source-shield distance. It is important to note that the semi-isotropic source used in this simulation replicates a conservative far-field profile, and the near-field considerations above therefore constitute a theoretical assessment rather than a direct result of the present model. While this reasoning suggests that the concurrent engineering of both ε and μ may provide broader impedance coverage across a wider range of source conditions, a rigorous quantification of near-field coating performance would require dedicated simulations with elementary electric and magnetic dipole sources at varying separation distances, which lies beyond the scope of the present work.

Sample	Thickness			
	2 mm		4 mm	
	Mean E-Field	Attenuation	Mean E-Field	Attenuation
	[dBuVrms/m]	[dB]	[dBuVrms/m]	[dB]
Without polymer	95.78	0.00	95.84	0.00
Polymer	93.52	2.26	94.20	1.64
CIP30	92.78	3.00	92.95	2.89
CIF30	92.68	3.10	92.43	3.41
CIP50	93.07	2.71	93.50	2.33
CIF50	91.62	4.16	90.33	5.51
CIP70	93.48	2.30	93.59	2.25
CIF70	90.82	4.96	89.38	6.46
CIF HP [24]	88.23	7.55	83.95	11.89

Table 2.2 Quantitative E-field attenuation results from the satellite cavity simulation: localized mean attenuation at the victim unit surface.

Sample	Thickness			
	2 mm		4 mm	
	S/C Mean Attenuation	Single Tray Mean Attenuation	S/C Mean Attenuation	Single Tray Mean Attenuation
	[dB]	[dB]	[dB]	[dB]
Polymer	0.43	0.63	0.51	0.68
CIP30	1.71	1.78	3.03	3.58
CIF30	1.40	1.47	2.45	2.87
CIP50	1.12	1.18	2.00	2.40
CIF50	3.18	3.48	5.47	6.40
CIP70	1.10	1.12	2.12	2.60
CIF70	3.96	4.39	6.35	7.38
CIF HP [24]	6.90	8.12	10.15	11.76

Table 2.3 Quantitative E-field attenuation results from the satellite cavity (S/C) simulation: global cavity and single tray-mean attenuation.

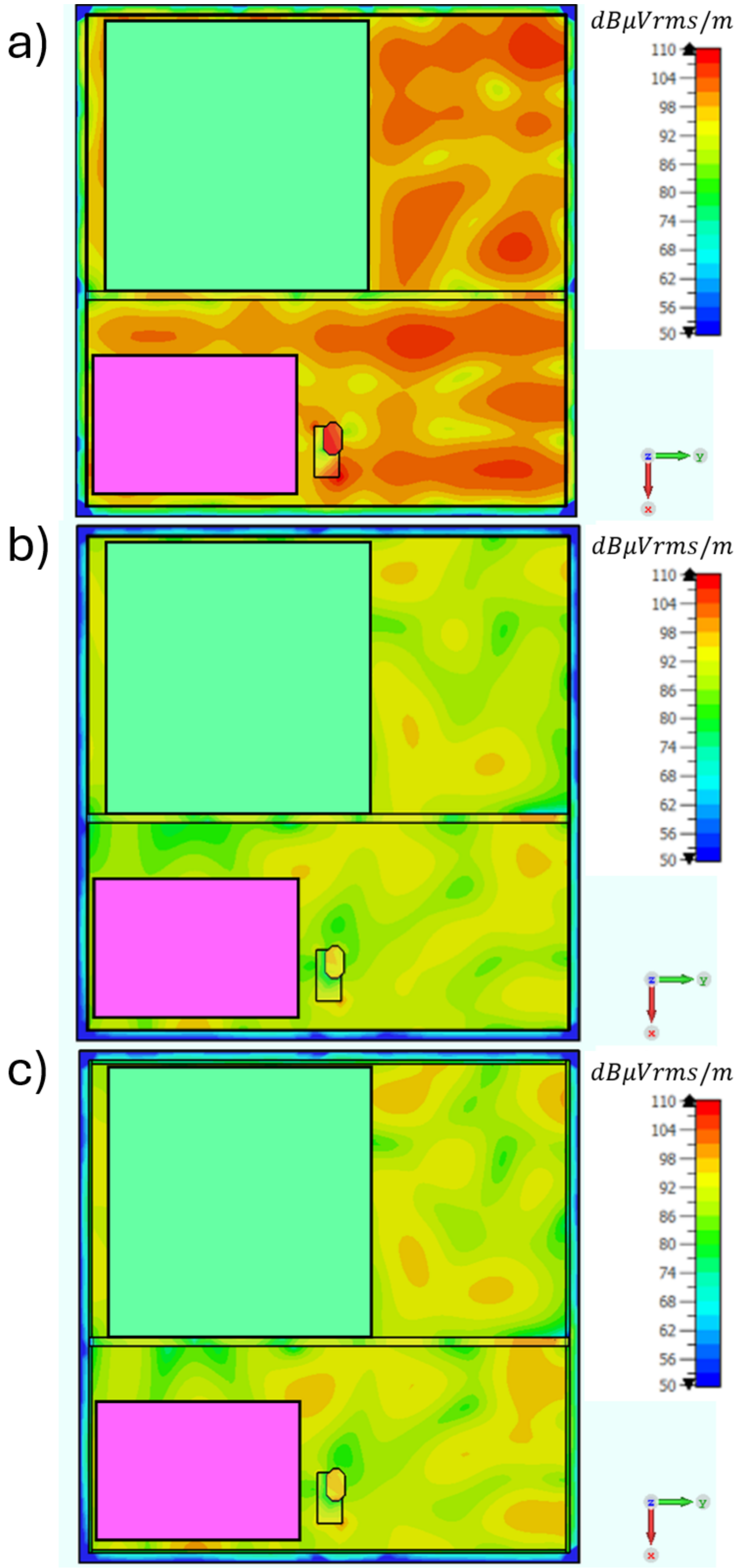

Fig. 2.15 E-field distribution maps of the (a) no coating applied case, (b) 2 mm CIF HP coating and (c) 4mm CIF70 coating.

2.2.2.6 CIF Oxidation

Despite the theoretical electromagnetic advantages traditionally associated with flaky morphologies — most notably the ability to surpass Snoek's limit through shape anisotropy — a dedicated experimental campaign was conducted to rigorously assess whether carbonyl iron flakes (CIF) could deliver a meaningful and reliable increase in effective relative permeability within the constraints of a space-qualified workflow. This investigation was not taken for granted: the potential performance gains warranted a direct empirical assessment before any conclusions could be drawn.

The SEM micrographs at 80,000x magnification, however, provided decisive and unambiguous results. The CIF particles exhibit a rough, granular surface texture that is a hallmark of rapid, exothermic oxidation occurring when high-aspect-ratio flakes are exposed to the atmosphere — clear morphological evidence of an extensive oxidative process and the subsequent formation of non-magnetic oxide layers compromising the functional core of the material.

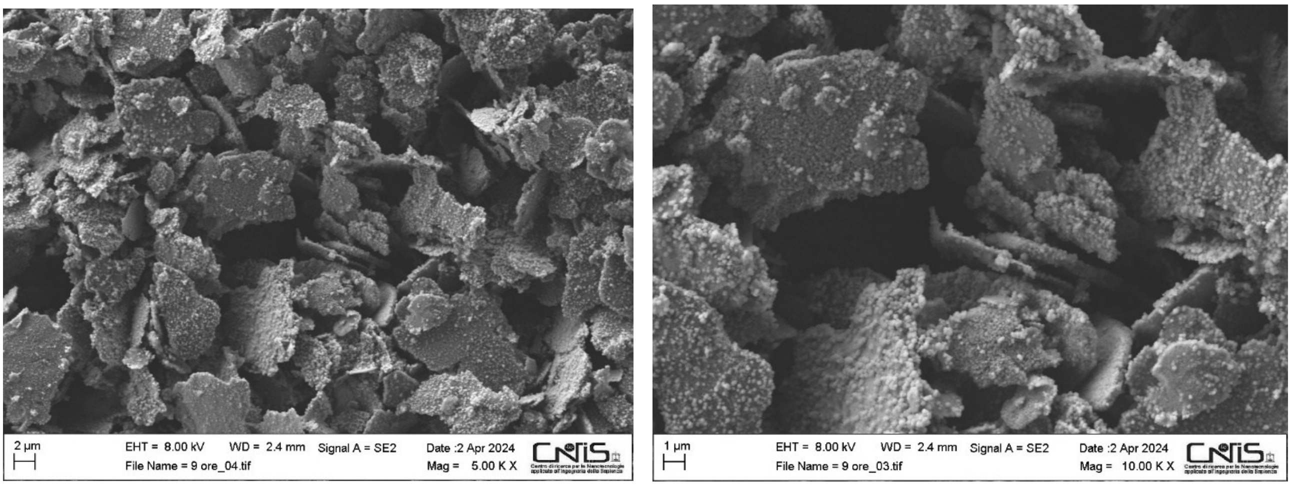

Fig. 2.16 SEM micrograph of ball-milled CIF particles, revealing surface structural degradation and the onset of oxidation.

The integrated SEM-EDS, in Fig. 2.17, analysis provides definitive chemical confirmation of this instability. The EDS spectra show prominent oxygen peaks alongside the primary iron signals, directly demonstrating the formation of non-magnetic iron oxide phases that degrade intrinsic magnetic performance and permeability. Detections of carbon and nitrogen are also observed, likely stemming from atmospheric exposure and residual processing solvents used during the flake recovery phase, while a small silicon peak is attributed to substrate artifacts or trace impurities introduced during milling.

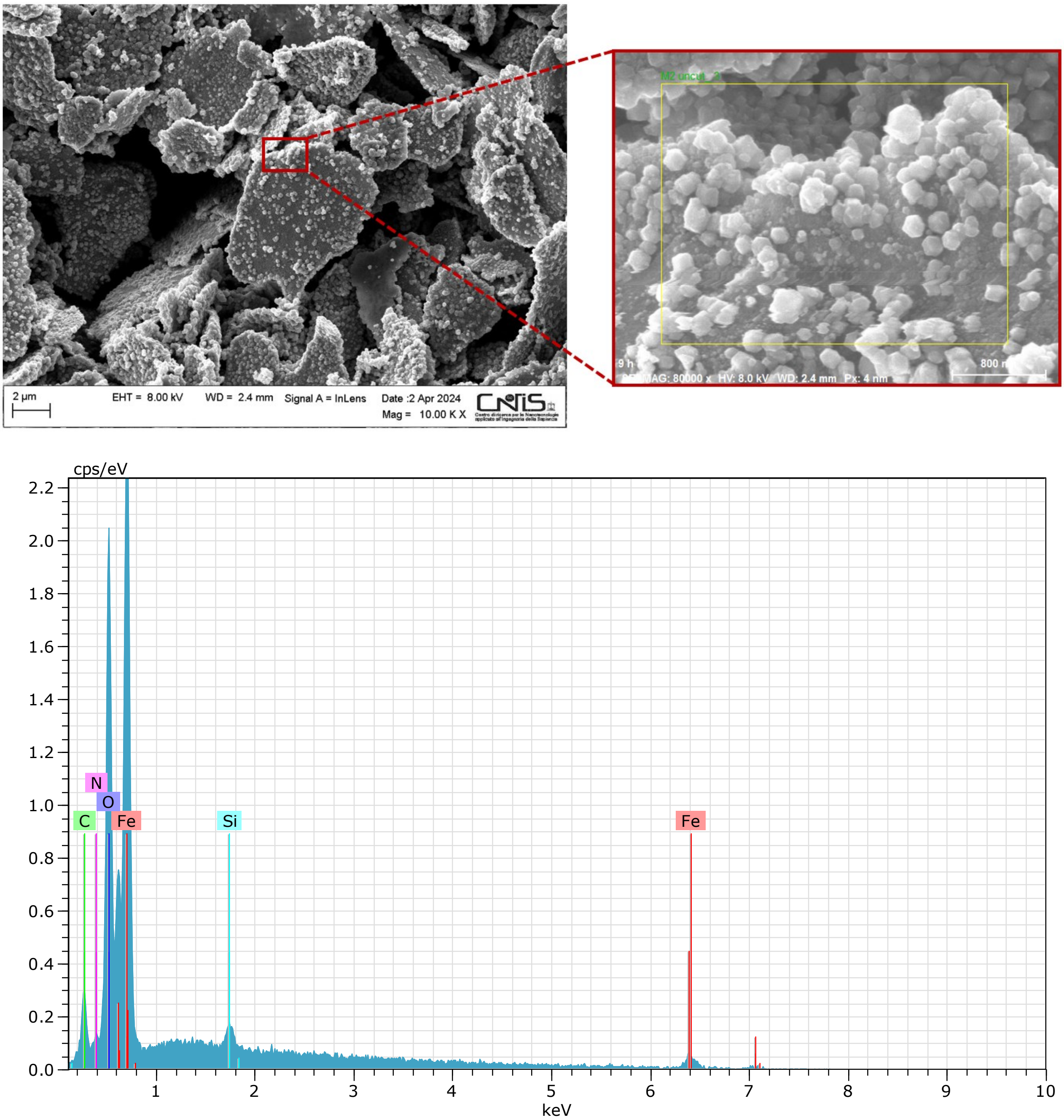

Fig. 2.17 SEM of ball-milled CIF particles confirming iron oxidation: (a) secondary electron image; (b) EDS elemental maps.

This degradation is a direct and unavoidable consequence of the fabrication process itself. While planetary ball milling is conducted under a strictly controlled Argon atmosphere, the extreme mechanical energy involved renders the resulting high-aspect-ratio flakes highly metastable. Upon opening the milling vessel — even after temperature stabilization — exposure to the atmosphere during cleaning and recovery triggers rapid, exothermic oxidation. This phenomenon is drastically exacerbated by the large specific surface area inherent to the flaky geometry, which provides a significantly greater number of reactive sites than the original compact spherical form.

From an electromagnetic perspective, the experimental results confirm that while CIF does produce a measurable increase in complex relative permeability through shape anisotropy, the magnitude of this improvement is consistently overshadowed by the chemical instability of the material. In the context of space applications, this trade-off is unacceptable: a partially oxidized filler would fail the stringent qualification requirements for spaceflight, as the oxide layer degrades both magnetic performance and long-term chemical stability of the coating. Materials intended for Low Earth Orbit must furthermore withstand severe thermal cycling — typically ranging from −100°C to +100°C — without property drift or mechanical failure of the film, a demand that the metastable flake morphology cannot reliably meet.

This experimental campaign therefore served its purpose: it established, through direct physical evidence, that the performance gains of flaky morphology cannot be decoupled from their fabrication-induced degradation under industrially realistic conditions. Spherical CIP, by contrast, presents a minimal surface-area-to-volume ratio that significantly reduces oxygen adsorption and lattice degradation. Its compact, mechanically unaltered structure maintains saturation magnetization over time and across long-duration mission cycles, making it the only morphology compatible with a reliable, space-qualified workflow.

Consequently, rather than pursuing further morphological optimization — which this investigation demonstrated to be an unreliable pathway under current processing conditions — the strategy is redirected toward exploring the application of two different host matrices for spherical CIP-based composites. It cannot be excluded that alternative processing methodologies might enable the implementation of flaky morphologies, but within the constraints of existing manufacturing capabilities, this work proposes a comparative study assessing whether the binder environment represents a viable degree of freedom for tuning the effective relative permeability of the composite while preserving the material purity and environmental stability required for spaceflight qualification.

2.2.3 Magnetic coatings

As established in the preceding analysis, the subsequent phase of this research focuses on the integration of the magnetic filler into polymeric paint matrices. Because the severe oxidation issues and structural degradation associated with the flake morphology render it unviable for long-term spaceflight applications, this integration phase strictly utilizes the chemically stable, spherical CIP. The chosen host materials for this dispersion are the two specialized, high-performance polymeric matrices: the aeronautical-grade AW system and the aerospace-grade AZ system. To systematically characterize the electromagnetic and mechanical performance of these newly developed composites across a comprehensive range of magnetic loadings, test samples were formulated and fabricated at distinct filler concentrations of 30, 50, and 70 percent by weight (wt%).

2.2.3.1 Fabrication of Magnetic Coatings

The fabrication protocol started with the weighing and proportioning of the constituents. The spherical CIP was systematically incorporated into the liquid matrices of both the AW and AZ systems to achieve the targeted filler concentrations of 30, 50, and 70 wt%. Given the high specific gravity of the metallic iron fillers maintaining a stable, agglomeration-free suspension within the polymer resin was a critical challenge. To achieve a homogeneous dispersion and prevent the premature sedimentation of the dense particles, the composite mixtures underwent a vigorous homogenization sequence, combining continuous mechanical stirring with high-shear mixing techniques.

Immediately following this homogenization phase, the coating deposition was executed via controlled, manual airbrushing onto a planar substrate to form a uniform film. A manual application approach was deliberately chosen over an automated plotter system to strictly minimize the latency period between mixing and deposition. This rapid protocol was critical to prevent the rapid sedimentation of the high-density magnetic particles at the bottom of the suspension, ensuring that the uniform dispersion achieved during mixing was effectively locked in place throughout the subsequent curing process.

Once fully cured, the solid composite films were carefully detached from the substrate and subjected to a high-precision mechanical shaping process to meet the stringent dimensional tolerances required for the coaxial airline measurement fixture (ASTM D5568-08). The inner diameter (D_{int} = 3.05 mm) was established using a precision vertical drill press, ensuring perfect coaxial alignment with the inner conductor of the measurement setup. Subsequently, the outer diameter was modulated to exactly 7.00 mm using a calibrated blade cutting system driven by a rigid guide. This highly controlled machining setup ensured exceptional concentricity and edge fidelity, minimizing air gaps between the sample and the walls of the sample holder—a critical factor for the accurate extraction of the material's intrinsic electromagnetic parameters.

2.2.3.2 Morphological Characterization of Magnetic Coatings

To validate the efficacy of the dispersion protocol and assess the interfacial compatibility between the magnetic filler and the polymeric host, a rigorous morphological characterization of the cured magnetic coatings was performed. SEM was employed to analyze the cross-sectional fracture surfaces of the composite films. As illustrated in the micrograph of the CIP-loaded matrix, the CIP unequivocally retains its pristine spherical morphology post-processing. Unlike the severe structural degradation and granular texturing previously observed in the mechanically milled flakes, the spherical CIP particles maintain smooth, intact surfaces. This visual evidence confirms the absence of process-induced oxidation or mechanical fracture during the vigorous high-shear mixing phase.

Furthermore, the SEM analysis provides critical insights into the internal microarchitecture of the resulting composite. The micrograph reveals the dense metallic spheres firmly embedded within the continuous polymeric phase. While isolated instances of close-proximity particle clustering are visible—a well-documented phenomenon driven by the inherent magnetic dipole-dipole interactions of the iron cores at elevated weight fractions—the host matrix demonstrates adequate wetting of the filler. The robust encapsulation of the spherical particles within the resin network suggests strong interfacial adhesion. This structural integrity is fundamental for ensuring the long-term thermomechanical stability of the coating under the rigorous environmental conditions of LEO, ultimately validating the strategic decision to utilize spherical CIP for a stable, space-qualified EMI absorbing structure.

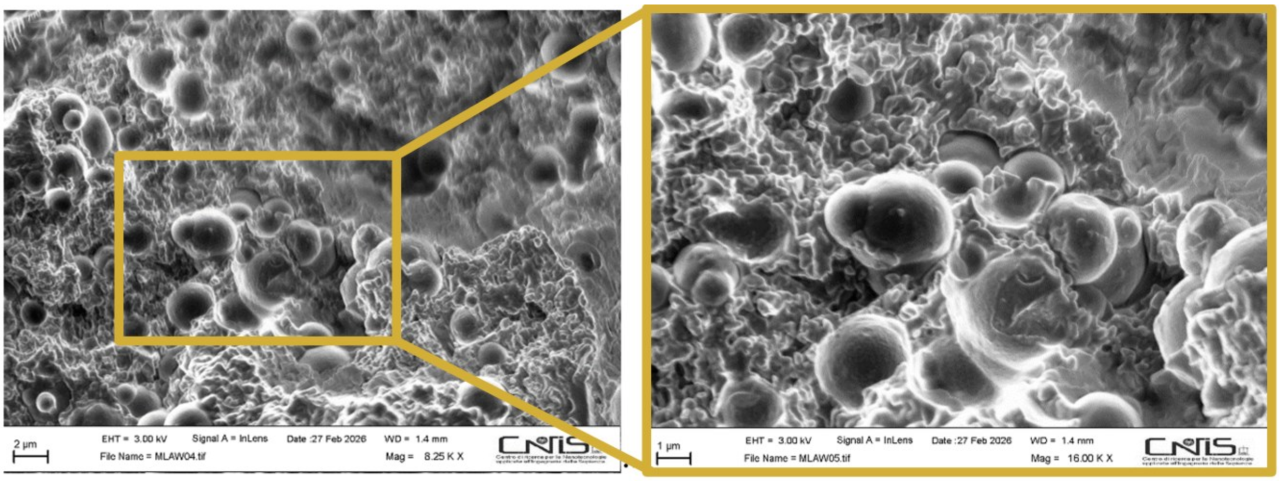

Fig. 2.18 SEM cross-section micrograph of CIP-loaded AZ paint coating, showing the homogeneous distribution of spherical carbonyl iron particles within the polymer binder matrix and the absence of significant agglomeration at two different magnifications: 8.25 K X (left) and 16.00 K X (right).

2.2.3.3 Electromagnetic Characterization of Magnetic Coatings

Unlike the purely dielectric GNP-loaded films characterized in Section 2.1.5.1, for which the assumption of unity permeability ($\mu_r = 1$) constitutes a physically grounded simplification, the characterization of CIP-loaded thin films demands the simultaneous extraction of both complex relative permittivity (ε^*) and permeability (μ^*) — as the magnetic filler fundamentally alters the permeability response and renders a scalar dielectric description insufficient. Fig. 2.19 and Fig. 2.20 present the results for the complex relative permittivity and permeability of the AW and AZ paints, respectively; in Fig. 2.19, it is observed that CIP within the water-based paint demonstrates an increase in EM parameters proportional to the filler amount, however, when comparing these results with the AZ parameters in Fig. 2.20, the significantly higher values of complex relative permeability in the aerospace-grade matrix become the defining differentiator. The extracted constitutive parameters for both the water-based (AW) and aerospace-grade (AZ) matrices demonstrate the significant impact of matrix chemistry and filler concentration on the electromagnetic profile of the composites, correlating the measured ε and μ with the theoretical principles of dispersion and interfacial wetting. The results for the AW matrix (Fig. 2.19) reveal a consistent, predictable increase in both permittivity and permeability with higher filler loading, though the magnitude of these parameters suggests certain limitations inherent to the aqueous host where the real permittivity (ε′) at 70 wt% starts at approximately 9.5 and exhibits a gradual decline across the 2–18 GHz range while the dielectric loss (ε″) remains relatively low, peaking near 3.5. Furthermore, the magnetic response in the AW matrix is relatively constrained, with μ' for the 70 wt% sample failing to exceed 1.9 at low frequencies and the broad, low-amplitude magnetic loss (μ″) indicating that while CIP provides a reliable loss mechanism, the AW matrix may harbor microscopic air voids which effectively lower the macroscopic magnetic induction through increased demagnetization. In contrast, the AZ matrix (Fig. 2.20) demonstrates a markedly superior electromagnetic performance, particularly regarding magnetic permeability, validating the decision to utilize a more chemically aggressive organic host for satellite applications; while the ε′ values are comparable to the AW matrix (peaking just above 9 for 70 wt%), the dielectric loss (ε″) profiles are more pronounced and better defined, suggesting a more homogeneous distribution of the CIP fillers and reduced localized agglomeration. A significant disparity is observed in the magnetic properties as the 70 wt% AZ sample achieves a μ′ of approximately 3.3 at 2 GHz—nearly 1.7 times higher than the equivalent AW sample—and the magnetic loss (μ'') for the AZ matrix shows a clear, well-defined relaxation peak near 4 GHz, which, compared to the flatter response of the AW matrix, is a strong indicator of superior interfacial wetting that allows the CIP particles to interact more efficiently with the magnetic component of the RF field by eliminating air voids at the polymer-iron interface.

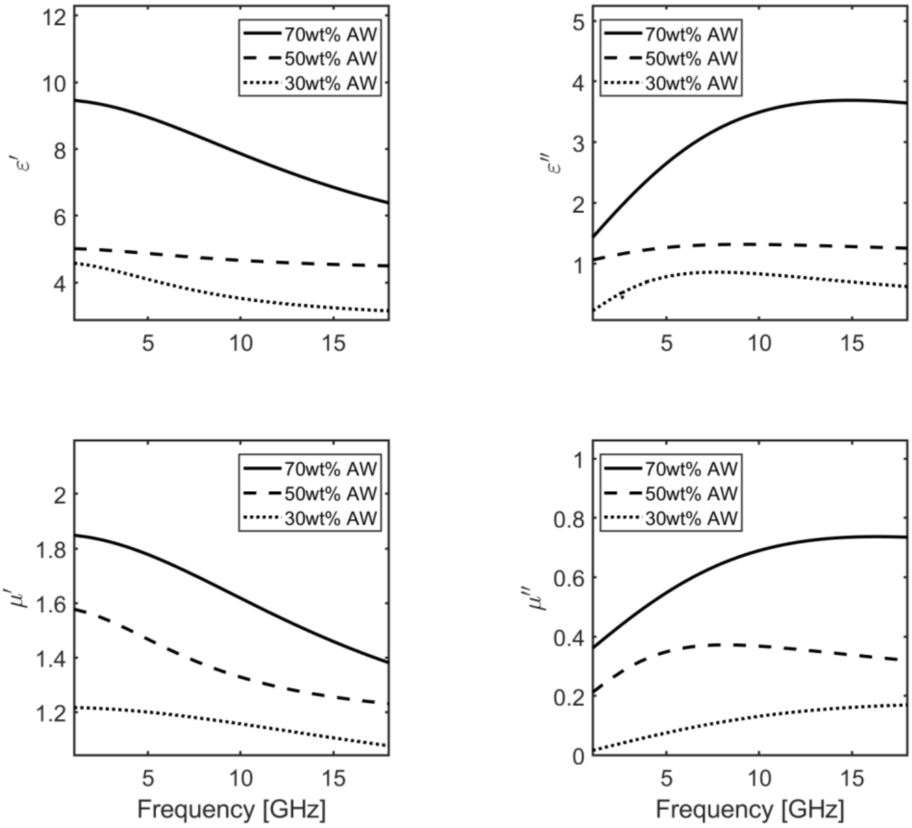

Fig. 2.59 Complex relative permittivity (a, b) and permeability (c, d) of 30, 50, 70 wt% water-based CIP-loaded paint (AW).

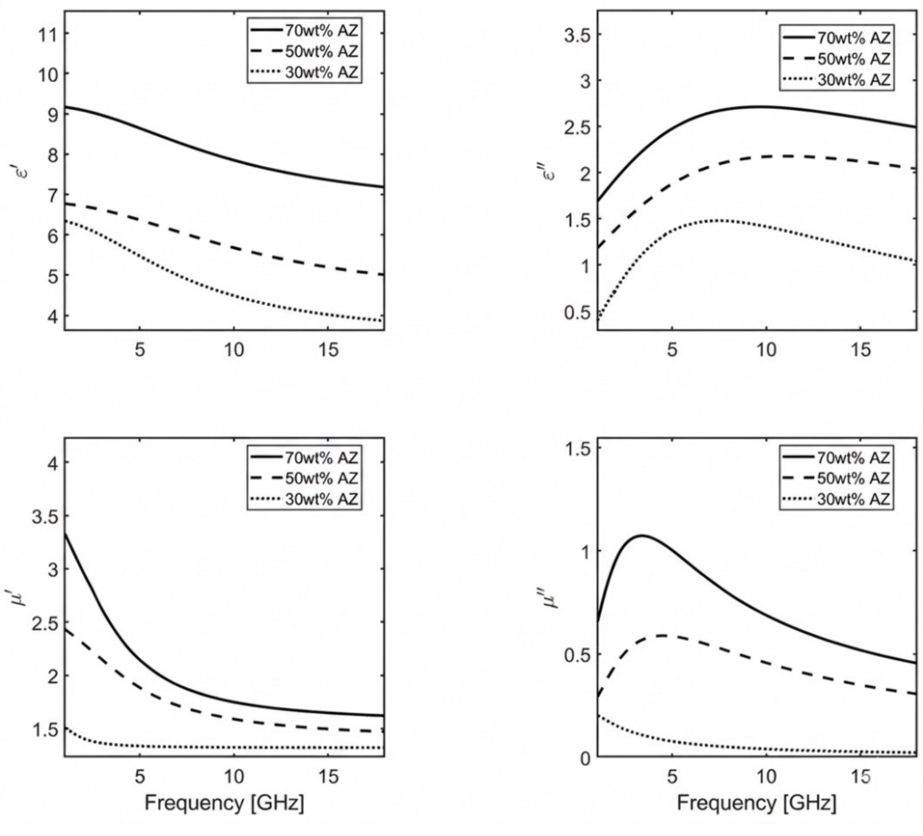

Fig. 2.20 Complex relative permittivity (a, b) and permeability (c, d) of 30, 50, 70 wt% aerospace-grade CIP-loaded paint (AZ).

2.3 Conclusions

This investigation successfully established a comprehensive suite of functional composite paints tailored for electromagnetic absorption applications. Through the systematic loading of CIP and GNP into AZ and AW matrices, a suite of functional materials was successfully developed for use in subsequent absorbing structures. These AZ and AW formulations demonstrated the necessary stability and loading capacity to achieve the electromagnetic profiles required for high-performance applications.

While the incorporation of CIF was intended to enhance μ, the experimental results indicated that this modification did not yield the desired magnetic improvement under the tested conditions. Nevertheless, the implementation of a matrix sweep using an organic solvent proved effective in optimizing the composite environment and addressing interface limitations.

These characterized materials now provide the foundational data required for the next phase of the research. The focus will now shift from individual material characterization to the practical application and performance testing of these composites within integrated absorbing structures.

References

[1] M. S. Sarto et al., "Water-based piezoresistive conductive polymeric paint containing graphene for electromagnetic and sensor applications," 2016.

[2] F. Cozzolino et al., "New sensing and radar absorbing laminate combining structural damage detection and electromagnetic wave absorption properties," *Sensors*, vol. 22, no. 21, p. 8470, 2022.

[3] A. Rinaldi et al., "Graphene-coated honeycomb for broadband lightweight absorbers," *IEEE Trans. Electromagn. Compat.*, vol. 60, no. 5, pp. 1454–1462, 2017.

[4] S. Chatterjee et al., "Comparing carbon nanotubes and graphene nanoplatelets as reinforcements in polyamide 12 composites," *Nanotechnology*, vol. 22, no. 27, p. 275714, 2011.

[5] C. Soldano et al., "Production, properties and potential of graphene," *Carbon*, vol. 48, no. 8, pp. 2127–2150, 2010.

[6] A. C. Ferrari et al., "Science and technology roadmap for graphene, related two-dimensional crystals, and hybrid systems," *Nanoscale*, vol. 7, no. 11, pp. 4598–4810, 2015.

[7] C. Lee et al., "Measurement of the elastic properties and intrinsic strength of monolayer graphene," *Science*, vol. 321, no. 5887, pp. 385–388, 2008.

[8] D. G. Papageorgiou et al., "Mechanical properties of graphene and graphene-based nanocomposites," *Prog. Mater. Sci.*, vol. 90, pp. 75–127, 2017.

[9] J. Li and J. K. Kim, "Percolation threshold of conducting polymer composites containing 3D filler networks," *Compos. Sci. Technol.*, vol. 67, no. 10, pp. 2114–2120, 2007.

[10] J. R. Potts et al., "Graphene-based polymer nanocomposites," *Polymer*, vol. 52, no. 1, pp. 5–25, 2011.

[11] A. C. Neto et al., "The electronic properties of graphene," *Rev. Mod. Phys.*, vol. 81, no. 1, p. 109, 2009.

[12] R. Jan et al., "High aspect ratio graphene nanosheets cause a very low percolation threshold for polymer nanocomposites," *Acta Phys. Pol. A*, vol. 129, no. 4, pp. 478–481, 2016.

[13] A. M. Nicolson and G. F. Ross, "Measurement of the intrinsic properties of materials by time-domain techniques," *IEEE Trans. Instrum. Meas.*, vol. 19, no. 4, pp. 377–382, 1970.

[14] W. B. Weir, "Automatic measurement of complex dielectric constant and permeability at microwave frequencies," *Proc. IEEE*, vol. 62, no. 1, pp. 33–36, 1974.

[15] J. L. Snoek, "Dispersion and absorption in magnetic ferrites at frequencies above one Mc/s," *Physica*, vol. 14, no. 4, pp. 207–217, 1948.

[16] W. Li et al., "Enhanced thermal stability of carbonyl iron nanocrystalline microwave absorbents," *Nanomaterials*, vol. 14, no. 10, p. 869, 2024.

[17] L. D. Landau and E. M. Lifshitz, "On the theory of the dispersion of magnetic permeability in ferromagnetic bodies," *Phys. Z. Sowjetunion*, vol. 8, pp. 153–169, 1935.

[18] R. Walser et al., "Shape-optimized ferromagnetic particles with maximum theoretical microwave susceptibility," *IEEE Trans. Magn.*, vol. 34, no. 4, pp. 1390–1392, 1998.

[19] S. Yang et al., "Effect of ball-milling process on microwave absorption behaviors of flaky carbonyl iron powders," *Materials*, vol. 16, no. 12, p. 4397, 2023.

[20] J. He et al., "Internal strain dependence of complex permeability of ball milled carbonyl iron powders in 2–18 GHz," *J. Appl. Phys.*, vol. 111, no. 9, 2012.

[21] T. Rudeichuk et al., "Exploring the impact of different milling parameters of Fe/SiO_2 composites on their structural and magnetic properties," *Materials*, vol. 17, no. 4, p. 862, 2024.

[22] C. Liang et al., "Structural design strategies of polymer matrix composites for electromagnetic interference shielding: A review," *Nano-Micro Lett.*, vol. 13, no. 1, 2021.

[23] ECSS-E-ST-20-07C Rev.2, *Space Engineering Electromagnetic Compatibility*, ESA-ESTEC, European Cooperation for Space Standardization, Noordwijk, NL, Jan. 3, 2022.

[24] B. Zhang et al., "Microwave-absorbing properties of de-aggregated flake-shaped carbonyl-iron particle composites at 2–18 GHz," *IEEE Trans. Magn.*, vol. 42, no. 7, pp. 1778–1781, 2006.

3.

MULTILAYERED ELECTROMAGNETIC ABSORBERS

As this research is conducted within the framework of an industrial Ph.D., the primary objective is to bridge the gap between advanced academic investigation and the stringent integration requirements typical of the aerospace sector [1, 2]. Having defined the fabrication protocols and intrinsic electromagnetic properties of the functionalized coatings in Chapter 2, this chapter shifts the focus from material characterization to structural design and application.

The core challenge addresses the mitigation of electromagnetic interference (EMI) within satellite cavities [1, 3]. Specific emphasis is placed on suppressing reflections within the S-band and the lower C-band, which host critical aerospace systems. To this end, 2.0 GHz and 5.4 GHz were selected as exemplary benchmark frequencies, representative of the operational bands for Telemetry, Tracking, and Command (TT&C) systems and Synthetic Aperture Radar (SAR) antennas [3, 4]. To address these requirements without compromising established aerospace standards, this research leverages the industrial heritage of the project's co-funder, Thales Alenia Space Italia S.p.A. Current thermal control solutions employed by the company rely on qualified thermo-optical coatings, such as the AZ paint investigated in the previous Chapter, designed primarily for passive thermal regulation. While highly effective for thermal stability, the standard, unloaded formulations of the AZ matrix are typically transparent or exhibit negligible absorption in the microwave regime. As the frequency decreases and the wavelength proportionally increases—reaching 15 cm at 2 GHz—this transparency becomes a critical limitation, rendering thin, single-layer coatings electrically invisible [5]. Consequently, the central thesis of this work is to utilize the flight-qualified AZ matrix as a baseline, functionalizing it with electromagnetic fillers to integrate EMI reduction capabilities into a material already optimized for the stringent thermo-optical requirements of the aerospace sector.

To address this requirement without disrupting established manufacturing processes, this work proposes a modular multilayer adhesive structure [6]. Rather than developing a heavy bulk material, the proposed solution involves engineering the filler-loaded aerospace-grade paint into an optimized multilayer configuration. This approach provides a dual advantage. First, it ensures risk mitigation and process continuity by using the same chemical base as the already qualified AZ paint; this means the material theoretically satisfies strict space-environment standards without requiring new, costly qualification campaigns. Concurrently, the architecture provides inherent tunability; by modulating the stratification sequence and layer thickness, the system facilitates frequency-selective absorption, effectively transforming the previously characterized dispersive media into an efficient resonant absorbing structure.

Furthermore, this chapter presents a comparative design analysis between the absorbers realized with the filler-loaded AZ paint and those designed using the aeronautical-grade, water-based paint (AW) introduced in Chapter 2.

Building upon the electromagnetic findings of the previous section—which demonstrated that the organic solvent in AZ paint facilitates superior filler dispersion [7, 8]—this analysis focuses on the resulting enhancements to complex permeability. By preventing particle agglomeration, the organic solvent promotes a more uniform and effective magnetic flux distribution throughout the coating. This heightened permeability, characterized by an increase in both the real component (μ') for magnetic energy storage and the imaginary component (μ'') for dissipative loss, directly translates into improved radar absorbing material (RAM) performance. Ultimately, this enhanced electromagnetic wave attenuation enables the functionalized AZ coating to achieve a reflection loss significantly superior to that of the water-based (AW) paint, validating its effectiveness as a lightweight electromagnetic shielding solution.

Consequently, these improved electromagnetic properties translate directly into a more efficient and versatile absorber design. The coating achieves the necessary impedance matching and attenuation while maintaining a sub-wavelength profile, significantly lower than the theoretical quarter-wavelength ($\lambda/4$) typically required for traditional resonant absorbers.

Beyond its electrical performance, the functionalized AZ coating offers superior integration potential due to its highly tunable nature. Unlike rigid shielding components, this paint-based solution can be easily applied to complex internal satellite geometries, maintaining strong adhesion and mechanical integrity in extreme aerospace environments. This combination of electrically thin profile and ease of application provides a critical advantage for high-density satellite cavities, where spatial constraints are stringent and the integration of EMI mitigation must not interfere with the existing mechanical or thermal layouts.

3.1 Simulations and optimization

The electromagnetic design of the multilayered absorbing structure is based on Transmission Line Theory (TLT), which models the propagation of a plane wave through material layers as signals traveling along a transmission line [5]. According to this theory, the input impedance Z_{in} of a single absorbing layer with thickness d, backed by a load impedance Z_{load}, is calculated as follows:

$$Z_{in} = Z_0 \frac{Z \tanh(d\gamma) + Z_{load}}{Z_{load} \tanh(d\gamma) + Z} \tag{14}$$

where Z_0 represents the characteristic impedance of free space ($Z_0 \approx 377\ \Omega$). The variables Z and γ denote the intrinsic properties of the material, defined respectively as the characteristic impedance of the medium and the propagation constant:

$$Z = Z_0 \sqrt{\frac{\mu_r}{\varepsilon_r}} \tag{15}$$

$$\gamma = \alpha + j\beta \tag{16}$$

Here, μ_r and ε_r are the complex relative magnetic permeability and electric permittivity of the composite material. α and β represent the attenuation constant and phase constant, respectively. For a lossy material, the propagation constant is frequency-dependent (f) and is expressed as:

$$\gamma = j\frac{2\pi f}{c}\sqrt{\mu_r \varepsilon_r} \tag{17}$$

where c is the speed of light in a vacuum.

In the case of a multilayer structure, the input impedance of the i-th layer acts as the load impedance (Z_{load}) for the preceding layer ($i-1$). The calculation is performed recursively, starting from the layer in contact with the satellite's metal surface (where $Z_{load} = 0$, assuming a PEC backing) [4]. Defining Z_{in1} as the impedance at the interface of the first layer (metal-backed), the equation simplifies to:

$$Z_{in1} = Z_1 \tanh(d_1\gamma_1) \tag{18}$$

For subsequent layers ($i = 2, 3, \dots, n$), the input impedance is derived recursively:

$$Z_{in,i} = Z_i \frac{Z_{in,i-1} + Z_i \tanh(\gamma_i d_i)}{Z_i + Z_{in,i-1} \tanh(\gamma_i d_i)} \tag{19}$$

The total input impedance of the entire stack, viewed from the air interface, is defined as $Z_{in,tot}$. For a structure with n layers, this is the final result of the recursive process:

$$Z_{in,tot} = Z_{in,n} \tag{20}$$

The optimization goal is to minimize the reflection coefficient Γ at the air-material interface, expressed as Reflection Loss (RL) in dB:

$$RL[dB] = 20\log_{10}\left|\frac{Z_{in,tot} - Z_0}{Z_{in,tot} + Z_0}\right| \tag{21}$$

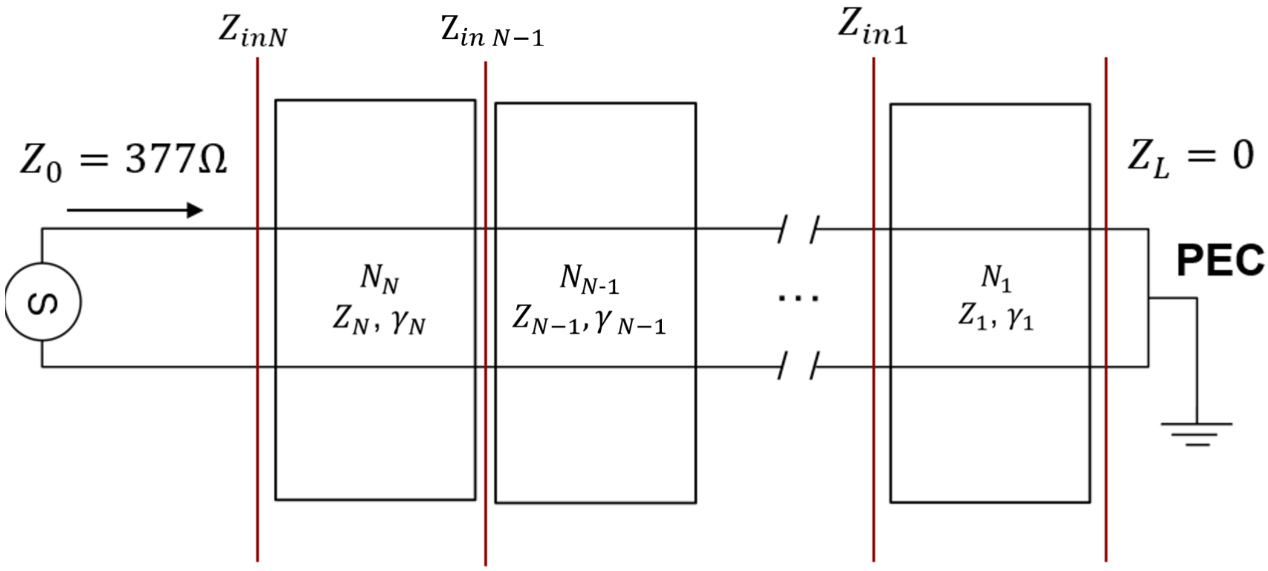

Fig. 3.1 Equivalent circuit diagram of the multilayered absorber modeled as a cascaded transmission line network backed by a PEC short circuit ($Z_L = 0$).

By characterizing the GNP-loaded and CIP-loaded formulations as segments with distinct characteristic impedances (Z_n) and propagation constants (γ_n), the multilayer assembly is reduced to a cascaded network of transmission lines [4, 9]. This allows the MATLAB-based optimization tool to systematically analyze electromagnetic wave propagation through the stratified medium, accounting for the phase-shifts and magnitude attenuations introduced at each material interface through cascaded impedance calculations that track the cumulative electromagnetic response of the entire multilayer structure.

The core objective of this computational framework is to achieve impedance matching between Z_0 and the total input impedance of the stack Z_{in}. By iteratively tuning the thickness and material sequencing, the algorithm minimizes the impedance mismatch that triggers reflections [5]. Furthermore, the PEC-backed boundary condition serves as a terminal short circuit ($Z_L = 0$); this forces a reflection phase shift that directs the energy back through the lossy layers [4, 5].

3.1.1 Optimization Algorithm

The structural design of the multilayer electromagnetic absorber involves a high degree of complexity due to the non-linear interdependence between individual layer thicknesses and the frequency-dependent complex properties of the loaded paints. Because a direct analytical inversion of the recursive impedance-transformation equations presented in the previous section is mathematically intractable—particularly when solving for multiple dispersive layers where the thickness variables are nested within transcendental hyperbolic functions—a dedicated computational tool was developed in MATLAB to identify the optimal geometric configuration [6, 10].

The algorithmic logic follows a constrained optimization workflow specifically engineered to respect aerospace manufacturing tolerances and practical assembly protocols. A central feature of this model is the definition of a repeating unit cell, composed of a GNP-loaded lossy dielectric layer, a CIP-loaded magnetic layer, and a fixed $150\ \mu\text{m}$ adhesive dielectric substrate. The optimization seeks to determine the ideal dimensions of this multilayer unit and the optimal number of repetitions (N), reflecting a modular assembly strategy. This approach is designed to facilitate manual integration: once the functional bilayer is fabricated onto the adhesive carrier, the total required thickness is achieved by stacking these discrete modules one on top of the other until the design target is met. This modularity not only simplifies the fabrication process and ensures the structure remains mechanically robust and reparable, but also allows for the precise tuning of the operating absorption frequencies by simply adjusting the stack count or layer dimensions to meet specific mission requirements.

To ensure the model remains grounded in physical reality, the search space for the thickness of the CIP-loaded paint (t_{CIP}) and the GNP-loaded paint (t_{GNP}) is strictly bounded between $70 - 180\ \mu\text{m}$ and $70 - 150\ \mu\text{m}$, respectively. These limits are defined by the manufacturer's technical specifications for the AZ matrix and represent the qualified thickness windows for a single-pass spray application. By constraining the optimization to these constraints, the algorithm ensures that the resulting unit cell can be realistically manufactured and manually handled during the stacking phase without compromising mechanical adhesion or surface uniformity. Furthermore, staying within these limits prevents common manufacturing defects such as solvent entrapment or micro-cracking during the curing phase.

A primary objective of this tool is to perform a comparative design analysis between the AW and AZ formulations. The algorithm independently optimizes the stacking for both paints to observe how the increase in complex permeability, afforded by superior filler dispersion in the AZ organic solvent, influences radar-absorbing performance. The process begins with a global stochastic search using a Monte Carlo approach (10,000 trials) to explore the vast solution space and avoid local minima caused by complex phase interference. For every sampled thickness pair, the algorithm evaluates two potential stacking sequences—standard GNP-CIP-Substrate (GCS) and inverted CIP-GNP-Substrate (CGS)—to identify the optimal internal impedance distribution within the unit cell, maximizing the transition of energy between the lossy layers.

Once the stochastic search identifies the most promising region, the Nelder-Mead simplex algorithm (fminsearch) is employed for local refinement, allowing for sub-micron tuning of the unit cell layers [11]. This gradient-free method is particularly effective here, as it can handle the small numerical discontinuities inherent in experimental material datasets. The performance is governed by the recursive impedance-transformation routine, which evaluates the total reflection loss for each manual stack repetition. To ensure high absorption, an exponential penalty term aggressively increases the cost if the reflection loss rises above a −15 dB threshold at the 2.0 GHz and 5.4 GHz targets. To further isolate the impact of magnetic enhancement, the final output compares the optimized AZ response against three control models: a non-magnetic variant ($\mu = 1$), an inverted order, and a 'GGS' dielectric configuration, where the magnetic layer becomes with equal parameters as the lossy dielectric one. This yields the optimized layer count and total physical thickness, facilitating a direct comparison of how the enhanced complex permeability of the AZ system translates into a more compact, electrically thin structural design [7, 8].

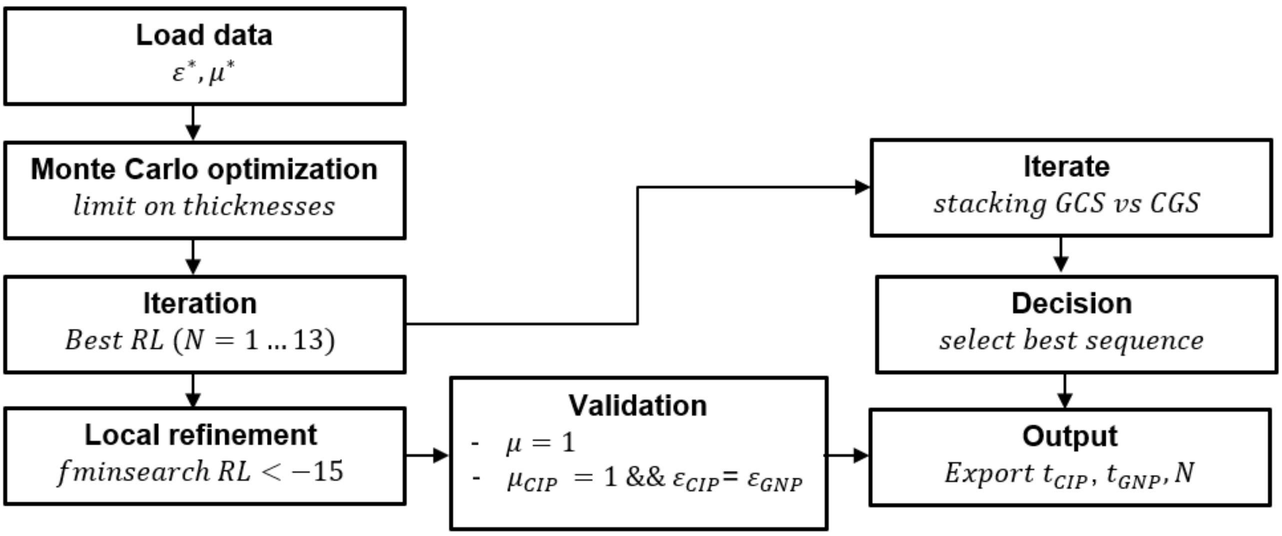

Fig. 3.2 Schematic workflow of the MATLAB optimization algorithm: global stochastic search followed by local Nelder–Mead refinement, evaluated against dual frequency targets at 2.0 and 5.4 GHz.

3.1.2 Electromagnetic Absorption of the Water-Based (AW) Configuration

To establish a baseline and evaluate the impact of the binder matrix on overall absorption performance, a full optimization was first conducted using the water-based AW paint. The unit cell for this configuration consists of a 180.0 μm CIP layer, a 150.0 μm GNP layer, and a 150.0 μm adhesive substrate. As established in Chapter 2, the AW matrix exhibits inherently lower magnetic permeability compared to solvent-based alternatives at equivalent filler concentrations [7, 8].

At the 2.0 GHz target, the optimized magnetic stack (GCS) requires $N = 13$ repetitions (total thickness of 6.24 mm) but achieves a RL of only -6.40 dB. This poor low-frequency performance is fundamentally tied to a severe impedance mismatch [5]. The complex input impedance (Z_{in}) at this frequency is $202.29 + j245.34\,\Omega$. The high reactive component and low resistive component prevent efficient wave penetration [4, 12]. Evaluating alternative configurations confirms these material limitations. For instance, using an inverted stacking order (CGS) yields an RL of -4.69 dB, while the non-magnetic case ($\mu_r = 1$) degrades entirely to -1.56 dB. Even a purely conductive configuration only reaches -8.37 dB, which outperforms the optimized stack but still fails to meet standard absorption thresholds [5, 12].

Conversely, at the 5.4 GHz target, the GCS AW configuration performs significantly better. The structure is optimized with $N = 6$ repetitions (total thickness of 2.88 mm), yielding a deep RL notch of -21.12 dB. The input impedance here is much closer to free space, at $395.46 - j65.47\,\Omega$. Alternative arrangements validate the necessity of the optimized CGS sequence, with the inverted stack achieving -13.73 dB, the $\mu_r = 1$ case ($N = 7$) dropping to -9.19 dB, and the lossy dielectric case ($N = 5$) yielding -6.34 dB. Ultimately, the AW matrix clearly struggles to provide dual-band stability, acting effectively only at higher frequencies [8, 12]. All these results are presented in Fig. 3.3.

The modularity of the design and the influence of total thickness are evidenced by the evolution of RL as the number of repetitions (N) increases. As layers are added—transitioning from a single unit cell to the maximum stack of N = 13—the increasing physical thickness causes the resonance peaks to shift predictably from higher to lower frequencies as shown in Fig. 3.4[4, 9]. This behavior is a direct result of the targeted optimization strategy focused on the 2.0 GHz and 5.4 GHz bands. While the structure demonstrates deep absorption notches at higher frequencies for lower values of N, the shift toward the 2.0 GHz range shows a broadening of the response. This does not indicate a material failure, but rather the mathematical limit of the current stack; with the total thickness capped at 13 repetitions, the system reaches its optimal phase-matching configuration for the primary design targets. The bundle of curves confirms that the geometric phase-matching principles are functioning as intended [4, 5]. The "bias" seen in the graph is simply the result of the MATLAB algorithm prioritizing the convergence of these specific frequency points within the defined structural constraints ($N \leq 13$), rather than an inherent inability of the water-based binder to dissipate energy at lower frequencies [11].

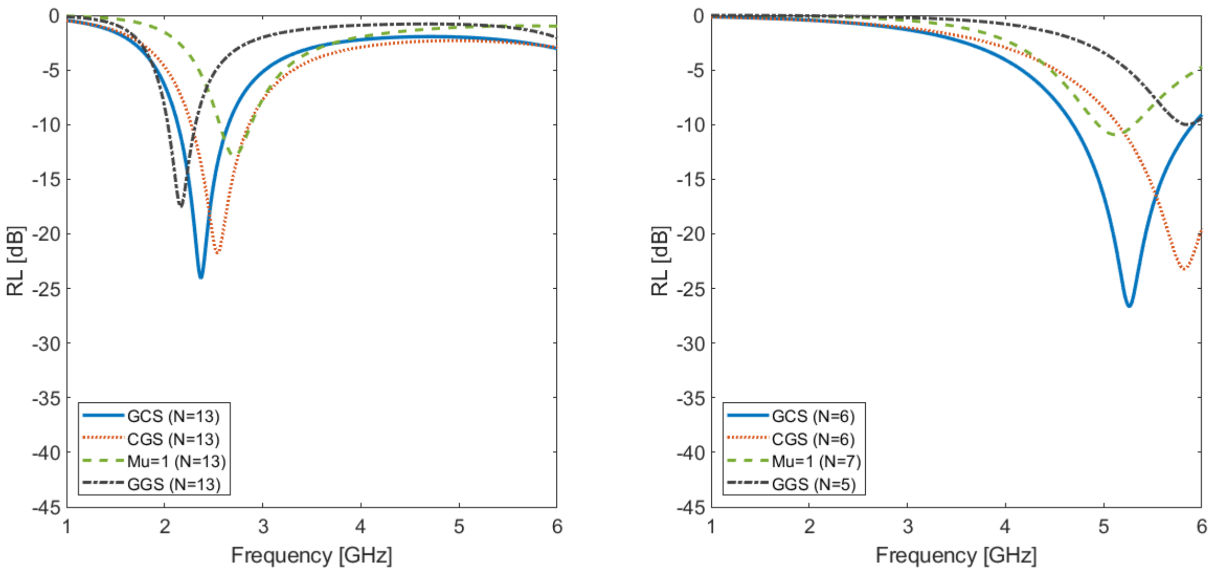

Fig. 3.3 RL spectra of the AW multilayer configuration at both target frequencies, comparison of stacking orders, non-magnetic and fully dielectric cases.

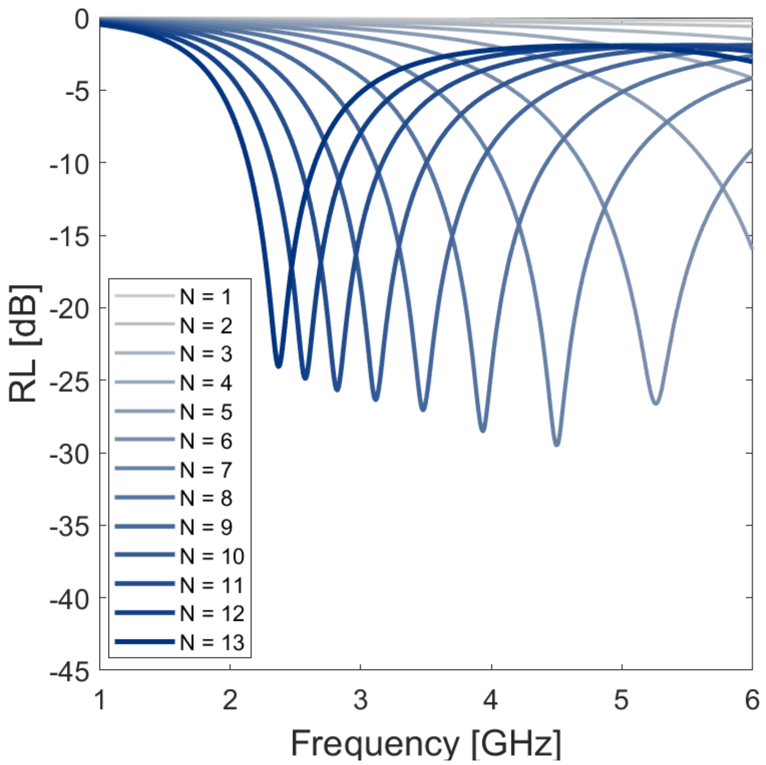

Fig. 3.4 Evolution of RL spectra with increasing number of unit cell repetitions N for the AW configuration, illustrating the progressive migration of absorption resonances toward lower frequencies with increasing total thickness.

3.1.3 Electromagnetic Absorption of the Solvent-Based (AZ) Configuration

Following the AW analysis, the solvent-based AZ configuration demonstrates the critical influence of material combination and optimized matrix properties on electromagnetic absorption [7, 8].

At the 2.0 GHz target, the optimized AZ magnetic stack (GCS) utilizing $N = 13$ repetitions (total thickness of 6.21 mm) achieves an excellent RL of -20.11 dB. This performance is closely tied to the complex input impedance, which at this frequency is $381.26 + j75.07\,\Omega$. When normalized to the impedance of free space (η_0), this results in a value of $Z_n \approx 1.01 + j0.20$, indicating a near-perfect impedance match that allows for deep energy penetration and subsequent dissipation [4, 5, 12]. The sensitivity of the AZ system is evident when comparing the optimized results to alternative configurations. Using an inverted stacking order (CGS) for the same stack results in an RL of only -12.80 dB, highlighting that the sequence of layers is as vital as their individual properties [6]. This significant performance difference arises from the fundamental electromagnetic principle that the GNP-loaded topcoat provides superior impedance matching at the critical air-absorber interface. The enhanced relative dielectric permittivity of the GNP layer ($\varepsilon' \approx$ 4-6) creates a graduated impedance transition from free space (Z_0 = 377Ω) toward the higher impedance magnetic layer, minimizing interfacial reflections that would otherwise prevent electromagnetic energy from penetrating into the absorber structure. Conversely, when the CIP-loaded layer is positioned externally (CGS configuration), the abrupt impedance discontinuity between air and the magnetic material creates substantial reflections at the surface, reducing the fraction of incident energy that can enter the absorber and be dissipated, thereby degrading the overall absorption performance despite identical material composition and total thickness.

Furthermore, without the permeability of the CIP paint ($\mu_r = 1$), the RL degrades significantly to -1.48 dB. Similarly, the GNP-only configuration (GGS) yields an RL of -7.78 dB, confirming that neither conductive nor magnetic properties alone satisfy the design requirements [13, 14].

At the 5.4 GHz target, the AZ structure is optimized with $N = 4$ repetitions (total thickness of 2.86 mm), yielding an RL of -15.00 dB. The input impedance is $302.23 - j96.55\,\Omega$ ($Z_n \approx 0.80 - j0.26$), representing a balanced trade-off between thickness and absorption depth [4, 5]. While the inverted order at this specific point shows a deeper notch (-23.98 dB), the CGS order was selected through global optimization to ensure stable, high-level performance across both target bands [10, 11]. Again, the $\mu_r = 1$ variant fails ($N = 5$, -9.45 dB), and the GNP-only stack remains insufficient (-6.38 dB) [13].

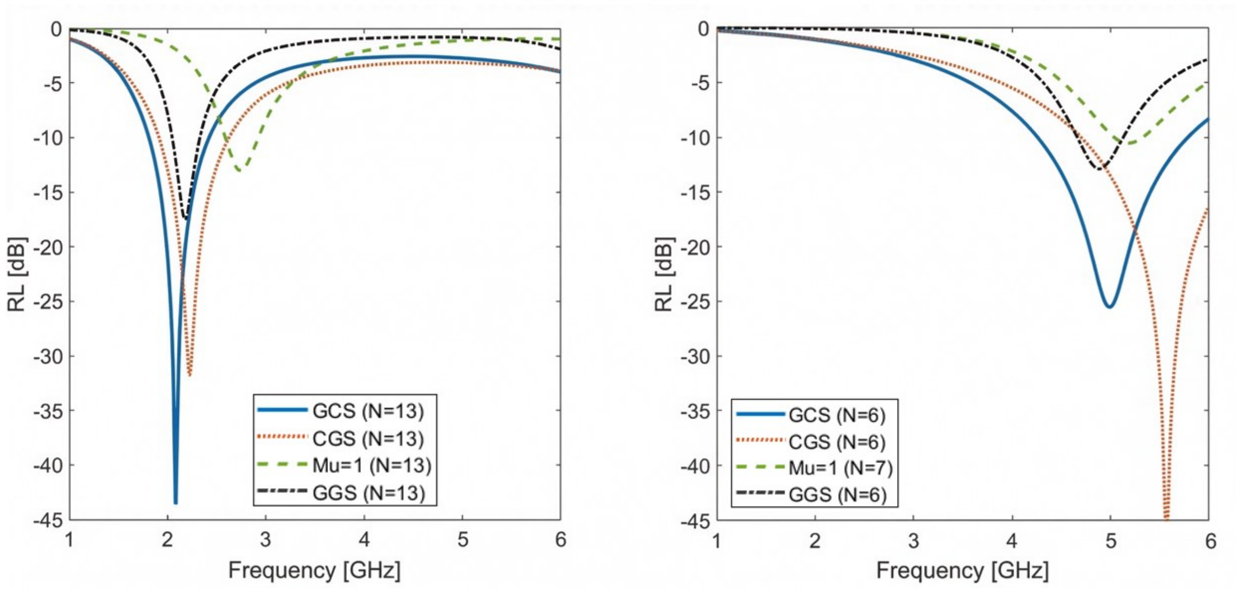

Fig. 3.5 RL spectra of the AZ multilayer configuration at both target frequencies, comparison of stacking orders, non-magnetic and fully dielectric cases.

The highly tunable nature of the AZ configuration becomes apparent when analyzing the RL across varying layer counts, as presented in Fig. 3.6. Electrically thin stacks at low values of N naturally result in minimal absorption, with RL values hovering near 0 dB, as the total thickness remains insufficient to satisfy the quarter-wavelength resonance condition that governs optimal absorption. However, incrementally increasing the number of repetitions produces a systematic pattern where resonance notches predictably migrate toward lower frequencies. This progressive frequency shift is characteristic of multilayer absorbers and demonstrates that each additional layer pair contributes constructively to the overall electromagnetic response without introducing parasitic resonances or impedance mismatches that could degrade performance.

The systematic tuning behavior observed across different layer counts confirms the stability of the effective medium properties throughout the entire volume of the absorber, validating that the individual GNP and CIP layers maintain their intrinsic electromagnetic characteristics regardless of their position within the multilayer stack. This consistency is critical for predictive design, as it ensures that the electromagnetic properties extracted from thin samples can be reliably extrapolated to thicker configurations without the need for extensive re-characterization.

By leveraging this consistent behavior, the primary frequency of operation can be dictated purely by the total physical thickness of the stack, presenting an ideal, customizable approach for complex environments like satellite systems where different subsystems may require electromagnetic absorption at distinct frequency bands [1, 2]. This thickness-based tunability eliminates the need for complex material reformulations or manufacturing process modifications when adapting the absorber design to different frequency requirements, significantly simplifying the qualification and deployment process for aerospace applications where material consistency and predictable performance are paramount for mission-critical electromagnetic compatibility.

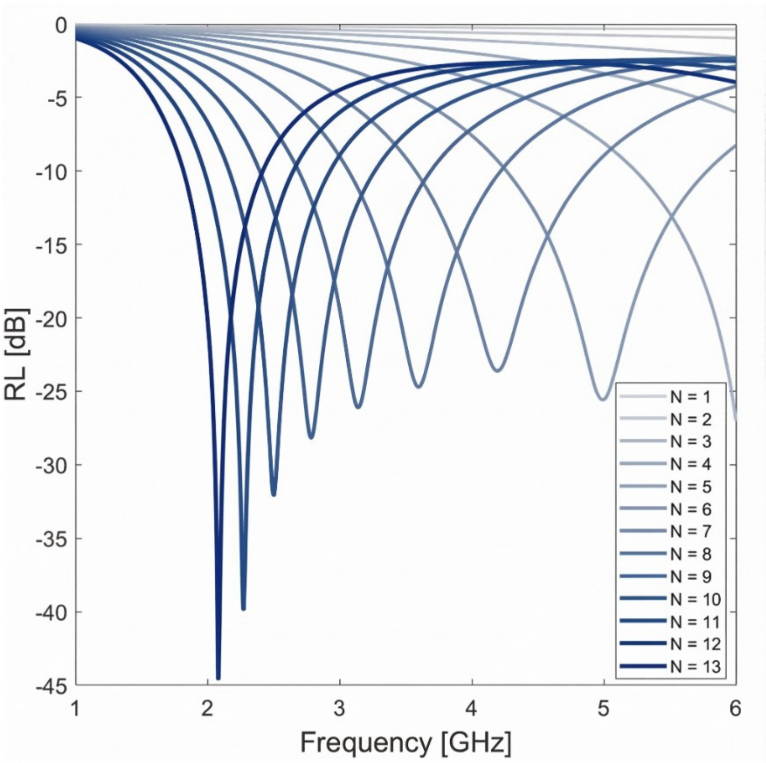

Fig. 3.6 Evolution of RL spectra with increasing number of unit cell repetitions N for the AZ configuration, illustrating the progressive migration of absorption resonances toward lower frequencies with increasing total thickness

3.1.4 Comparative Analysis: Matrix Influence on Radar Absorbing Efficacy

A direct comparison between the water-based (AW) and solvent-based (AZ) configurations conclusively demonstrates the superiority of the AZ matrix for comprehensive EMI absorbance, particularly for dual-band or low-frequency applications [7, 8, 12]. The principal performance differentiator is the magnetic permeability achievable within each binder system, as summarized in Table 3.1 and Table 3.2. At 2.0 GHz, the AW matrix fundamentally fails to provide adequate absorption (RL = −6.40 dB), suffering from a highly reactive impedance mismatch [5]. In stark contrast, the higher magnetic permeability facilitated by the AZ organic solvent system allows the coating to act as an effective impedance matching layer [7, 8], pulling the normalized impedance to $Z_n \approx 1.01 +$

$j0.20$—almost perfectly aligned with the free-space characteristic impedance. This results in a superior RL of −20.11 dB.

While the AW matrix produces a deeper absolute absorption notch at 5.4 GHz (−21.12 dB versus −15.00 dB for AZ), it lacks the broadband stability and dual-band capability of the solvent-based system [12]. The global optimization of the AZ stack ensures reliable, standard-exceeding absorption across both target frequency bands using a single structural philosophy [10, 11]. This confirms the AZ formulation as the optimal choice for the final absorber design, particularly for satellite applications requiring simultaneous coverage of the S-band TT&C frequency and the C-band SAR operational range [1, 2, 3].

Parameter	AW Matrix	AZ Matrix
Target frequency	2.0 GHz	
Optimal stacking order	GCS	GCS
Repetitions N	13	13
Total thickness (mm)	6.24	6.21
Reflection Loss (dB)	−6.40	−20.11

Table 3.1 Comparative summary of optimized multilayer performance for AW and AZ matrix configurations at 2.0 GHz target frequency.

Parameter	**AW Matrix**	**AZ Matrix**
Target frequency	5.4 GHz	
Optimal stacking order	CGS	CGS
Repetitions N	6	6
Total thickness (mm)	2.88	2.86
Reflection Loss (dB)	−21.12	−15.00

Table 3.2 Comparative summary of optimized multilayer performance for AW and AZ matrix configurations at 5.4 GHz target frequency.

3.2 Realization

The fabrication with the two distinct polymer matrices, AW and AZ, was then carried out. The electromagnetic properties of the CIP-loaded magnetic paints, previously characterized and described in Chapter 2, acted as the foundational data for these formulations. A high-loading concentration of 70 wt% CIP was selected for the magnetic layers. In order to isolate the influence of the host matrix on the magnetic response of the composite, the dielectric contribution was kept constant across both formulations: the GNP loading was tuned such that both the AW and AZ-based dielectric layers exhibit equivalent permittivity trends and values — 3 wt% for the AZ case and the corresponding amount for the AW matrix [14]. This approach ensures that any observed difference in the overall electromagnetic performance between the two systems can be directly attributed to the effect of the binder environment on the effective relative permeability of the CIP-loaded layer, rather than to variations in the dielectric response.

The realization of the modular multilayer structure followed a precise and iterative deposition sequence. First, the 70wt% CIP-loaded paint was deposited onto an adhesive substrate to form the base. To ensure the precise layer thicknesses required by the simulations, a combined air-spraying and plotting method was employed. This controlled process was critical for achieving a high degree of homogeneity across the planar surface and minimizing surface roughness that could lead to scattering losses. Once the CIP base layer was stabilized, the GNP-loaded paint was prepared at the simulated concentration and deposited directly onto the CIP coating using the same air-spraying technique. Finally, the samples underwent a curing cycle compliant with the established chemical baseline to ensure that the structural integrity and outgassing profiles remained within the limits required for space qualification.

To transition from a planar coating to a testable microwave component, a modular stacking approach was used. The composite films were precision-cut into annular samples matching the dimensions of a standard coaxial airline with a 7 mm external diameter and a 3.04 mm internal diameter. The individual functionalized layers were then stacked to achieve the final adhesive structure. A primary challenge in this phase was the elimination of air gaps between layers, as even microscopic gaps can cause significant impedance mismatches and disrupt the destructive interference patterns required for absorption. This risk was mitigated by the inherent tackiness of the adhesive substrate and the application of controlled mechanical pressure during the stacking sequence.

3.3 Experimental validations and Measurement Setup

The analytical characterization of a fabricated multilayered electromagnetic absorber marks a critical transition from a discrete, stratified geometry to a homogenized equivalent medium representation [15]. By treating the heterogeneous multilayer assembly as a single equivalent layer of identical total thickness, the complex interactions between individual magnetic and dielectric laminae are condensed into bulk macroscopic parameters through the definition of an effective complex relative permittivity (ε_{eff}) and permeability (μ_{eff}). This transformation provides a mathematically rigorous yet computationally tractable description of the periodic structure, and is essential for high-fidelity integration into large-scale numerical models where explicit layer-by-layer modeling would be prohibitive [6, 15].

The effective parameters are extracted from coaxial airline measurements using the NRW algorithm [16, 17], applied here to the multilayer stack as a unified entity rather than to its individual constituent layers as in Chapter 2. The resulting frequency-dependent profiles reveal the dispersive nature of the composite across the 1–6 GHz range and are shown in Fig. 3.7. The real part of the relative, ε'_{eff}, remains consistently elevated, initiating near 21 and gradually stabilizing toward 18.5, while the dielectric loss factor, ε''_{eff}, undergoes a more pronounced reduction from approximately 4 to 1. Simultaneously, the magnetic response exhibits a clear relaxation: the real component μ'_{eff}decreases from 1.7 to approximately 1.25, while the imaginary component μ''_{eff}displays an upward trend peaking near 0.42 at approximately 4.5 GHz. This behaviour underscores a frequency-dependent dissipation mechanism in which dielectric losses dominate at lower frequencies and magnetic losses become increasingly prominent through the mid-to-upper C-band [8, 12].

Having established the effective electromagnetic parameters through experimental extraction, the next critical step involves validating the accuracy of these parameters and the reliability of the homogenization approach through numerical modeling and cross-correlation with independent experimental measurements. To demonstrate this validation methodology, a comparative study was conducted using the water-based AW system. The manufactured multilayer sample, consisting of an alternating AW stack of N = 5 repetitions, was inserted into the airline fixture and measured in a through-transmission configuration. The coaxial airline supports TEM mode propagation, which is physically equivalent to plane wave incidence in free space [19, 20], making it an ideal environment for probing the intrinsic electromagnetic response of the stacked layers. As illustrated in Fig. 3.8, the validation framework encompasses the physical laboratory sample, its corresponding full-wave 3D model developed in CST Microwave Studio, and a cross-sectional representation of the stack within the airline.

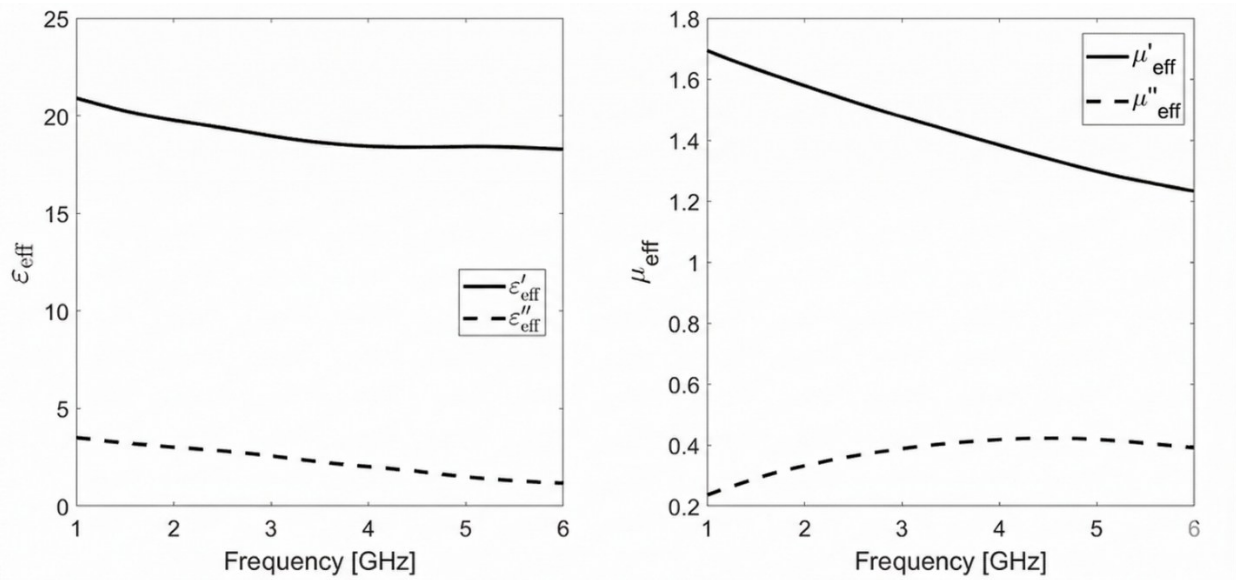

Fig. 3.7 Frequency-dependent effective complex relative permittivity and permeability of the AW multilayer stack modeled as a homogenized single-layer effective equivalent across the 1–6 GHz range.

The three approaches — experimental VNA measurement, full-wave TEM simulation in CST, and the analytical single-layer effective medium model — are compared directly through the magnitude and phase of the S-parameters across the measured frequency range [16, 17, 18], as presented in Fig. 3.9. In both representations, the three curves exhibit strong mutual agreement throughout the band of interest. The magnitude responses align closely in both amplitude and spectral shape, while the phase curves track one another with consistent fidelity, confirming the absence of any significant systematic discrepancy between the three approaches. This coherence is particularly significant for the effective medium representation: despite reducing the full geometric complexity of the N = 5 multilayer stack to a single homogeneous equivalent layer, the analytical model faithfully reproduces both the measured and simulated behaviour, confirming that it is not merely a convenient simplification but a physically sound description of the stack's aggregate electromagnetic response [15].

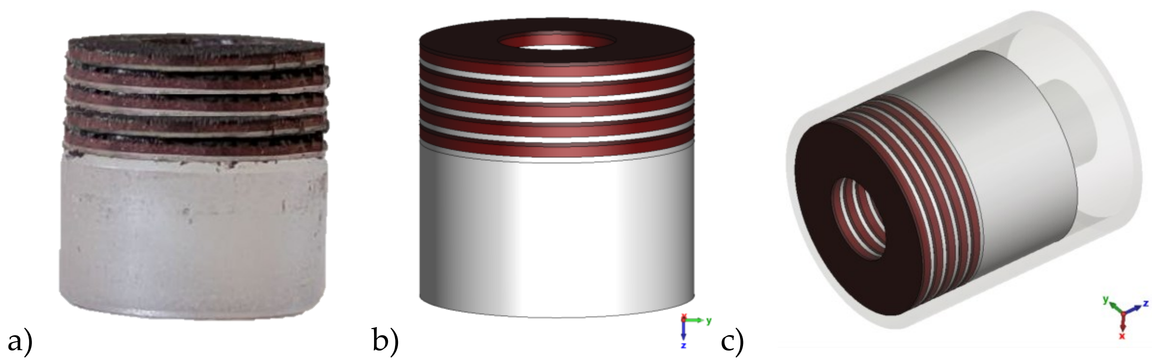

Fig. 3.8 Triple-correlation validation framework: (a) physical laboratory sample (N = 5, AW) inserted in the coaxial airline; (b) corresponding full-wave 3D CST model; (c) cross-sectional schematic of the stacked sample within the coaxial fixture.

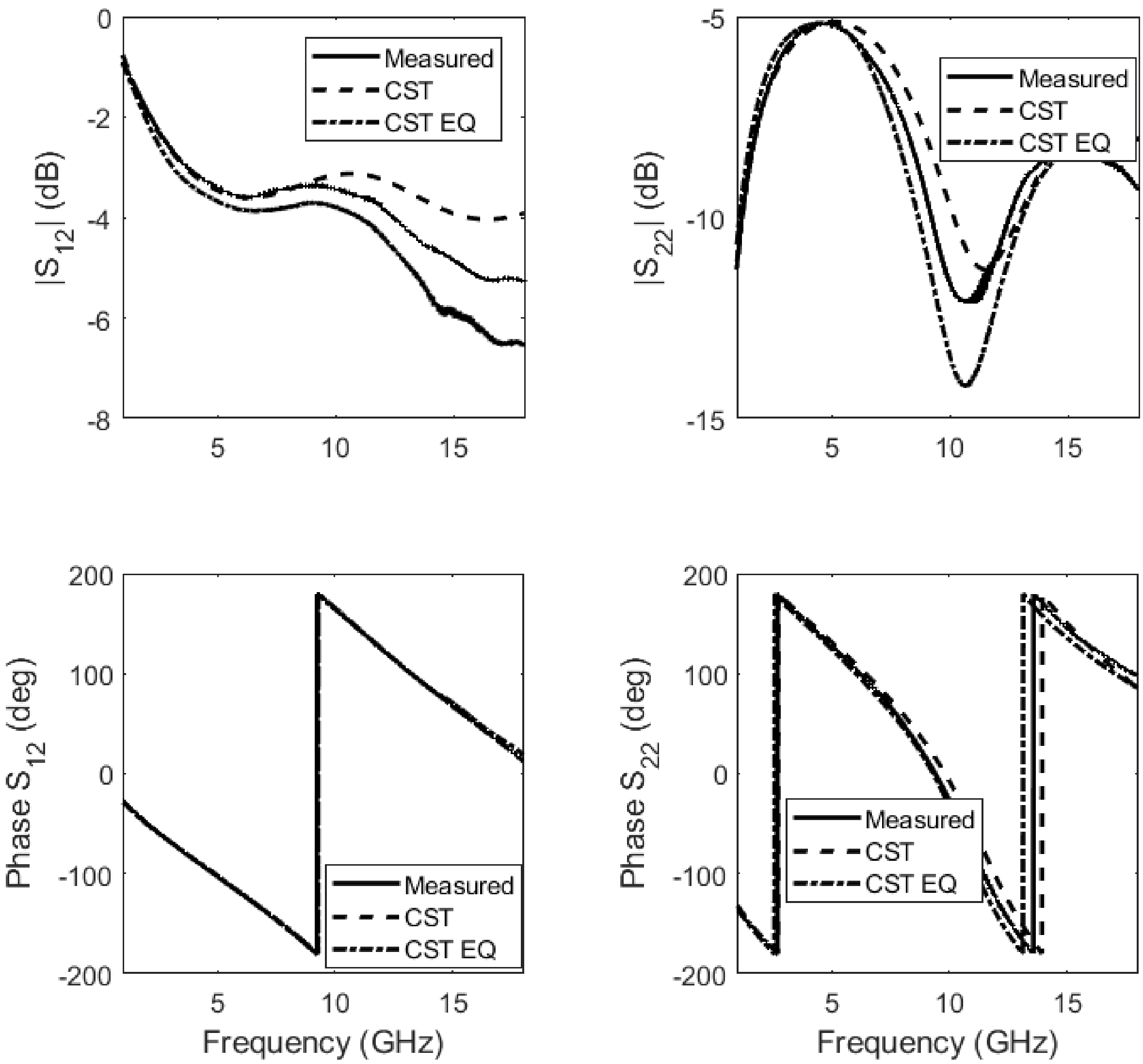

Fig. 3.9 Comparison of experimentally measured S-parameters (S_{11} and S_{21}) of the N = 5 AW multilayer stack against 3D CST full-wave simulations and the analytical effective single-layer model across the 1–6 GHz range.

The strong agreement across these three distinct domains establishes a rigorous triple correlation among experiment, full-wave simulation, and analytical prediction [15, 16, 17, 18]. Since the electromagnetic interaction between the material and the TEM wave is simultaneously verified through all three approaches in an environment that accurately replicates free-space propagation, the effective material model is considered fully validated. This baseline directly underpins the reliability of the subsequent PEC-backed simulations: the introduction of a metallic boundary condition simply imposes a known short-circuit termination on a material stack whose intrinsic electromagnetic behaviour has already been thoroughly characterized [4, 5]. Furthermore, from an engineering perspective, this single-layer equivalence is indispensable for simulating large-scale systems such as complete satellite assemblies, where explicitly resolving dozens of ultra-thin individual layers would require an extremely dense computational mesh and prohibitive memory costs [6, 15, 21]. Substituting the detailed multilayer stack with a single homogenized equivalent drastically reduces computational overhead, enabling rapid design iterations and full-system electromagnetic compatibility analyses without sacrificing physical accuracy [21].

3.4 EM 3D-full wave simulations in satellite cavity

The transition from laboratory-scale validation to application-level assessment was realized by integrating the homogenized effective medium model into a 3D full-wave time-domain simulation of a realistic, modular small satellite cavity using CST Microwave Studio Suite [21]. This stage represents the technical culmination of the design workflow, providing a high-fidelity prediction of the multilayer's radar absorbing performance within an operationally representative environment. The simulation geometry replicates a multi-tier stack-of-trays satellite architecture, characteristic of modern modular small-satellite designs, where the internal module houses sensitive victim units. Aside from the specific material properties and layer thicknesses, this conducted simulation is analogous in every parameter to the reference configuration presented in Section 2.2.2.4, same solver, same mesh criterion, same NFS excitation level and frequency.

To ensure computational efficiency without sacrificing physical accuracy, the internal walls of the targeted tray within the satellite stack were uniformly coated with the AZ multilayer absorber optimized in Section 3.1.3. This coating was modeled using the previously extracted effective complex parameters [15, 16, 17], thereby bypassing the prohibitive computational overhead of explicit layer-by-layer meshing while maintaining the material's full dispersive signature. The integration of the multilayer absorber into the numerical environment yielded a quantifiable and spatially distributed reduction in electric field (E-field) intensity throughout the satellite cavity. Comparative E-field maps, shown in Fig. 3.10 and 3.11, demonstrate a systematic suppression of peak field values and a significant dampening of the resonant standing wave patterns typically induced by the enclosed metallic cavity. The uncoated reference configuration (Fig. 10a and 11a) exhibits characteristic cavity resonance phenomena with pronounced E-field hot spots concentrated at specific geometric locations within the satellite structure. These high-intensity regions, appearing as bright red concentrations in the field maps, represent areas where electromagnetic energy accumulates due to constructive interference between incident and reflected waves at the metallic boundaries.

The most striking observation from the coated configuration (Fig. 10b and 11b) is the homogenization of the E-field distribution throughout the cavity volume. The multilayer absorber effectively eliminates the sharp field gradients and localized intensity peaks that dominate the uncoated case, replacing them with a more uniform, significantly attenuated field pattern. This transformation is particularly evident in the xy-plane cross-section (Fig. 3.10), where the complex standing wave structure visible in the reference case is substantially smoothed in the absorber-lined cavity.

Furthermore, the zy-plane analysis (Fig. 3.11) reveals that the absorber's effectiveness extends beyond simple amplitude reduction to include a fundamental alteration of the cavity's modal structure. The coherent wave patterns and interference fringes characteristic of cavity resonances are disrupted, indicating that the multilayer coating not only absorbs incident electromagnetic energy but also prevents the establishment of stable standing wave modes within the enclosed volume. This dual mechanism—absorption and modal disruption—is critical for achieving reliable EMI mitigation in complex satellite geometries where multiple resonant modes can couple and interact.

Quantitatively, as summarized in Table 3.3, the application of the 6.2 mm AZ-ML absorber achieved a substantial global reduction in field intensity compared to the 99.63 dBμV/m vacuum reference. Specifically, the Mean E-field measured at the surface of the victim units was reduced to 81.84 dBμV/m, representing a localized attenuation (*delta*) of 17.79 dB. Furthermore, the attenuation metrics for the entire satellite cavity (S/C Mean Attenuation) and the individual tray assembly (Tray Mean Attenuation) were recorded at 14.21 dB and 15.62 dB, respectively, confirming the high-level electromagnetic isolation provided by the conformal coating.

The spatial consistency of the attenuation performance across different measurement zones—from localized victim unit surfaces to the broader cavity and tray assemblies—demonstrates the absorber's ability to maintain effectiveness across varying geometric scales and boundary conditions. This uniformity is particularly significant for satellite applications, where electronic components of different sizes and sensitivities must coexist within the same electromagnetic environment.

These results confirm that the multilayer AZ configuration, modeled through an effective medium approach, effectively disrupts internal cavity resonances and provides critical electromagnetic isolation for sensitive onboard components. The observed performance validates the end-to-end design methodology, proving that engineered lossy coatings can successfully mitigate internal crosstalk and electromagnetic overcrowding in densely packed, high-frequency aerospace architectures. This localized performance is complemented by a consistent reduction in the cavity-averaged noise floor, remaining fully consistent with the material-level performance predicted by the 1D optimization. This alignment validates the transition from raw material characterization to a full-system electromagnetic compatibility assessment that addresses the strict volumetric and performance constraints of modern aerospace platforms.

Case	Frequency	Mean E-Field on the Victim Unit		delta	S/C Mean Attenuation	Tray Mean Attenuation
	[GHz]	[V/m]	**[dBuVrms/m]**	**[dB]**	**[dB]**	**[dB]**
Vacuum	2.00	0.137	99.63	0.00	0	0
6.2 mm AZ ML		0.018	81.84	17.79	14.21	15.62

Table 3.3 Summary of E-field attenuation achieved by applying the optimized multilayer (ML) absorber to the internal satellite cavity walls @2GHz.

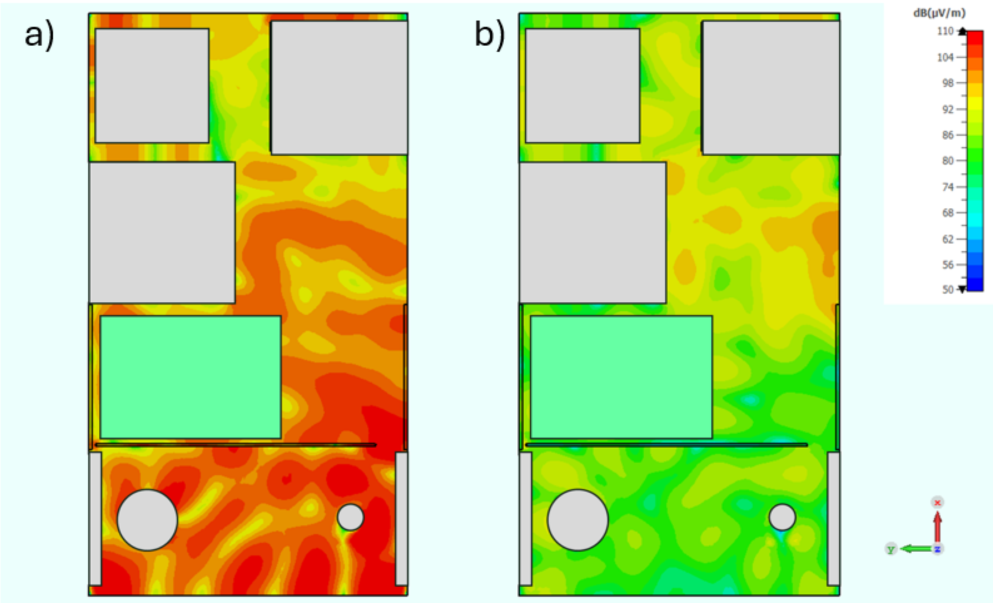

Fig. 3.10 E-field distribution maps inside the modular satellite cavity @2.0 GHz in the xy plane, at the center of the cavity: (a) reference configuration without absorber; (b) cavity walls lined with the AZ multilayer absorber modeled via the effective single-layer equivalent.

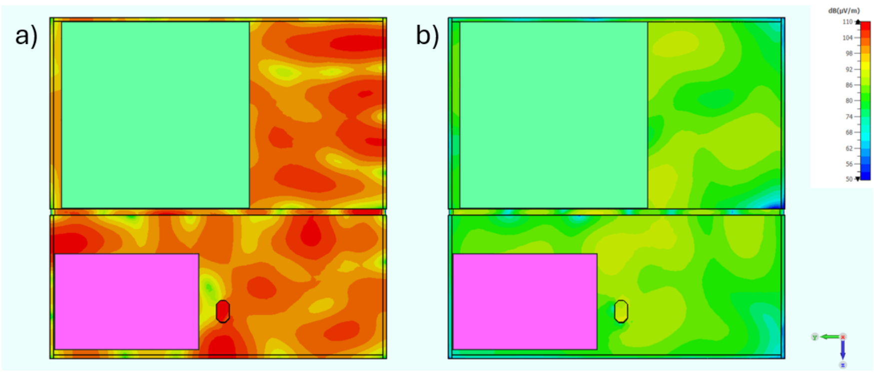

Fig. 3.101 Electric field distribution maps inside the modular satellite cavity @2.0 GHz in the zy plane placed at the center of the victim unit: (a) reference configuration without absorber; (b) cavity walls lined with the AZ multilayer absorber modeled via the effective single-layer equivalent.

3.5 Conclusions

The research presented in this chapter has realized the optimization, fabrication, and subsequent characterization and validation of a multilayered absorber designed as a practical, ready-to-integrate solution for the satellite industry. This development was driven by the need for a system capable of transitioning from laboratory performance to a real-world satellite scenario. Specifically, the deployment of an aerospace-grade paint formulation facilitates the actual integration of the material onto flight hardware, while the adhesive nature of the realized multilayer stack enables a high degree of modulability. This allows the dual-band solution for the S-band (2.0 GHz) and C-band (5.4 GHz) to be treated as a flexible, conformal component that can be adapted to the evolving configurations of modern modular satellite architectures.

The structural design was grounded in Transmission Line Theory [4] and implemented through a hybrid MATLAB optimization algorithm combining a global Monte Carlo stochastic search with local Nelder-Mead refinement [11]. This approach systematically explored the space of layer thicknesses and stacking sequences to identify configurations yielding optimal impedance matching at both target frequencies simultaneously.

The comparative analysis of the water-based (AW) and solvent-based (AZ) formulations highlighted the crucial role of the binder environment. Specifically, the choice of binder favorably alters the complex electromagnetic parameters, directly improving macroscopic absorption. The AW configuration, despite reaching its maximum allowed stack of N = 13 repetitions (6.24 mm), achieves only −6.40 dB at 2.0 GHz due to a severely reactive impedance mismatch. In contrast, the AZ configuration attains −20.11 dB at the same frequency with just N = 13 repetitions (6.21 mm), enabled by a near-perfect normalized impedance of $Z_n \approx 1.01 + j0.20$ — a direct consequence of the superior filler dispersion afforded by the organic solvent environment. At 5.4 GHz the performance gap narrows, with the AW system reaching −21.12 dB and the AZ system yielding −15.00 dB, but the AZ configuration's global optimization ensures reliable dual-band coverage within comparable total thicknesses, establishing it as the preferred candidate for aerospace applications requiring simultaneous S- and C-band attenuation [7, 8, 12]. Sensitivity analyses across both matrices consistently confirmed that the GCS stacking order and the magnetic contribution of the CIP layer are indispensable: inverting the stack or removing the permeability enhancement universally degraded absorption to inadequate levels [5, 13, 14].

The fabricated samples were physically realized through a controlled air-spraying and plotting deposition sequence, precision-cut to the geometry of a standard 7 mm coaxial airline fixture. The homogenization of the multilayer stack into a single effective medium — characterized by frequency-dependent ε_{eff} and μ_{eff} parameters extracted via the NRW algorithm — was rigorously validated through a triple correlation framework encompassing experimental VNA measurements, full-wave CST simulations under TEM excitation, and the analytical single-layer equivalent model. The strong mutual agreement in both S-parameter magnitude and phase across all three approaches confirmed that the effective medium description is not a simplifying assumption but a physically accurate representation of the stack's aggregate electromagnetic behaviour. This validation is foundational: it simultaneously certifies the accuracy of the CST model and the suitability of the homogenized representation for deployment in large-scale computational environments.

Finally, the integration of the validated AZ effective medium model into a 3D full-wave simulation of a realistic modular small-satellite cavity demonstrated the practical impact of the proposed solution. Under sources excitation in S-band frequency range in compliance with radiated E-field limit reported in ECSS-E-ST-20-07C Rev. 2, the multilayer coating produced a spatially distributed suppression of cavity field intensity, with a localized E-field attenuation of up to 17.79 dB at the surface of the victim units. This result confirms that the material-level performance predicted by the 1D optimization translates directly and consistently to system-level EMI attenuation within an operationally representative environment. Collectively, the findings of this chapter validate the end-to-end design methodology — from raw material characterization and numerical optimization through physical fabrication and full-system electromagnetic assessment — establishing the AZ-based multilayer absorber as a viable, weight-efficient, and process-compatible solution for EMI mitigation in modern aerospace platforms.

References

[[1] K. Yang et al., "Bio-inspired multifunctional high-performance electromagnetic shielding coatings resistant to extreme space environments," *The Innovation Materials*, vol. 1, no. 1, p. 100010, 2023.

[2] M. Jaroszewski et al., *Advanced Materials for Electromagnetic Shielding: Fundamentals, Properties, and Applications*. Hoboken, NJ: Wiley, 2019.

[3] European Cooperation for Space Standardization (ECSS), "Electromagnetic compatibility," ECSS-E-ST-20-07C Rev. 2, Noordwijk, The Netherlands, 2012.

[4] A. Braun, "SAR-based landcover classification with Sentinel-1 GRD products," SkyWatch Space Applications Inc. & ESA STEP, 2020.

[5] W. Chew, *Waves and Fields in Inhomogeneous Media*. New York, NY: IEEE Press, 1999.

[6] C. Vong et al., "Manufacturing of a magnetic composite flexible filament and optimization of a 3D printed wideband electromagnetic multilayer absorber in X-Ku frequency bands," *Materials*, vol. 15, no. 9, p. 3320, 2022.

[7] W. Przybył et al., "Microwave absorption properties of carbonyl iron-based paint coatings for military applications," *Defence Technol.*, vol. 22, pp. 1–9, 2023.

[8] K. Sista et al., "Carbonyl iron powders as absorption material for microwave interference shielding: A review," *J. Alloys Compd.*, vol. 853, p. 157251, 2021.

[9] E. Michielssen et al., "Design of lightweight, broad-band microwave absorbers using genetic algorithms," *IEEE Trans. Microw. Theory Tech.*, vol. 41, no. 6, pp. 1024–1031, 2002.

[10] M. Asi et al., "Design of multilayer microwave broadband absorbers using central force optimization," *Prog. Electromagn. Res. B*, vol. 26, pp. 101–113, 2010.

[11] J. Nelder and R. Mead, "A simplex method for function minimization," *Comput. J.*, vol. 7, no. 4, pp. 308–313, 1965.

[12] F. Wang et al., "Microwave absorption properties of carbon black–carbonyl iron/polylactic acid composite filament for fused deposition modeling," *Materials*, vol. 15, no. 15, p. 5455, 2022.

[13] N. Abdelal et al., "Electromagnetic interference shielding and dielectric properties of graphene nanoplatelets/epoxy composites in the x-band frequency range," *J. Mater. Sci.*, vol. 57, pp. 13928–13944, 2022.

[14] A. Rinaldi et al., "Graphene-coated honeycomb for broadband lightweight absorbers," *IEEE Trans. Electromagn. Compat.*, vol. 60, no. 5, pp. 1454–1462, 2017.

[15] A. Sihvola, *Electromagnetic Mixing Formulas and Applications*. London: IEE Publishing, 1999.

[16] A. Nicolson et al., "Measurement of the intrinsic properties of materials by time-domain techniques," *IEEE Trans. Instrum. Meas.*, vol. IM-19, no. 4, pp. 377–382, 1970.

[17] W. Weir, "Automatic measurement of complex dielectric constant and permeability at microwave frequencies," *Proc. IEEE*, vol. 62, no. 1, pp. 33–36, 1974.

[18] O. Luukkonen et al., "A stepwise Nicolson-Ross-Weir based material parameter extraction method," *IEEE Antennas Wireless Propag. Lett.*, vol. 10, pp. 1295–1298, 2011.

[19] J. Baker-Jarvis et al., "Improved technique for determining complex permittivity with the transmission/reflection method," *IEEE Trans. Microw. Theory Tech.*, vol. 38, no. 8, pp. 1096–1103, 1990.

[20] C. Balanis, *Advanced Engineering Electromagnetics*, 2nd ed. Hoboken, NJ: Wiley, 2012.

[21] Dassault Systèmes, "CST Studio Suite — Electromagnetic field simulation software," Vélizy-Villacoublay, France: Dassault Systèmes, 2023.

4.

COATED HONEYCOMB ELECTROMAGNETIC ABSORBERS

The multilayer optimization detailed in Chapter 3 demonstrated that targeted absorption at 5.4 GHz is achievable within a 2.8 mm stack, providing a compact additive solution for satellite EMI mitigation. Building on these results, this chapter explores a complementary paradigm: embedding C-band attenuation directly within structural honeycomb panels. By functionalizing the load-bearing elements already present in small satellite architectures, this approach co-locates electromagnetic shielding within a pre-existing component, aiming to maintain high performance while further reducing the platform's net mass.

Specifically, the study investigates a C-band (4–6 GHz) honeycomb panel functionalized via sequential dip-coating. This process creates a conformal bi-layer that intimately maps the complex 3D topography of the hexagonal cells without altering their macroscopic geometry. The bi-layer architecture is designed to optimize energy dissipation within the hexagonal cells: a CIP-loaded base layer is deposited directly onto the honeycomb wall, while a GNP-loaded topcoat is applied over it. Both layers utilize the AW water-based formulation characterized in Chapter 2. Unlike the AZ matrix — a proprietary formulation classified under Thales Alenia Space S.p.A. and therefore not openly accessible — the AW paint is commercially available, making it the natural choice for a solution intended to be reproducible and industrially scalable. This study therefore targets a commercially optimized architecture as a first demonstrator, with the integration of the AZ matrix representing a natural evolution toward further minimizing stack thickness and mass once the large material batches required for systematic honeycomb fabrication and testing become accessible.

Alongside the physical architecture, a central objective of this chapter is to demonstrate the effectiveness of the single-layer equivalent effective medium model as a reliable tool for simplifying the electromagnetic analysis of geometrically complex, periodic three-dimensional structures. By extracting effective parameters through WR187 waveguide characterization, the functionalized honeycomb is modeled as a homogeneous equivalent layer. The effectiveness of this representation is assessed through a triple-correlation framework encompassing experimental measurements, analytical modeling, and cell-level full-wave simulations in CST Microwave Studio. Successfully demonstrating the accuracy of this homogenized description across the lower C-band would establish a computationally tractable framework directly extensible to large-scale satellite-level simulations, confirming that the effective medium approach — already validated for planar multilayer geometries in Chapter 3 — retains its predictive power when applied to structurally integrated, periodic aerospace components.

4.1 Fabrication and characterization

This section details the experimental methodologies utilized to realize and evaluate the functionalized honeycomb absorber. It first outlines the sequential dip-coating procedures required for the physical construction of the prototype, followed by a description of the specific characterization techniques employed to assess its resulting morphological and electromagnetic properties.

4.1.1 Fabrication

The fabrication phase centred on the development of two functionally distinct coatings: a magnetically loaded paint based on CIP and a lossy dielectric paint incorporating GNP. For the magnetic foundation, CIP was dispersed into the AW polymer matrix at three discrete weight concentrations — 30, 50, and 70 wt% — maintaining the same formulation strategy established during the material characterization campaign of Chapter 2. The principal methodological departure from that earlier work lies in the deposition technique: whereas Chapter 2 employed air spraying for planar sample preparation, the honeycomb integration required a transition to dip-coating, driven by the geometric complexity of the honeycomb architecture. Achieving a conformal, uniform distribution of CIP across the intricate internal surfaces of the hexagonal cells is non-trivial; air spraying produces directional deposition that is inherently ill-suited to reaching the recessed cell walls, whereas full immersion ensures that every surface within the periodic structure is wetted simultaneously. Homogenisation of the suspension was accomplished through high-shear mechanical mixing, which suppresses particle agglomeration and sustains a stable colloidal state throughout the immersion and withdrawal cycle, preventing localised filler settling that would otherwise compromise the spatial uniformity of the permeability distribution.

The dielectric topcoat, loaded with GNP at a fixed concentration of 8.5 wt% as established in prior investigations [12], demanded a more elaborate preparation protocol reflective of the tendency of graphitic nanoplatelets to restack under van der Waals attraction. An initial mechanical mixing step was followed by high-intensity ultrasonication via a sonotrode, whose cavitation-induced shear fields progressively separate and debundle the platelet agglomerates, exposing a greater fraction of the GNP surface area to the polymer matrix. A final high-shear mixing stage consolidated the dispersion before deposition, ensuring that the exfoliated state achieved during ultrasonication was preserved in the applied coating rather than lost to reagglomeration during handling.

For both layers, controlled withdrawal after immersion was followed immediately by rotational curing at 150 rpm. This continuous rotation counteracts the gravitational drainage that would otherwise drive filler migration toward the lower edges of each cell wall during solvent evaporation, a phenomenon that would introduce thickness gradients incompatible with the target electromagnetic response. The rotational curing step is a geometrically necessary condition for maintaining the conformal precision upon which the intended bilayer architecture — and its associated wave-trapping mechanism — ultimately depends.

4.1.2 Morphological characterization

Morphological characterization of the coated honeycombs is conducted through optical microscopy to investigate the macroscopic distribution of the layers and verify the structural integrity of the composite. As shown in Fig. 4.1, the analysis tracks the transition from the bare aramid honeycomb core to the single-layer magnetic coating, and finally to the complete heterostructure loaded with both CIP and GNP. These observations confirm the absence of macroscopic delamination between the sequential layers.

Notably, the optical micrographs reveal a characteristic accumulation of paint within the V-junctions or nodal areas of the honeycomb cells. Despite the rotational curing process intended to homogenize the coating, the complex geometry of the lattice naturally traps a higher volume of the viscous matrix in these corners due to surface tension and capillary effects. This non-uniform distribution remains an inherent feature of the dip-coating method on periodic structures.

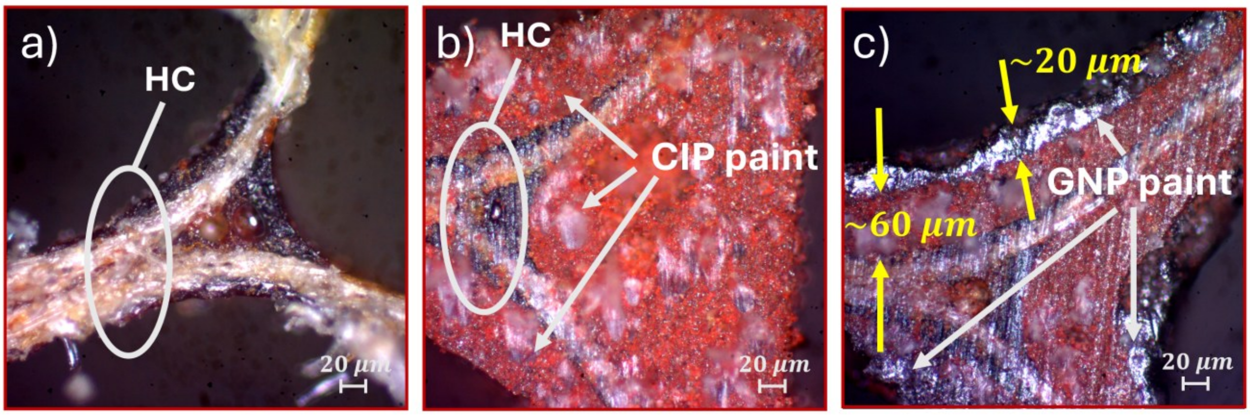

Fig. 4.1 Optical microscopies of the cross section of the uncoated HC (a), coated HC with 70 wt% CIP-loaded paint (b) and with double coating (c).

Complementing these macroscopic observations, SEM is utilized to assess the microstructural features and the quality of the boundary between the functional layers. Fig. 4.2 highlights a distinct morphological transition from the tightly packed spherical CIP clusters, on the left side of the image, to the structural domains of the GNP layer, on the right side. This microscopic inspection confirms intimate contact and robust adhesion between the two loaded polymer matrices, ensuring both structural and electromagnetic continuity across the composite layers.

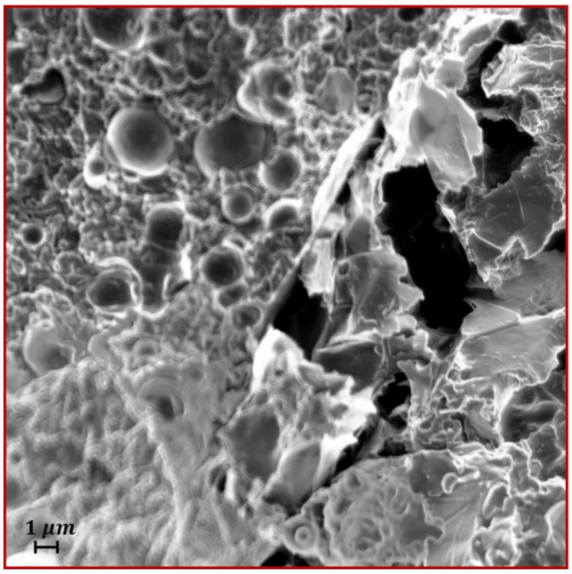

Fig. 4.2 SEM micrograph capturing the interface and robust adhesion between the inner CIP-loaded magnetic foundation and the outer GNP-loaded dielectric coating.

4.1.3 Electromagnetic characterization

The electromagnetic performance of the proposed absorber was evaluated in two sequential phases. First, the intrinsic complex parameters of the constituent loaded paints were isolated and quantified to establish baseline material properties. Following this, the macroscopic effective parameters of the fully integrated 3D honeycomb structures were characterized to assess the overall performance of the assembled composite architecture.

4.1.3.1 Loaded paints

This section details the preliminary planar measurements of the AW paint conducted to define the material properties before their application to the complex honeycomb geometry. Since these cured films are not self-standing, the sample preparation and de-embedding protocol established in Chapter 2 is employed. This involves the deposition of the formulated paints onto thin rigid substrates, which are subsequently machined into annular rings (7.00 mm outer and 3.05 mm inner diameter) to fit the coaxial airline environment, as represented in Fig. 3.

The extraction of the intrinsic complex relative permittivity and permeability of these isolated thin films follows the previously established sequential measurement and de-embedding procedure. By removing the electromagnetic influence of the supporting layers and applying the modified Nicolson-Ross-Weir (NRW) method, an accurate baseline of the material parameters is obtained. Fig. 4.3 represents the coaxial airline and the sample on the rigid substrates. The frequency-dependent electromagnetic parameters extracted from the coaxial measurements, which are essential for the subsequent 3D full-wave simulations, are presented in Fig. 4.4 and 4.5. Specifically, Fig. 4.4a and 4.4b illustrate the ε^* spectra of the unloaded polymer matrix and the lossy dielectric paint loaded with 8.5 wt% GNP. Conversely, the frequency-dependent ε^* and μ^* of the magnetic paint across the three formulated CIP concentrations is the same presented in Section 2.2.3.3, in Fig. 2.18. As observed in the data, a clear proportional trend is established: both the ε^* and μ^* exhibit a consistent increase as a function of the filler loading within the host matrix, confirming the expected macroscopic physical behavior of the composite. These extracted frequency-dependent parameters served as the essential material inputs for the subsequent 3D full-wave simulations. In particular, they were assigned to the geometrically modeled CIP and GNP coating layers on the honeycomb cell walls, ensuring the numerical analysis accurately reflected the real-world electromagnetic response of the composite.

Fig. 4.3 Coaxial airline with thin film loaded on rigid substrates inserted on the central pin of the coaxial airline.

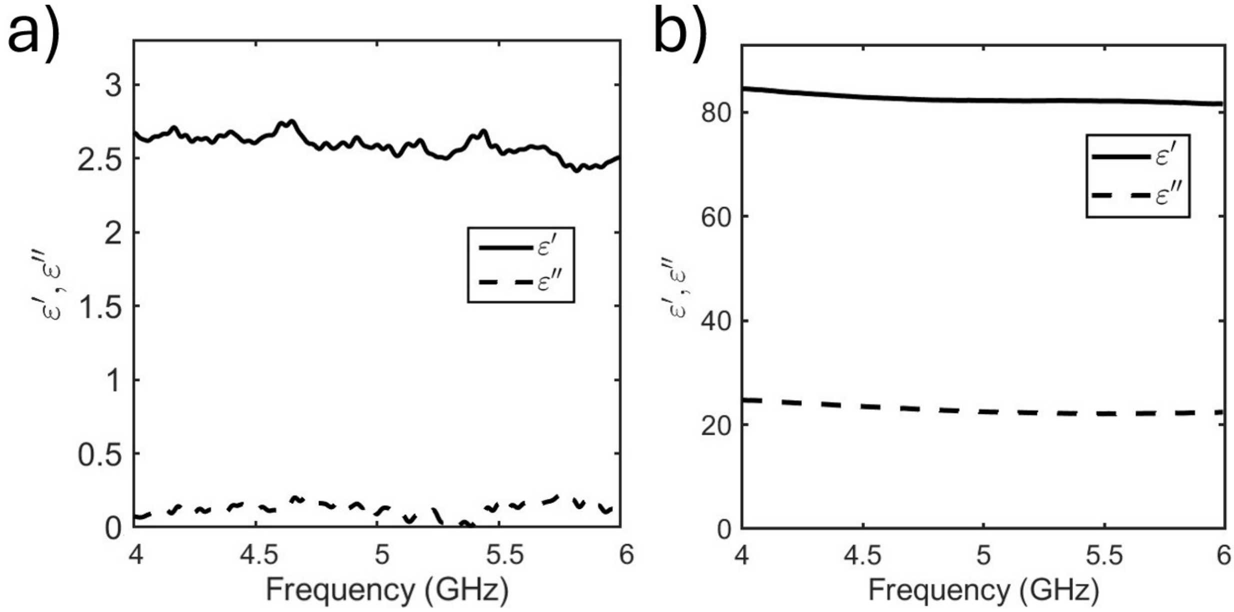

Fig. 4.4 Complex relative permittivity of neat (a) and 8.5 wt% GNP-loaded paint (b).

4.1.3.2 Coated honeycombs

Following the intrinsic characterization of the individual paints, experimental measurements were conducted on the fully fabricated honeycomb specimens to extract their effective complex relative

permittivity ($\varepsilon_{eff}^{*} = \varepsilon_{eff}' - j\varepsilon_{eff}''$) and permeability ($\mu_{eff}^{*} = \mu_{eff}' - j\mu_{eff}''$), which are essential for modeling the complex periodic geometry as a single equivalent homogeneous layer. The coated honeycomb samples—progressing from single-layer CIP or GNP configurations to the final dual-layer GNP/CIP architecture—were characterized across the C-band using a WR187 rectangular waveguide, shown in Fig. 6. To ensure measurement precision and eliminate systematic errors at the reference planes, the waveguide setup was rigorously calibrated using a Short-Short-Load-Thru (SSLT) kit, shown in Fig. 4.5b.

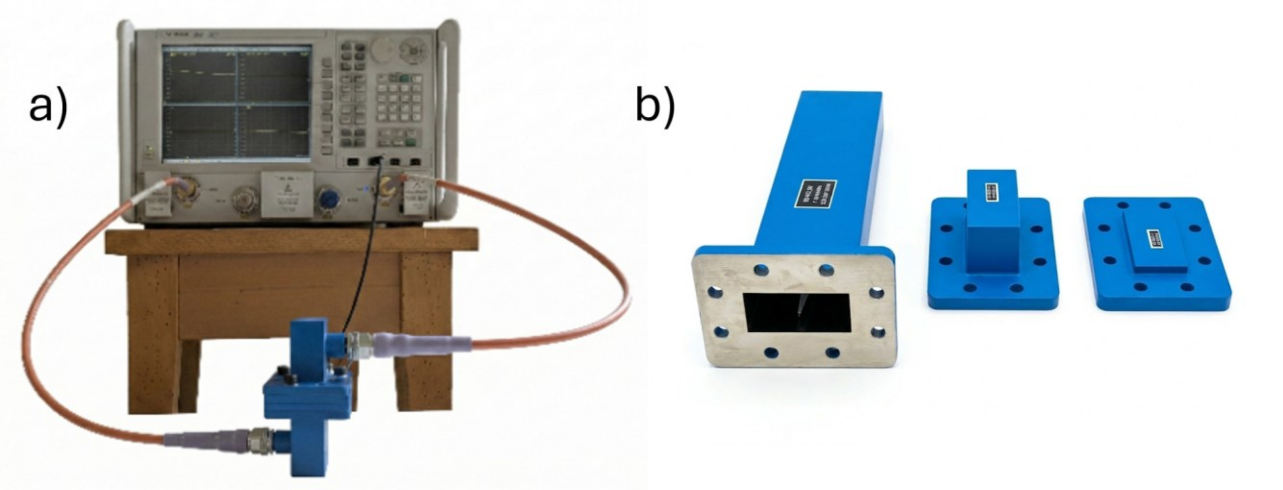

Fig. 4.5 Agilent N5245A PNA-X Vector Network Analyzer with WR187 rectangular waveguide setup (a) and SSLT Calibration Kit (b).

The acquired S-parameters were then processed to accurately capture the macroscopic electromagnetic response of the structures. The effective relative permittivity and permeability are simultaneously extracted by solving the coupled equations that describe electromagnetic wave propagation through the stratified medium, accounting for the sample thickness and measurement frequency. Critically, this extraction process inherently accounts for the air-filled void fraction within the honeycomb cells, automatically yielding volume-averaged effective parameters that represent the composite structure's macroscopic response rather than the properties of the coating material alone.

The validity of this effective medium approach relies on the fundamental assumption that the honeycomb cell dimensions remain significantly smaller than the electromagnetic wavelength (d << λ), ensuring that the incident wave cannot resolve the internal periodic structure and responds to the composite as if it were a homogeneous material. Under these conditions, the extracted effective parameters represent the volume-weighted electromagnetic properties of the entire honeycomb-coating system, incorporating both the dielectric/magnetic contributions of the coatings and the dilution effects of the air-filled cells. This homogenization theory provides the theoretical foundation that justifies treating the complex three-dimensional honeycomb architecture as an equivalent single-layer material for electromagnetic modeling purposes.

As illustrated in Fig. 4.6, while the effective parameters for the single-layer configurations show a diluted macroscopic response due to the high volume of internal air, both the ε^*_{eff} *and* μ^*_{eff} of the CIP-coated samples exhibit a clear, proportional increase corresponding to the magnetic filler concentration, with the expected exception of the non-magnetic honeycomb coated solely with the 8.5 wt% GNP. The effective relative permittivity data (Fig 4.6a and b) demonstrates that ε'_{eff} increases systematically with CIP loading, reflecting the enhanced polarization contribution from the magnetic particles. The imaginary component ε''_{eff} follows a similar trend, indicating increased dielectric losses that contribute to electromagnetic absorption. The frequency-dependent behavior visible in these plots reveals the dispersive nature of the composite, with both real and imaginary components showing characteristic variations across the C-band that are essential for accurate broadband modeling.

The effective relative permeability results (Fig. 4.6c and d) provide direct confirmation of the magnetic enhancement achieved through CIP incorporation. The real component μ'_{eff} shows a clear progression from unity to elevated values that scale with the magnetic filler concentration, while μ''_{eff} demonstrates the magnetic loss mechanisms that contribute to the overall absorption performance. The frequency dependence of these parameters reflects the underlying magnetic relaxation processes within the CIP particles, with the peak positions and magnitudes providing insight into the dominant loss mechanisms at different frequencies. These systematic trends validate the effectiveness of the CIP incorporation strategy and confirm that the magnetic enhancement can be precisely controlled through filler concentration optimization.

Fig. 4.7 details the EM characterization of the fully realized bi-layered system, which represents the culmination of the multi-functional coating strategy. In this configuration, the μ^*_{eff}remains highly coherent with the results from single-layered CIP coatings, as it is dictated entirely by the foundation layer. However, the ε^*_{eff} exhibits a substantial increase, confirming that the GNP-loaded topcoat successfully enhances dielectric polarization along the cell walls and compounds the structure's overall loss mechanism. The relative permittivity enhancement in the dual-layer system (Fig. 4.7 a and b) demonstrates the additive effects of the GNP topcoat, where the conductive graphene nanoplatelets create additional polarization mechanisms. The magnitude of this enhancement varies across frequency, indicating that the GNP contribution involves multiple loss mechanisms including conductive losses, interfacial polarization, and possibly quantum capacitance effects at the GNP-polymer interfaces.

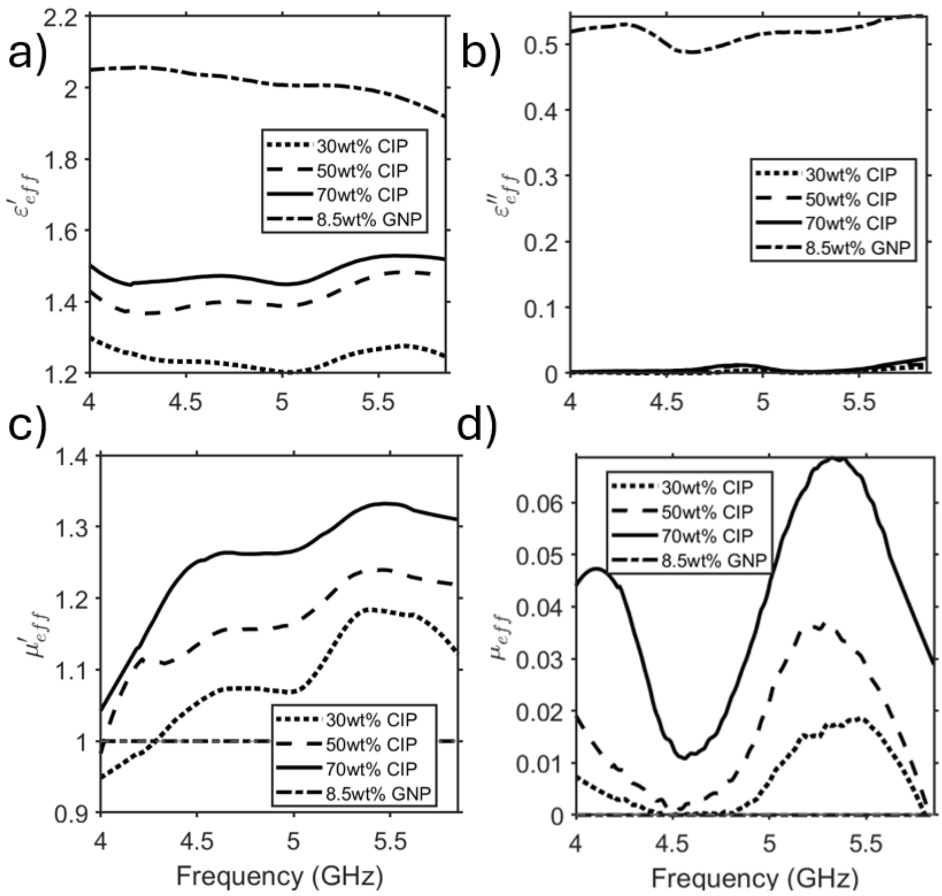

Fig. 4.6 Effective complex relative permittivity (a, b) and permeability (c, d) of single-layer coated honeycombs.

The relative permeability response (Fig 4.7 c and d) confirms that the magnetic properties remain dominated by the CIP foundation layer, validating the design strategy of spatially separating the magnetic and dielectric enhancement functions. The consistency between single-layer and dual-layer μ^*_{eff} values demonstrates that the GNP topcoat does not significantly interfere with the magnetic behavior of the underlying CIP coating, ensuring that the dual-layer approach achieves the intended electromagnetic property enhancement without undesired coupling effects. This functional independence between the magnetic and dielectric enhancement layers represents a critical design achievement, as it allows for independent optimization of each electromagnetic property while maintaining the overall system performance.

The systematic trends observed in both single-layer and dual-layer configurations validate the effective medium extraction methodology and confirm that the honeycomb-coating composites can be accurately represented as homogeneous materials for electromagnetic modeling purposes. This validation is crucial for the subsequent integration of these parameters into full-system simulations, where the computational efficiency gained by treating the complex honeycomb geometry as an equivalent homogeneous layer enables practical analysis of complete satellite cavity configurations without sacrificing accuracy. The successful extraction and validation of these effective parameters establishes the foundation for transitioning from component-level characterization to system-level electromagnetic performance prediction, bridging the gap between material engineering and practical aerospace applications.

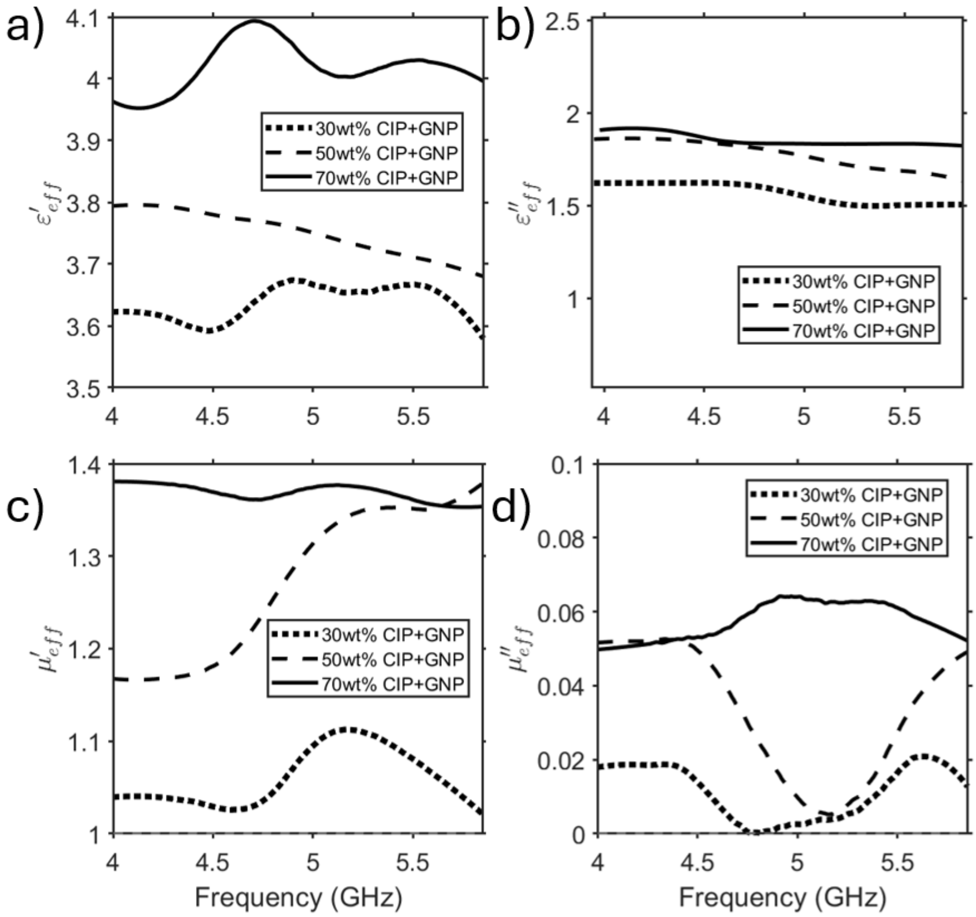

Fig. 4.7 Effective complex relative permittivity (a, b) and permeability (c, d) of double-layer coated honeycombs.

4.2 EM 3D full-wave simulations

The numerical analysis and optimization of the radar-absorbing structure were performed using the CST Microwave Studio full-wave electromagnetic solver. To accurately replicate the physical samples, the honeycomb core and its conformal bi-layered coatings were explicitly modeled to match the exact fabricated geometry and measured coating thicknesses, as in Fig. 4.8. To ensure the high fidelity of this numerical model, the frequency-dependent intrinsic parameters (ε^* and μ^*) extracted from the de-embedding algorithms discussed in Section 4.3.1 were assigned to their respective layers, capturing the real dispersive behavior of the various CIP and GNP formulations. To verify the accuracy of the numerical framework, the structures were first simulated within a virtual WR187 rectangular waveguide environment. Two distinct numerical approaches were evaluated: the high-fidelity 3D geometric model featuring the explicitly coated cell walls, and an approximated equivalent single-layer model utilizing the experimentally extracted effective complex parameters. As illustrated in Fig. 4.9, a triple-correlation analysis was performed by comparing the experimentally measured S-parameters against the scattering responses of both numerical models. This validation phase was foundational, establishing the necessary accuracy of the computational setup before transitioning to the evaluation of the structure as a practical radar absorber (RAM). By confirming the consistency between the waveguide measurements and the numerical models, the simulation environment could be reliably adapted to a free-space configuration. This enabled the subsequent modeling of a periodic unit cell and the single-layer equivalent backed by a Perfect Electric Conductor (PEC), facilitating the parametric optimization of the honeycomb core thickness to maximize internal attenuation and minimize reflection loss across the lower C-band.

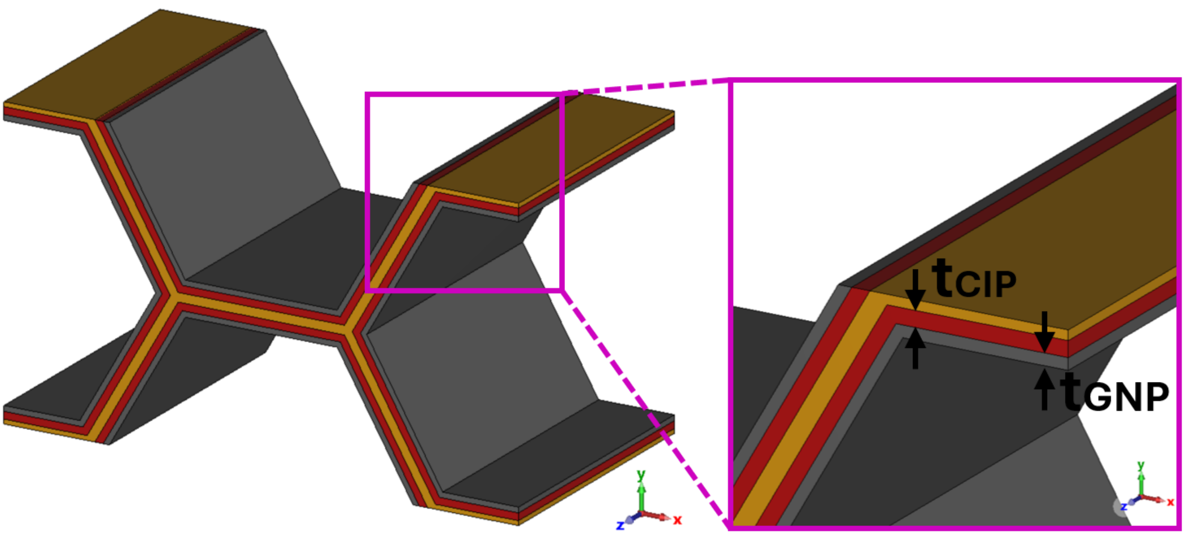

Fig. 4.8 Elementary cell of CST simulations: Aramid in orange, CIP-loaded paint in red, and GNP-loaded paint in grey.

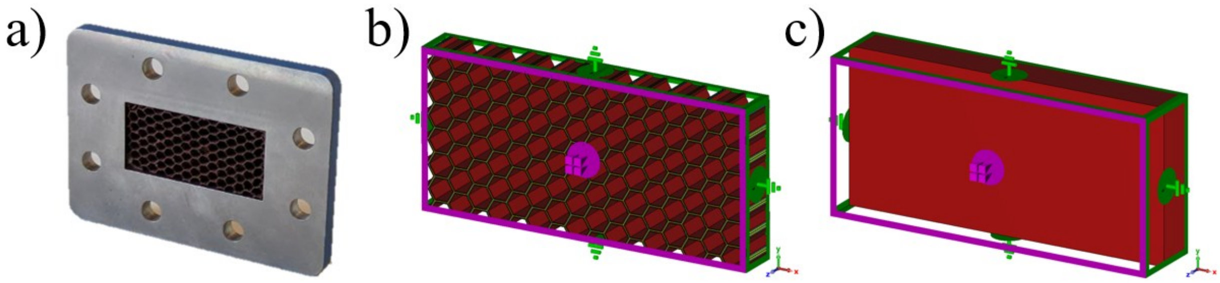

Fig. 4.9 Triple-correlation setup: (a) HC sample in WR187 flange; (b) 3D geometric simulation; (c) effective single-layer equivalent.

As shown in Fig. 4.10, the results demonstrate a high degree of agreement in terms of magnitude. The bi-layered honeycomb model, in particular, exhibits a strong correlation with the experimental S_{11} and S_{21}curves. Conversely, a noticeable divergence is observed in the phase responses, characterized by a non-linear upturn in the simulated $\angle S_{11}$ phase and a constant offset in $\angle S_{21}$. This discrepancy is corroborated by the morphological characterization: while the numerical simulations assume an idealized geometry with a perfectly homogeneous coating, the fabricated samples exhibit localized filler accumulations at the honeycomb V-junctions, as observed through optical microscopy. These physical clusters create a non-ideal scattering environment, altering the local refractive index encountered by the incident wave. Consequently, this leads to a more linear phase dispersion in the experimental measurements compared to the idealized, coherent reflections generated by the numerical model.

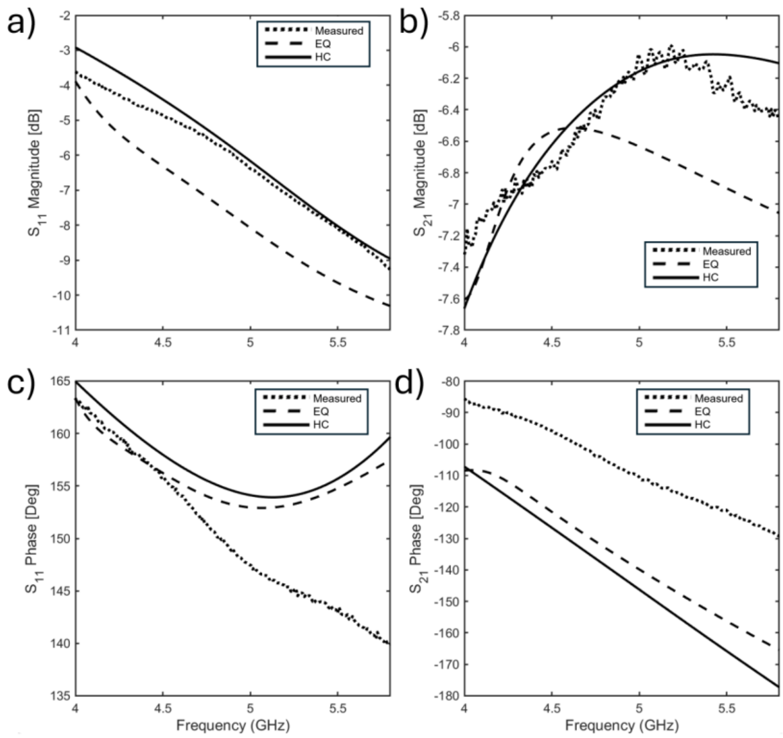

Fig. 4.50 S-parameter magnitude (a, b) and phase (c, d) comparison between experimental measurements, 3D geometric simulation (HC) and approximate effective single-layer model (EQ).

To further validate the reliability of the design approach, the linear scalability of the bi-layered system was investigated by analyzing samples subjected to sequential mechanical thickness reductions. This experimental phase aimed to demonstrate that the intrinsic material properties remain stable and predictable even as the macroscopic physical dimensions are altered, which is fundamental for practical design optimization and manufacturing tolerance analysis. The results indicate that as the thickness is reduced, the structure continues to perform in close alignment with numerical predictions, confirming that the electromagnetic response can be precisely tuned to target specific frequencies through simple mechanical adjustments. This consistency is quantitatively supported by an analysis of the phase behavior across the different thickness stages, which reveals fundamental insights into the material's electromagnetic integrity under mechanical processing.

Specifically, as shown in Fig. 4.11a, the unwrapped phase of the transmission coefficient at 5 GHz—selected as an explicative reference for the system's behavior—exhibits a high degree of correlation with sample thickness. The linear relationship demonstrates that the phase accumulation follows the theoretical expectation $\varphi = \beta t$, where β is the phase constant and t is the thickness, confirming that the effective material properties remain constant despite the mechanical reduction process. This relationship is confirmed by a linear fit with an R^2 value greater than 0.99, indicating that less than 1% of the phase variation can be attributed to factors other than the geometric thickness change. This linearity confirms that the phase delay is a direct, predictable function of the physical dimension, validating both the coating adhesion and the preservation of electromagnetic properties throughout the mechanical processing.

Furthermore, when analyzing the normalized phase—defined as the phase divided by the sample thickness (Fig. 4.11b)—the resulting curves for the various thickness levels nearly overlap across the entire 4-6 GHz band. This overlap is particularly significant as it demonstrates that the specific phase per unit thickness ($\partial\varphi/\partial t$) remains constant regardless of the absolute sample dimensions, confirming that the material behaves as a true bulk electromagnetic medium rather than exhibiting thickness-dependent boundary effects. The frequency dependence of this normalized phase reveals the intrinsic dispersive characteristics of the bi-layered composite, with the slight variations observable across the frequency range directly correlating to the frequency-dependent complex relative permittivity and permeability of the CIP and GNP components. This behavior validates the robustness of the coating process and the overall coherence of the effective electromagnetic medium, establishing confidence in the scalability of the design for different application requirements.

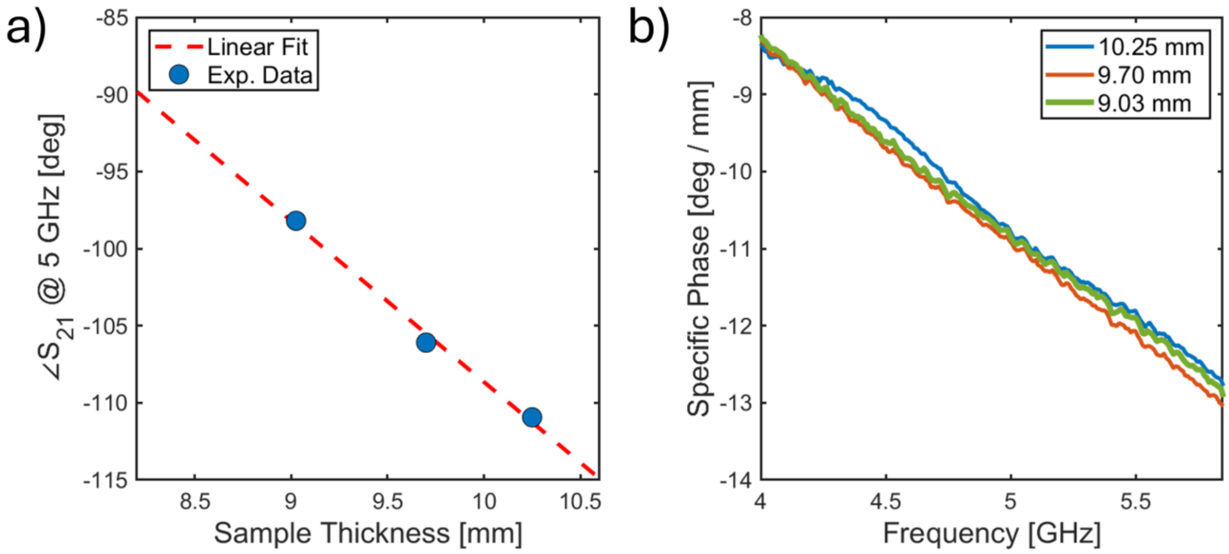

Fig. 4.11 Phase-based scalability: (a) linear correlation between phase and thickness at 5 GHz; (b) frequency-dependent specific phase per unit thickness.

Finally, to evaluate the radar-absorbing performance of the structure, both the full 3D geometric model (HC) and the approximated equivalent single-layer material model (EQ) were analyzed in a free-space simulation environment backed by PEC. The transition from waveguide to free-space analysis represents a critical validation step, as it tests the absorber performance under realistic conditions where the incident wave encounters the structure at normal incidence without the constraining boundary conditions of a metallic waveguide. As shown in Fig. 4.13, the simulated reflection loss (RL) spectra of the two models exhibit a slight frequency shift and amplitude variation, with the differences providing valuable insights into the accuracy and limitations of the homogenization approach.

This discrepancy is physically anticipated and can be attributed to several fundamental factors: the EQ homogenization approach treats the highly porous honeycomb core as a uniform solid single layer, inherently neglecting localized 3D scattering effects that occur at individual cell boundaries, cell-edge diffraction phenomena that arise from the sharp geometric transitions between air-filled voids and coated walls, and specific impedance mismatches at the complex air-material interface that vary spatially throughout the honeycomb structure. The 3D geometric model captures these effects through explicit meshing of the honeycomb topology, resulting in a more accurate representation of the true electromagnetic environment encountered by the incident wave. The frequency shift observed between the models indicates that the effective electrical thickness differs between the homogenized and actual structures, with the real honeycomb exhibiting a slightly different resonant condition due to the complex wave interactions within the periodic cell structure.

Despite these theoretical deviations, the equivalent model reliably captures the overarching absorption trend, demonstrating that the homogenization approach provides sufficient accuracy for design optimization while offering significant computational efficiency advantages. The magnitude of the reflection loss values shows remarkable consistency between the two approaches, with differences typically remaining within 2-3 dB across the frequency range of interest. This level of agreement validates the use of effective medium theory for rapid design iterations while highlighting the need for full 3D validation in the final optimization stages. Crucially, both numerical approaches demonstrate that scaling the structural thickness between 5 and 9 mm consistently yields an RL greater than 10 dB across the targeted lower C-band, with peak absorption values exceeding 20 dB at the optimized thickness values. This performance level confirms highly efficient electromagnetic mitigation that meets or exceeds typical requirements for EMI absorption applications in aerospace systems.

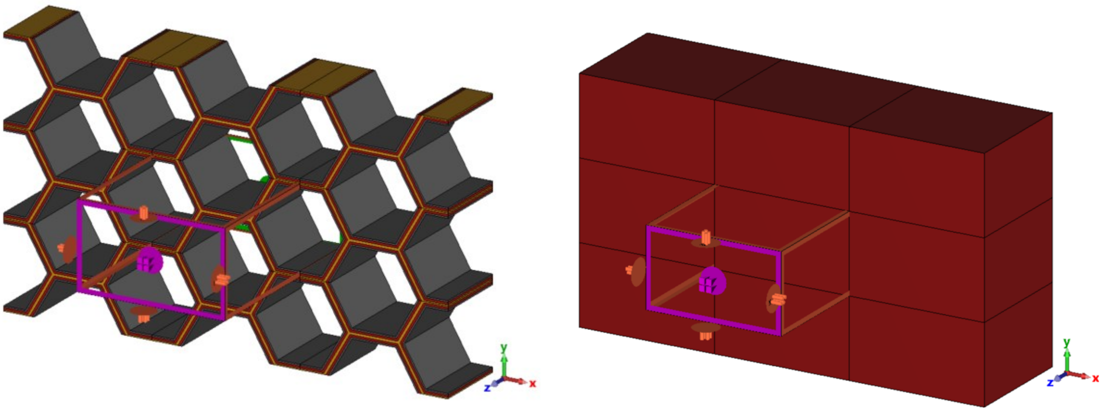

Fig. 4.62 Comparison of the simulated RL between the 3D geometric model (HC) and the approximated equivalent single-layer model.

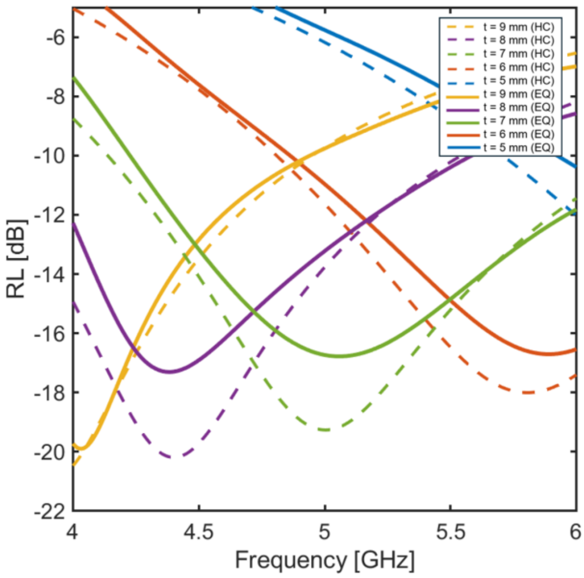

Fig. 4.13 RL spectra of the optimized coated honeycomb absorber configuration.

4.3 Conclusions

This study presented a comprehensive experimental and numerical approach for designing lightweight, honeycomb-based radar-absorbing structures for the lower C-band (4–6 GHz) EMI mitigation. Using a sequential dip-coating technique, a conformal heterostructure was achieved by combining a magnetic CIP foundation with a dielectric GNP topcoat. Characterization confirmed robust interlaminar adhesion and demonstrated that this bi-layer architecture enhances dielectric polarization without compromising the magnetic response. To predict macroscopic behavior, a rigorous numerical framework was established using a triple-correlation analysis to benchmark experimental S-parameters against high-fidelity 3D simulations and a approximated homogenized single-layer model.

Despite minor phase discrepancies from localized filler accumulation at V-junctions, the equivalent model proved highly reliable. Notably, this homogenized equivalent will be instrumental for simulating expansive aerospace and satellite platforms—such as satellite bus components or aircraft airframes—where explicit geometric modeling would impose prohibitive memory requirements. By utilizing this validated model, the large-scale environments investigated in [8] can be analyzed with high fidelity and significantly reduced computational overhead. Finally, free-space simulations confirmed that core thicknesses of 5–9 mm consistently yield a reflection loss exceeding 10 dB, providing a scalable strategy for weight-sensitive and volume-constrained high-density electronic environments.

4.4 References

[1] S. Zecchi et al., "A comprehensive review of electromagnetic interference shielding composite materials," *Micromachines*, vol. 15, no. 2, p. 187, 2024.

[2] C. Wang et al., "The trade-off between impedance matching and loss capability in layer-structured FeSiCr for ultra-broadband microwave absorption with thin thickness," *J. Alloys Compd.*, vol. 1035, p. 181543, 2025.

[3] A. Rinaldi et al., "Graphene-coated honeycomb for broadband lightweight absorbers," *IEEE Trans. Electromagn. Compat.*, vol. 60, no. 5, pp. 1454–1462, 2018.

[4] H. Luo et al., "Preparation and microwave absorption properties of honeycomb core structures coated with composite absorber," *AIP Adv.*, vol. 8, no. 5, p. 056635, 2018.

[5] J. S. Noh et al., "All-nickel-coated glass fabric honeycomb sandwich composite for robust and lightweight radar absorption," *Compos. Part A: Appl. Sci. Manuf.*, 2024.

[6] Y. Xian et al., "A novel frequency-selective surface-enhanced composite honeycomb absorber with excellent microwave absorption," *Polymers*, vol. 16, no. 23, p. 3312, 2024.

[7] M. S. Hareesh et al., "Electromagnetic interference shielding: a comprehensive review of materials, mechanisms, and applications," *Nanoscale Adv.*, vol. 7, no. 15, pp. 4510–4534, 2025.

[8] A. N. Casling et al., "Performance assessment of magnetic polymeric composites for EMI reduction in small satellites," in *Proc. 2025 ESA Workshop on Aerospace EMC*, IEEE, 2025.

[9] S. Hassan et al., "Carbon based composite materials for microwave absorption in low frequency S and C band: A review," *ChemNanoMat*, vol. 10, no. 12, Oct. 2024.

[10] C. Shen et al., "Synergistic integration of CIP and graphene within honeycomb architectures toward high-efficiency electromagnetic wave absorption," *Coatings*, vol. 15, no. 11, p. 1262, 2025.

[11] Y. Li et al., "High-efficiency design of multifunctional radar absorbing honeycomb structures for enhanced ultrathin, broadband, and load-bearing performance," *Adv. Funct. Mater.*, 2025.

[12] F. Cozzolino et al., "New sensing and radar absorbing laminate combining structural damage detection and electromagnetic wave absorption properties," *Sensors*, vol. 22, no. 21, p. 8470, Nov. 2022.

[13] A. M. Nicolson and G. F. Ross, "Measurement of the intrinsic properties of materials by time-domain techniques," *IEEE Trans. Instrum. Meas.*, vol. 19, no. 4, pp. 377–382, Nov. 1970.

[14] W. B. Weir, "Automatic measurement of complex dielectric constant and permeability at microwave frequencies," *Proc. IEEE*, vol. 62, no. 1, pp. 33–36, Jan. 1974.

5.

CONCLUSIONS AND FUTURE DEVELOPMENTS

This doctoral research has culminated in a technical framework for EMI mitigation in next-generation satellite architectures by demonstrating that the transition from monolithic metallic shielding to integrated, lossy thin-film and structural absorbers provides a scalable solution to the challenges of high-density electronic packaging. The findings confirm that the host polymer matrix is a primary design variable; the use of an organic solvent-based aerospace-grade matrix (AZ) facilitated superior interfacial wetting and a more homogeneous dispersion of CIP fillers compared to the water-based AW system. At 2 GHz, taken as a representative example frequency for TT&C communications, the 70 wt% AZ composite achieved a real permeability of 3.3, whereas the AW equivalent reached only 1.9, a distinction that proved critical for compressing the incident wavelength within the material and allowing for the design of absorbers that are physically thinner than the traditional quarter-wavelength limit. While high-energy ball milling successfully transformed spherical CIP into high-aspect-ratio flakes, morphological characterization via SEM-EDS confirmed a severe susceptibility to oxidation, leading to the conclusion that despite a theoretical boost in permeability, flaky morphology is unsuitable for an industrial aerospace workflow due to chemical instability and the high risk of property drift during thermal cycling.

The application of a tunability-by-design approach through multilayered architectures successfully resolved the conflict between achieving superior electromagnetic performance and maintaining industrial viability by combining stable spherical CIP with complementary dielectric enhancement layers, with numerical optimization showing that the AZ-GCS configuration could achieve a reflection loss of -20.11 dB at 2 GHz if 6.21 mm thick and -15.00 dB at 5.4 GHz with only six repetitions, equal to 2.8 mm. Furthermore, the functionalization of honeycomb cores with a bi-layered CIP/GNP coating proved that geometric multiple internal reflections mechanisms can compensate for lower material thickness by exploiting the honeycomb's cellular architecture to extend electromagnetic path length beyond simple geometric dimensions. The inner magnetic CIP foundation layer dictates the inductive response by providing enhanced permeability that compresses the incident wavelength, while simultaneously introducing magnetic losses through relaxation mechanisms. The outer GNP topcoat optimizes dielectric losses via conductive pathways and interfacial polarization, creating enhanced permittivity and substantial dielectric losses that provide impedance matching at the air-absorber interface. This functionally graded approach ensures efficient attenuation of both electric and magnetic field components, yielding a reflection loss exceeding 10 dB across the 4–6 GHz band with peak absorption reaching -15 to -20 dB while maintaining total thickness below 8 mm, representing 90-99% absorption efficiency.

The experimental validation of these structures established a rigorous triple-correlation framework—benchmarking experimental S-parameters against high-fidelity 3D simulations and homogenized effective medium models—which provided comprehensive validation of the single-layer effective medium approach. Both the fabricated honeycomb samples and their corresponding equivalent effective models demonstrated that the complex periodic structures can be accurately represented by simplified effective parameters, with the experimental S-parameter measurements showing good agreement with the homogenized model predictions across the entire frequency range. This validation extends beyond mere numerical convergence: the physical structures themselves confirmed that the volume-averaged effective relative permittivity and permeability capture the essential electromagnetic behavior of the multi-scale honeycomb-coating composite, enabling high-fidelity prediction of E-field reduction without the prohibitive computational cost of modeling micro-scale coatings. The success of this effective medium representation for both single-layer and dual-layer configurations establishes a reliable foundation for large-scale system simulations, where complex geometric details can be abstracted into equivalent material properties without sacrificing accuracy in electromagnetic compatibility predictions.

Ultimately, this thesis provides the aerospace industry with a space-qualified material baseline and a reliable methodology to ensure electromagnetic compatibility in the increasingly congested and miniaturized architectures of future space missions.

Looking toward future perspectives, the research transitions from the fundamental material validation and 1D/3D simulations established in this work toward the experimental assessment of these systems within a real-world satellite scenario. A critical next step involves the integration of these conformal coatings and multilayered films into a physical engineering model of a satellite structure to be tested within a large-scale anechoic chamber. Such a measurement campaign will allow for the empirical verification of the predicted radar absorbing effectiveness and the suppression of cavity resonances under real radiated emission conditions, accounting for complex diffraction effects and aperture leakages that are difficult to model in isolation. Furthermore, the industrial qualification of the AZ-based structures will require systematic Thermal Vacuum cycling to monitor mass loss and outgassing, as well as radiation aging tests to ensure the long-term electromagnetic stability of CIP in the harsh environment of Low Earth Orbit.

Complementing these efforts, the temperature-dependent characterization of the electrical properties of the GNP composite represents a necessary progression from the room temperature baseline established in this work. Measuring DC conductivity and percolation behavior across the operational thermal range of satellite structures — typically spanning from −150°C to +150°C — will be essential to assess the stability of the conductive network under thermally induced mechanical stress and to validate the material's suitability for sustained use in orbit.

Appendix

This industrial PhD project was co-funded by Thales Alenia Space Italia S.p.A. and Regione Lazio. The research was primarily conducted within the laboratories of the Department of Electrical and Energy Engineering (DIEE) and the Research Center for Nanotechnology Applied to Engineering (CNIS) at Sapienza University of Rome, with significant activities also hosted at Thales Alenia Space Italia S.p.A. premises.

Activities conducted at the University focused on the synthesis and fabrication of advanced materials and test samples, leveraging specialized know-how in the development of nanocomposites loaded with Graphene Nanoplatelets (GNP). Fabrication processes were carried out within the Nanotechnology Laboratory of the DIEE. A core component of the laboratory work involved the comprehensive characterization of the fabricated materials, conducted across the Electromagnetic Compatibility (EMC) Laboratory and the CNIS facilities. These analyses focused on morphological, electrical, and electromagnetic properties to evaluate dispersion, conductivity, and radar-absorbing performance. Furthermore, the design and implementation of specialized optimization codes and algorithms, along with preliminary 3D full-wave electromagnetic simulations, were performed at the University level to validate material behavior at the sample stage.

Thales Alenia Space Italia S.p.A. acted as the industrial partner, providing the aerospace-grade matrix (AZ) essential for the study. Utilizing their high-performance computing infrastructure and internal EMC Laboratory, in-company 3D full-wave simulations specifically tailored to the satellite scenario were performed.